Parameters affecting inductive displacement sensors

Wilkinson, Michael Richard

PARAMETERS AFFECTING INDUCTIVE DISPLACEMENT SENSORS

Michael Richard Wilkinson

2003

Thesis for the Degree of Master of Science

School of Engineering

University of Durham

Abstract

An investigation of the limitations of inductive displacement sensors (IDSs) was conducted with the use of electromagnetic finite element analysis (FEA). A comparison of displacement sensing technologies highlighted the advantages of IDSs in harsh industrial environments, but an understanding of the operation of IDSs showed that they are limited by the influence of target material, width and offset. It was proposed that studying the electromagnetic field around IDSs could reveal more information than was available from the simple impedance measurements employed by a commercially available IDS.

A test coil sensor and signal processing system was designed and the result was a reliable system for measuring the magnetic field around the IDS. Experiments showed that the 1 MHz field had an amplitude of 5×10^{-6} T at the base of the IDS and two- and three-dimensional FEA models were constructed that gave closely matching central field values.

The unreliability of the IDS for different target materials was demonstrated experimentally. FEA simulations showed that changing target permeability and varying target displacement both altered the whole field amplitude uniformly. This showed that it was not possible to counteract the target dependence by monitoring the field with the test coil system in this way. Further FEA simulations revealed field patterns that changed with target offset. An experiment with the test coil system confirmed that it was possible to use the change in lobe amplitude to measure the offset of the target; for example when target displacement d_t = 25 mm and offset o_s = 1.2 times the IDS coil diameter, the distance error was 3.6 %, which corresponded to a normalised test coil output of 0.54. A similar effect was found from target width FEA simulations. Hence it was possible to correct the output signal from the IDS coil to counteract the effect of an offset small target.

Contents

List of Figures

List of Tables

Declarations

The author confirms that this thesis conforms to the word length prescribed for the degree to which it is submitted.

No part of the material offered in this thesis has been previously submitted by the author for a degree in this or any other University.

Statement of Copyright

Acknowledgements

The support and continuously optimistic encouragement from my supervisor Sherri Johnstone has been very much appreciated and has been pivotal to the success of this work. Many thanks are also extended to Dave Wood for his assistance throughout the project.

Chapter 1

Introduction

The sensor industry is a diverse one, yet it is vital to almost all modern manufacturing processes. Continual sensor research and development is required to meet the needs of industry by providing innovative solutions to increase reliability and decrease costs. The field encompasses research into a range of technologies including optical, ultrasonic and biological for functions such as liquid and gas sensing, displacement measurement, tomography and water quality monitoring. Industry sectors where applications are found are just as diverse and include the automotive industry, structural monitoring for civil and aerospace structures, the chemical industries and the food industry [1].

In many industrial locations — for example in steel works and on production lines — the distance to metallic materials often needs to be measured and monitored. This task can be difficult when the application environment is dusty, steamy or similarly harsh. Inductive proximity sensors are appropriate for this type of situation because they rely on electromagnetic fields that can pass through the intervening medium unaffected. This type of sensor is now common place in harsh industrial environments, so the exploration of their limitations and subsequent improvement is an important physical problem.

This thesis summarises research performed in this important area and in this first chapter the topic is introduced. There are a number of different technologies suitable for non-contact displacement measurements and here capacitive, optical, ultrasonic and inductive sensors are discussed (§ 1.1). Their applications and relative merits are observed with particular reference to the harsh industrial environment described above. This gives a justification to the particular importance of inductive proximity sensors, which are introduced through a discussion of their operating principles (§ 1.2) and applications (§ 1.3). The basis of this work has been the investigation of the limitations of these sensors through research into the influence of target material, offset and width, which are introduced in section § 1.4. The wider context of this work and its relation to previous research and publications is discussed (§ 1.5) before the chapter concludes with a discussion of the organisation of the remainder of this thesis (§ 1.6).

1.1 Non-Contact Spatial Sensors

There are number of spatial measuring devices that are useful in an industrial context and they may be classified as proximity, position, displacement, dimension and vibration sensors. Often a non-contact spatial sensor can operate in a number of these modes depending on how it is installed. Proximity sensors return an on or off output signal denoting presence (or part presence) or absence of the target. Position sensors record the location of an object with respect to a defined reference coordinate. Displacement sensors give the movement from one position to another in a defined direction. Part specific geometrical measurements can be determined with dimension sensors. Finally, the amplitude and frequency of targets with oscillatory motion are commonly measured with a vibration sensor. The advantage of non-contact sensors over contact-based sensors is that there is no risk of damage to fragile parts and the sensor can be positioned in a convenient location to avoid interference with the process being measured. Industrial processes often require the use of these non-contact spatial sensors to monitor the target objects in a number of applications from robotic positioning systems to quality control. Such instruments operate using capacitive, optical, ultrasonic or inductive technologies [2] [3]. Each type has its own set of characteristics and the particular sensor used will depend on considerations such as: the motion and degrees of freedom to be measured e.g. rotational or linear motion in single or multiple dimensions; the operating environment e.g. temperature, humidity, dust, vibrations or mechanical shocks; the required measurement range; and the measurement performance e.g. sensitivity, linearity and accuracy requirements.

1.1.1 Capacitive Sensors

The capacitance of a pair of electrodes is given by the basic formula $C = \varepsilon G$ where ε is the permittivity of the dielectric and G is a geometrical factor. For a parallel flat plate capacitor $G = A/d$ where A is the area of the plates and d is the displacement between them. Capacitance-based non-contact spatial measuring systems consist of a sensing plate positioned above a conducting target and a potential difference developed between the two enables measurement of the capacitance. Such a system can be constructed in a similar manner to a variable capacitor, whereby the overlap between the plates, and therefore A, changes depending on the angular position of the target. This gives an angular position sensor. Alternatively, and more commonly, if the device is assembled such that d changes with the displacement to be measured, then the result is a simple, but linear, non-contact displacement sensor. Devices can be constructed to cover a measurement range of about 2.5 – 250 mm [3].

Capacitive transducers are also sensitive to changes in the material between the sensor plate and the target; therefore maintaining a constant dielectric permittivity is important. The

dielectric constant of air increases with humidity and is also influenced by other materials such as dust, dirt, oil etc. in the sensing gap. This affects the capacitance and thus the resulting distance measurement. Thermal expansion and contraction of sensor components is a further source of error and this is a substantial problem when measuring or controlling to high precisions.

1.1.2 Optical Sensors

Light-emitting diodes (LEDs) and photodiodes (PDs) have fast responses to current and light intensity respectively, which makes them suitable for use in an intensity-based optical displacement sensor. Figure 1.1(a) shows how an LED and a PD can be positioned face on to each other to measure the distance between them. A second PD can be added to compensate for ambient illumination levels and LED fluctuations. Alternatively an angular displacement sensor may be composed from two fixed position PDs and a moveable LED (figure 1.1(b)). Measurement errors are reduced by combining and averaging the signals from the two PDs. To further reduce the influence of ambient illumination, the incident light may be modulated and phase-locking signal processing used to decode the signals from the detector.

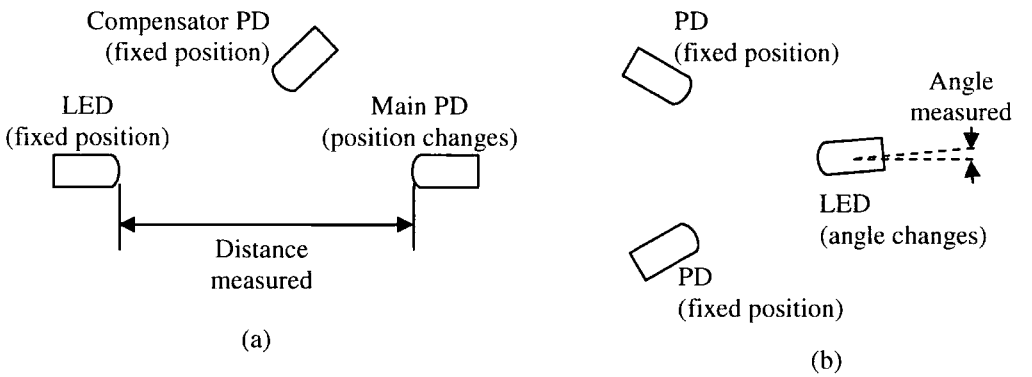

Figure 1.1. Optical displacement sensors with LEDs and PDs. (a) Linear displacement with a second compensating PD. (b) Angular displacement with two main PDs.

Other mechanisms, such as that developed by Wang [4], use light reflected from the target to obtain a displacement measurement. As the reliability of laser diodes has increased, laser-based systems are now available that also use a reflection mechanism. The radiation from laser diodes can be of a much higher intensity than ambient light and so background effects are reduced. However, all optical systems are most obviously limited by the need for a clean measurement gap; intervening dust, oil, metal filings, etc. will reduce the reliability of the measurement.

1.1.3 Ultrasonic Sensors

The term ultrasonic refers to sounds with frequencies greater than those audible to humans, which usually incorporates frequencies greater than 20 kHz. Although medical scanners use frequencies in the range 1 – 20 MHz, ultrasonic spatial sensors typically utilise the range 20 – 200 kHz. Such devices emit a short burst of ultrasonic sound towards a target, which is then reflected back to the sensor. The time between transmission and reception of the burst gives a value for the distance between the sensor and the target. This technology is well established and a wide range of sensors are available which operate at different frequencies and have different radiation patterns. The resolution of the measurements depends on the wavelength of the sound emitted by the sensor, but in general, commercial products are available with resolutions in the range 0.2 – 0.7 % of the full scale.

Assuming transmission occurs under adiabatic conditions, the speed of sound, c, is a function of temperature, T, and varies as

$$c = \sqrt{\frac{\gamma R T}{m}} \tag{1.1}$$

where γ is the ratio of heat capacities, R is the universal gas constant (= 8.314 J.mol^{-1}.K^{-1}) and m is the molar mass of the transmission medium. If it is assumed that air is a diatomic ideal gas ($\gamma = 7/5$) with a molar mass of 29.0×10^{-3} Kg.mol^{-1}, then at $T = 273.15$ K (0 °C), $c = 331.1$ m.s^{-1}. For the higher temperature of $T = 313.15$ K (40 °C), the speed is increased to $c = 354.5$ m.s^{-1}. This demonstrates the requirement for effective temperature compensation.

The nature of the medium in which the ultrasonic system is operating must also be taken into consideration. In a non-dispersive medium — such as air — the frequency has no influence on the speed of sound and the energy and sound travel at the same speed. In a dispersive medium — such as water — sound speed is a function of frequency and each frequency component propagates with its own phase velocity, but the energy travels at the group velocity.

The maximum range of these sensors depends on the attenuation of the sounds waves. In air the attenuation of the ultrasonic pulse increases with the frequency and for each frequency the attenuation is a function of humidity. Industrial processes in the sensor environment may produce background noise in the ultrasonic range. However, in general, this is less likely to be a problem at higher frequencies. The size and form of the target affects the intensity of the reflected sound burst. A large flat surface will reflect the whole beam and the received intensity is equivalent to the intensity at twice the target distance. An example of this type of situation is

measuring the level of a large vat of still liquid. When the target is not flat, a reflection coefficient may be calculated, which can be taken into consideration when selecting the sensor.

1.1.4 Inductive Sensors

There are two main types of inductive displacement sensor (IDS): those with one coil and those with more than one coil [2]. IDSs with two or more windings generally consist of a transmission coil and one or more receiver coils. A conducting material positioned between the coils will result in a change in the flux measured by the receiving loop. The general configuration is to have two coils facing each other with a conducting bar that is free to move between them. Thus by moving the conducting bar and monitoring the receiving loop impedance, a displacement can be determined. This type of sensor has been utilised in a number of applications for example by Bartoletti et al. [5] who use such a device in a low-noise accelerometer for the detection of gravitational waves.

The second type of inductive sensor with one coil can be utilised for non-contact displacement measurements. Such devices generally comprise a main sensor coil from which distances are measured and an oscillator / demodulator electronic module as shown in figure 1.2. The output of the system is a voltage that is directly proportional to the distance being measured. This type of sensor is used widely in the measurement of the distance to conducting targets in harsh environments because they are not affected by dust, dirt, humidity etc. between the sensor and target and because they can be enclosed in a protective casing to allow operation at high temperatures.

1.1.5 Comparison of Technologies

The technologies of capacitance, optical, ultrasonic and inductive displacement sensors have been discussed and their relative merits and shortcomings offered. In the context of a harsh industrial environment — where the measurement gap may be inconsistent and contaminated with particles of dust, oil, etc. — it is apparent that eddy current inductive displacement sensors are the most useful. Capacitance-based sensors are limited by their dependence on the permittivity of the dielectric between the sensing plate and the target material. A more detailed comparison between capacitive and inductive sensors is offered by Welsby [6]. Although laser-based optical displacement sensors offer an increased reliability compared to LED and photodiode systems, they are still limited by particles in the sensing gap. IDSs are well suited for harsh environments, but this type of sensor is not without limitation and the work presented here has focused on these devices and research into improving them.

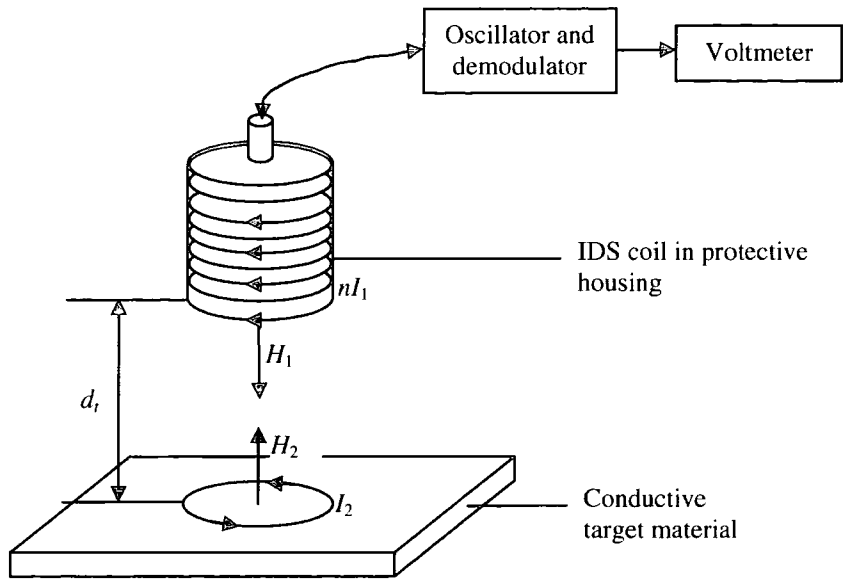

Figure 1.2. The Physical arrangement of an IDS.

1.2 Inductive Displacement Sensor Principles

Figure 1.2 shows how an alternating current, I_1, passes through the IDS coil to generate an alternating magnetic field, H_1. When a conducting target is positioned in the field, eddy currents are generated on the surface and this produces a secondary magnetic field, H_2, which opposes H_1.

1.2.1 IDS Coil Impedance

The equivalent circuit of the IDS system consists of two loops: the IDS coil and the induced eddy currents in the target. This arrangement is shown in figure 1.3. A change in the current of loop one results in a change in the flux through that coil. Loop one and loop two are magnetically coupled and so a potential difference is induced in the target material. The induced voltage, V_2, is proportional to the rate of change of the flux and thus the rate of change of the current in loop one, I_1, such that

$$V_2 = -M_{12}\frac{dI_1}{dt} \tag{1.2}$$

where M_{12} is the coupling constant between loop one and loop two, called the mutual inductance, which depends on the geometrical arrangement of the IDS coil and the target. M_{21} can be used to quantify the magnetic coupling between loop two and loop one. In general these two mutual inductances are equal since loop one and loop two may be interchanged without affecting the mutual inductance. Thus the mutual inductance is

$$M = M_{12} = M_{21} \tag{1.3}$$

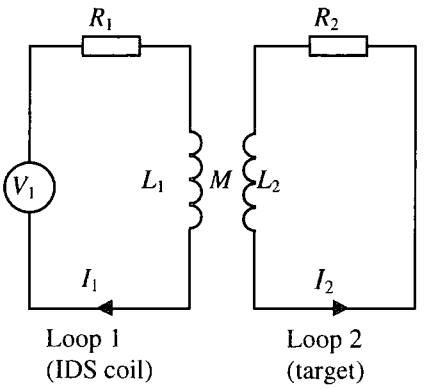

Figure 1.3. IDS equivalent circuit.

Figure 1.3 shows that each loop has an inductance (L_1 and L_2) and resistance (R_1 and R_2). The potential difference across the sensor coil with a current of angular frequency, ω, is given by Kirchoff's voltage law as

$$V_1 = R_1 I_1 + i\omega L_1 I_1 - i\omega M I_2 \tag{1.4}$$

where $i = \sqrt{-1}$. But for the second loop there is no overall potential difference and so

$$V_2 = R_2 I_2 + i\omega L_2 I_2 - i\omega M I_1 = 0 \tag{1.5}$$

Combining these two equations gives an expression for the potential difference across the IDS coil

$$V_1 = I_1\left[R_1 + \frac{\omega^2 M^2 R_2}{R_2^{\,2} + \omega^2 L_2^{\,2}} + i\omega\left(L_1 - \frac{\omega^2 L_2 M^2}{R_2^{\,2} + \omega^2 L_2^{\,2}}\right)\right] \tag{1.6}$$

from which the IDS coil equivalent impedance can be extracted

$$Z = R_1 + \frac{\omega^2 M^2 R_2}{R_2^{\,2} + \omega^2 L_2^{\,2}} + i\omega\left(L_1 - \frac{\omega^2 L_2 M^2}{R_2^{\,2} + \omega^2 L_2^{\,2}}\right) \tag{1.7}$$

This leads to frequency dependent equations for the IDS coil equivalent resistance

$$R = R_1 + \frac{\omega^2 M^2 R_2}{R_2^{\,2} + \omega^2 L_2^{\,2}} \tag{1.8}$$

and equivalent inductance

$$L = L_1 - \frac{\omega^2 L_2 M^2}{R_2^{\,2} + \omega^2 L_2^{\,2}} \tag{1.9}$$

1.2.2 The Skin Effect

An important result of the flow of eddy currents in the target material is the skin effect. This is the tendency of eddy currents to concentrate in the surface of the target closest to the excitation field. As the frequency of the excitation field increases, the skin effect increases and the currents become more concentrated at the surface. The effect is also dependent on the target conductivity and permeability. The amplitudes of the currents decrease exponentially — or approximately exponentially, depending on the geometry of the material — with depth into the target. Also with increased depth, the phase difference between the currents at that depth and the surface currents increases. An explanation of the skin effect is that eddy currents produce a magnetic field at a greater depth that counteracts the excitation field, thus reducing its ability to generate eddy currents deeper in the material.

Libby [7] (pages 123–135) shows that in the plane wave case, where a target of infinite extent is impinged upon by a perpendicular field of infinite extent, the current density J_z, at a depth z, is given by

$$J_z = J_0 \exp\left(-z\sqrt{\pi f \mu \sigma}\right) \tag{1.10}$$

where J_0 is the surface current density, f is the frequency and μ and σ are the permeability and conductivity of the target material respectively. For non-magnetic materials the permeability is that of free space, $\mu = \mu_0 = 4\pi \times 10^{-7}\ \mathrm{H.m^{-1}}$, otherwise $\mu = \mu_0 \mu_r$ where μ_r is the relative permeability of the material. A factor called the standard depth of penetration, or skin depth, can be introduced that is the depth where the current density has decreased to $1/e$ times its value at the target surface. Therefore (1.10) may be written as

$$J_z = J_0 \exp\left(-\frac{z}{\delta}\right) \tag{1.11}$$

where $\delta = (\pi f \mu \sigma)^{-1/2}$ is the standard depth of penetration. Figure 1.4(a) shows this variation of eddy current density with depth into the target. The axis of abscissas has the depth relative to the standard depth of penetration and the axis of ordinates has the current density relative to the surface current density.

The phase difference in radians, θ, between J_0 and J_z is given by

$$\begin{aligned} \theta &= z\sqrt{\pi f \mu \sigma} \\ &= \frac{z}{\delta} \end{aligned} \tag{1.12}$$

Figure 1.4(b) show a plot of the phase lag with depth into the target material. The axis of abscissas has the depth relative to the standard depth of penetration and the axis of ordinates has the phase difference between J_x and J_0.

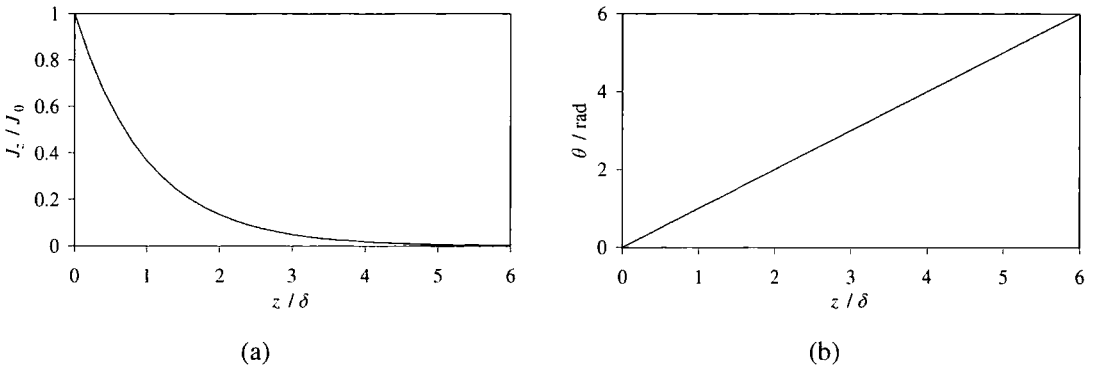

Figure 1.4. Variation of eddy current properties with depth in the plane wave case. (a) Eddy current density as a function of depth. (b) Eddy current phase angle as a function of depth.

1.3 Inductive Displacement Sensor Applications

IDSs may be used in a wide variety of applications ranging from simple distance measurement to vibration alarms. The electromagnetic nature of IDSs means that they are not affected by dust, humidity, etc. and may be employed in applications where other technologies — such as ultrasonic sensors — are not appropriate. Some example applications are detailed in table 1.1.

Aknin et al. [8] describe the use of an IDS in the railway industry for the measurement of the relative lateral displacement of a rail/wheelset or rail/bogie. Specific applications given are: "the measurement of the track gauge at high speed, the measurement of the yaw angle and lateral motion of a bogie, and finally the active steering of the railway wheelset". The device was expected to operate with rain, frost, snow, rapid cooling of the device when entering tunnels, large acceleration forces and the possibility of one side being heated through sun exposure and the other remaining cool in shadows. Optical sensors were ruled out because of mud, chips, metal filing and grease splashes, and capacitive sensors were unfeasible because of the large displacement that was required to keep the sensor clear of guard rails, level crossings, etc. Hence an IDS array was found to be the most suitable system.

Table 1.1. Example applications for IDSs.

Application	Description
Alignment	Two IDSs positioned perpendicularly around a joint can be used to show the position of a metallic rod during an alignment process.
Cylinder diameter	Two IDSs diametrically positioned towards the cylinder (e.g. a shaft) can be used to measure the diameter if the separation of the IDSs is known first.
Non-conductive material thickness	Place the test material on a conducting base and the ECS on the upper side of the material.
Part sorting	Metallic parts on a conveyor system can be sorted by their height over the surface.
Vibration measurement or alert	Both the amplitude and frequency of vibrations in a metallic object can be recorded. The maximum frequency will be limited by the response times of the electronics and the operation frequency of the coil.

An inductive proximity sensor is described by Sharp and Pater [9] for use in a nuclear facility to provide status information on moving machinery. Although this paper refers specifically to proximity sensors rather than displacement sensors, the same principles are applicable. The authors describe the benefits of using these sensors in a nuclear facility where the reliability of remote sensing equipment has important safety implications. Although standard inductive sensors are generally reliable, when subjected to ionising radiation they can fail at relatively low and unpredictable total doses. By redesigning the electronic circuit and selecting cables with appropriate specifications, a sensor with radiation tolerance was developed. The tested sensor has been manufactured by AEA Technology and has found applications in the thermal oxide reprocessing plant at Sellafield. Some further applications of IDSs are given towards the end of this chapter in section § 1.5.

1.4 Limitations of IDS

Eddy current IDS have a number of limitations and it is the purpose of this thesis to discuss these restrictions on their reliability and applications. Section § 1.2 has introduced the theory of operation for IDSs, which forms the basis of why target material affects the output of the sensor. Other factors affecting the reliability of IDS measurements are the target width and target offset. These factors place important limits on the range of applications in which IDSs can be employed.

1.4.1 Target Material

Equation (1.7) shows that the equivalent impedance, Z, of the sensor coil depends on the angular frequency, ω, and thus the frequency, f, of the current I_1. The resistance of the eddy current path, R_2, is a function of the resistivity of the target, ρ, and inductance of the target

depends on the permeability of the target, μ. Also, as mentioned in section § 1.2, the mutual inductance, M, varies with the geometry of the coil and target arrangement and so it is a function of the target displacement from the IDS coil, d_t. Thus Z is a function of all these factors, i.e.

$$Z = g(d_t, f, \rho, \mu) \tag{1.13}$$

For eddy current displacement sensors, f, ρ and μ must be controlled to give the single variable function

$$Z = g(d_t) \tag{1.14}$$

The frequency may be controlled by selecting a suitable value at the design stage that will depend on the target skin depth as described in section § 1.2.2. However, ρ and μ are properties of the target material and vary between, for example, steel and aluminium (see table 4.1). This target dependence can be a major limitation of an eddy current IDS and in situations where different targets need to be measured, the IDS needs to be recalibrated each time. Commercial IDSs are usually optimised for either magnetic or non-magnetic targets and it is difficult to use a system tuned for non-magnetic materials with a magnetic target. Indeed manufacturers state that with some smaller sensors it is impossible to use a mismatched target and system as the electronic circuits are optimised for the specific application.

1.4.2 Target Width

The ratio of target size to sensor coil diameter is an important consideration when selecting an IDS system. Sensor coils can be either shielded or unshielded depending on the application; the flux from unshielded sensors tends to extend laterally beyond the coil diameter, whereas the flux from shielded sensors does not tend to spread out in this way. The linear measuring range is directly proportional to the sensor coil diameter with unshielded coils having a greater measuring range than shielded coils. A manufacturer's IDS operation manual [10] states that for shielded sensors the target should be a minimum of 1.5–2 times the coil diameter, whereas for unshielded sensors the target material must be at least 2.5–3 times the coil diameter. Using an IDS with targets smaller than the specified widths will lead to degradation in linearity and long-term stability. However a target of size greater than the required minimums does not affect the system.

1.4.3 Target Offset

The influence of an offset target, that is a target that is displaced laterally relative to the centre of the IDS coil, is related to that of target width. When a target is offset, it appears to be smaller

than the required width on the side which has been moved towards the centre of the coil. This situation can arise where either the target has moved off-centre or the IDS coil has been displaced laterally.

1.5 Context

IDS technology is well established and much of the current research is based in the sensor manufacturing industry. For this reason trade journals can provide a useful insight into the current market and commercially available technologies. For example, an introduction to these sensors is presented by Welsby and Hitz [11] and the techniques required to design and build an eddy current IDS are given by Roach [12]. Besides this, there are also a number of published works that detail the modelling and improvement of IDSs, from which principles and theories can be extracted and applied to the work in this thesis.

The inhomogeneity resulting from different target materials is a major problem although only a small quantity of research on this matter has been published, such as that presented by Tian et al. [13] and Wang and Becker [14]. In the Tian et al. paper, the influence of target resistivity and permeability are investigated, as is the influence of the converting circuits. The work concludes, "...the effect of inhomogeneity in non-ferrous targets is much less than that of ferrous targets. Therefore non-contact displacement eddy current sensors are suited to applications for the precision measurement of non-ferrous targets." Wang and Becker have reported on their design of an IDS that gives a displacement that is described as being "practically independent of the material of the object".

There have been a number of reports of new designs and applications of IDSs, such as Passeraub et al. [15] who present a system that utilised a flat coil to achieve sub-micrometric sensitivity.

Research published by Bartoletti et al. [5] details "the design of a proximity inductive sensor". The aims of the work were to get low dimensions, a fast response to change in target displacement and low costs. The proximity sensor used flat coils that were constructed from a spiral design etched on a double-sided copper printed board. The advantage of this cheap process was that the coils were very thin and could therefore be placed in close proximity to the target. This was found to lead to greater sensitivity compared to the more usual design that extends laterally relative to the plane of the coil. The paper gives a qualitative discussion about the temperature dependence of their sensor, which is relevant to the work in this thesis; although the Bartoletti et al. descriptions are complicated by the fact tat they have used spiral coils.

Macovschi and Poupot have presented a two stage report on their study of variable inductance transducers as proximity sensors. The first part [16] describes the computer simulations of the magnetic circuits in a coil and target system, which were used to extract magnetic parameters. The magnetic field, the geometry and position of the coils, the permeability of the magnetic circuits and targets and the saturation of the magnetic circuits were studied. The simulations were used to compare two different coil core designs and in the second part [17] one of the designs was selected for experimental investigation. Results were presented for the variation of coil inductance with a number of parameters including: position and geometry of the coils, magnetic circuit material, target thickness, coil frequency and some auxiliary construction elements.

A highly sensitive and compact sensor system utilising 1 mm diameter coils has been demonstrated by Passeraub [18]. The system also incorporated a new electronic interface that was surface-mounted onto a PCB to include short leads and a low component count. The result was a low-noise, high-sensitivity IDS. To demonstrate the system, it was used to control a stepper motor by detecting a 1 mm hole drilled in a rotating brass disc. This was shown to permit a well-defined numbering of the motor's steps and hence enabled more control of the motor.

Much work has been done to utilise eddy current-type sensors to measure profiles and outlines of metallic objects in a process called electromagnetic tomography. Peyton et al. [19] present an overview of this method, which includes operating techniques and some examples. Hardy et al. [20] used an eight by eight array of spiral coils to detect and recognise metallic objects. Each coil was an eddy current IDS and the 64 elements gave a total sensing area of 320×320 mm. The output of the system was a computer image which was used to identify metallic objects in the sensing range. Fenniri et al. [21] used an eddy current IDS to measure the distance to a conducting target and then utilised a deconvolution algorithm to extract the profile of the target surface. The system was only demonstrated for certain targets, although Fenniri et al. suggest that it could have been employed to make an image of simple-shaped profiles such as toothed gearings, which would allow for the detection of fractured edges. On similar lines, Passeraub et al. [22] utilise their highly sensitive small coil IDSs to determine metallic profile and material information of coins. They demonstrate their system by highlighting the difference in results from genuine and fake coinage.

Belloir et al. [23] describe a smart flat-coil eddy current sensor for metal tag recognition used to identify buried pipes. The tags were buried with utility pipes and nine configurations were used to give a unique identification to the utility type (e.g. water, gas, data cabling, etc.). The

intention was that workers were able to locate and identify pipes without needing to excavate investigation trenches. Although separate emission and receiving coils were used, this work is closely related to eddy current IDSs in that the metal tags affected the flux distributions such that they could be identified remotely. The system was further improved [24] and the authors state that they have reduced the risk of tag misidentification to nearly zero. This work gives useful insights into hardware and signal processing considerations for IDSs.

An interesting application of an IDS is to measure the position of diesel engine valves as presented by Marčič [25]. Previous work had involved fitting a sensor to the valve, which altered its mass and therefore affected the measurements being taken. However, Marčič's system uses two coils fitted around the valve that do not interfere with its operation. This is not an eddy current based IDS, but again the design processes given in the paper are relevant to the present work.

In Scarr and Zelisse's work [26] an eddy current system is used to measure the thickness of metallised films. The system relies on the skin effect in the target material to attenuate the incident flux. Results were obtained using just one coil and this operated in a similar manner to that described here in section § 1.2 and gave a response to target displacement as well as target thickness. However Scarr and Zelisse wanted a system that would provide thickness results independent of the target position. To realise this, two coils were used and the target material was positioned between them; one coil acted as a transmitter and the other as a receiver. The authors also describe a system where the two coils are on the same side of the target, with the receiver wrapped inside the transmitter.

On the subject of modelling magnetic displacement sensors, Johnstone and Peyton [27] describe the use of three-dimensional finite element simulations to evaluate the performance of a magnetic sensor system. The technique of using a quarter-geometry model is described and compared to the full geometry model. Methods to overcome problems associated with meshing errors are described and the model results are compared to experimental measurements. The system described by Johnstone and Peyton is quite different from the IDSs described in this thesis, although the paper's description of the modelling is useful. Huang et al. [28] have also used finite element analysis to model a displacement sensor. The paper describes how a three-dimensional model of two coils from a non-contact inductive system was constructed. The models helped the authors to understand the non-linear nature of the device and assisted in the optimisation of the design.

In summary, despite IDSs now being off-the-shelf devices, research continues in design optimisation, miniaturisation and the investigation of new applications. Related work on finite

element analysis provides a useful insight into the techniques required to produce reliable models of IDSs. There has been some investigation of the limitations of IDSs although these issues have not been fully resolved and still remain an important area of research.

1.6 Organisation of the Remainder of this Thesis

In this chapter the subject of IDSs has been introduced and compared to other sensor technologies. The performance of these different sensors in a harsh industrial environment has been discussed and it is argued that IDSs are most appropriate for measuring distances when the sensing gap is contaminated with dust, steam or oil, etc. Some general applications of IDS have been introduced and some specific applications have been given. A discussion of the physics of IDSs has been given, which not only presented an understanding of their operation, but also described why they are limited by their dependence on the target material. The other limitations discussed were the influence of target width and target offset. Finally there was a presentation of some references to previous published research on the subject of IDS applications and improvements, which sets this thesis in context.

It has been demonstrated that IDSs measure changes in their coil impedance and use this to determine the target displacement. It is the total field that affects the impedance and therefore local variations are neglected. The central contention of this thesis is that the structure of the field can reveal information that is not available from these simple impedance measurements. The remainder of this thesis describes research that confirms this hypothesis as axiomatic and utilises this information to address the current limitations of IDSs. Chapter two describes how measurements of the IDS magnetic field were made. A number of technologies were investigated and the most appropriate was selected for use in the subsequent experimental work. Chapter three shows how finite element analysis simulations were used to model the IDS and includes a discussion of the merits and applications of two- and three-dimensional schemes. The fourth chapter shows the results of experimental and practical work on the limitations of IDSs resulting from target material, target offset and target width. The final chapter forms a summary of the work and draws conclusions about the practicability of making improvements to IDS designs.

Chapter 2

Magnetic Field Measurements

Magnetic fields are central to the operation of IDSs and in this chapter methods for taking measurements of these fields are described. Magnetic sensing technology has a broad range in terms of both field strength and the physics involved; this was researched and the relative merits of different sensors were compared. An estimate of the field amplitude and frequency was made, which enabled suitable measurement devices to be identified. The application of both magneto-resistive and test coil devices was investigated and the most appropriate was selected. Signals were recorded using a digital oscilloscope and a Java application was developed to reduce the noise using a phase-locking technique. The result was a system that was appropriate for the field range and frequency of the IDS and this was subsequently applied to the experimental work described later in this thesis.

2.1 Magnetic Sensor Technologies

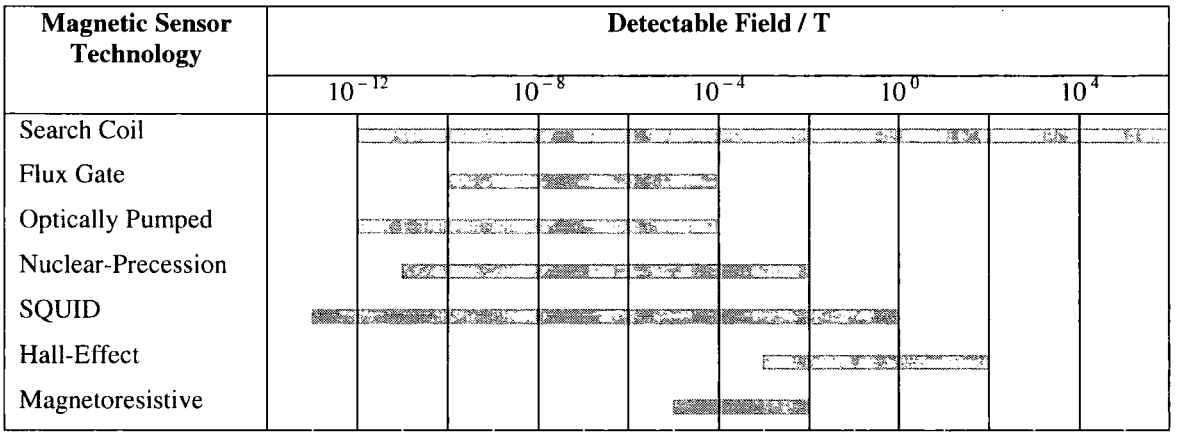

Figure 2.1. Comparison of typical magnetic field sensor approximate values. Adapted and updated from [29].

A variety of devices can be used to detect magnetic fields and the technology involved determines whether they are classified as low-, medium-, or high-field sensors [30]. Devices that detect magnetic fields $< \sim 10^{-10}$ T can be described as low-field sensors. Given that the magnitude of Earth's field is $\sim 5 \times 10^{-5}$ T, medium-field sensors which operate in the range $10^{-10} - 10^{-3}$ T, are referred to as Earth's field sensors. Detectors that measure fields $> 10^{-3}$ T

can be labelled as bias magnet field sensors. Figure 2.1 lists some devices and their associated typical approximate sensing ranges.

2.1.1 Low-field Sensors

It can be seen in figure 2.1 that a variety of low-field sensors exist. Application areas include measuring the neuro-magnetic fields in the brain and military surveillance equipment. However, these devices tend to be costly and bulky compared to other magnetic field sensors that are suitable for detecting stronger fields. It should be noted that the fields that are measured by these sensors are much less than Earth's field and so careful design choices must be made to ensure that the field of interest is preserved on the output signal. Some technologies suitable for measuring in this range are nuclear precession magnetometers, superconducting quantum interference devices and test coils.

Nuclear-Precession

Nuclear-precession magnetometers generally consist of a hydrogen-rich core surrounded by a coil. Current is passed through the coil to generate a DC magnetic field that aligns the spinning protons (hydrogen nuclei) like dipole magnets along the direction of the field. After the coil is turned off the protons are only subject to the magnetic field that is being measured. This field causes torque on the spinning nuclei and they precess around the direction of the field. Consequently a small alternating current is induced in the coil with a frequency equal to that of the precession. Since the field strength is proportional to the precession frequency, an accurate value for the magnetic field can be determined. Although this type of device can measure very low fields, it was deemed impractical for the application in hand. The same is true of optically pumped and fibre-optic magnetometers.

SQUIDS

Superconducting quantum interference devices (SQUIDs) [31] can detect magnetic fields over 15 orders of magnitude from several teslas to several femto-teslas. First developed in the early 1960s these devices utilise a Josephson junction and until recently required low temperatures to operate. Low temperature superconducting systems are not well suited to practical use outside the laboratory because of the sophisticated and expensive liquid helium (~ 4 K) cryogenics involved. However with the advent of (relatively) high temperature superconductor thin films SQUIDs have become more practical for testing purposes since they only require smaller and cheaper liquid nitrogen cooling (~ 77 K). Indeed the use of such high temperature SQUIDs has been demonstrated for enhancing eddy current non-destructive investigation of metallic structures [31]. However practical and low cost off-the-shelf SQUID systems are a long way off.

Test Coils

The list in figure 2.1 shows that test coils have a wide sensing range and can be used to measure low-fields. When a loop of wire is subject to an alternating magnetic field, Faraday's law of magnetic induction states that the EMF of the loop is equal to the negative of the rate of change of the magnetic flux through the area enclosed by the loop. For a coil of multiple loops, the EMF is simply multiplied by the number of turns. This is the basis of search coil magnetic field sensors. The sensitivity depends on the number of loops, the coil area and the permeability of the core. Since these devices rely on changing magnetic fields — or moving through one — they cannot be used to measure static or slow-varying fields.

2.1.2 Earth's Field Sensors

Given their sensing range, sensors in this group are typically used to measure the Earth's magnetic field. Example applications include using electronic compasses for navigation, determining the yaw of aircraft and projectiles and measuring variations in the field for road traffic measurements. Some technologies that fall into this range are fluxgate, magnetoresistive and Hall-effect sensors.

Fluxgate

Fluxgate sensors [32] can be used to measure DC or low frequency AC magnetic fields over the range $10^{-10} - 10^{-4}$ T. The usual configuration is called a second harmonic device, which comprises two coils formed on a common high-permeability core. An alternating current in the excitation coil periodically saturates the magnetic core and the permeability is modulated. The second winding is a sensing coil that couples with the excitation coil through the core. The external measured field also affects the core's permeability and a voltage proportional to the field strength is induced in the sensing coil at the second harmonic of the excitation frequency. Although standard fluxgates can detect AC magnetic fields they generally have an upper limit of ~ 1 kHz, although recent publications have claimed to have achieved a bandwidth of ~ 1 MHz.

Hall-Effect

A particle of charge, q, moving with a velocity, $\underline{v}$, in a magnetic field, $\underline{B}$, is subject to a Lorentz force

$$\underline{F}_L = q(\underline{v} \times \underline{B}) \tag{2.1}$$

which acts in a direction that is perpendicular to $\underline{v}$ and $\underline{B}$. The Hall Effect is the influence of the Lorentz force in a semiconductor material. A voltage applied across a block of semiconductor material causes a current to flow. If a magnetic field is applied perpendicularly to the current, then $\underline{F}_L$ will cause the charge carried to be deflected in the third dimension. This results in a

build up of charge and a potential difference is developed across the device in the direction perpendicular to the applied voltage and measured magnetic field. Hall sensors typically use n-type silicon for low-cost applications although other semiconductors such as InAs and AnSb can be used where greater frequency response and sensitivity are required. This enables easy integration with other semiconductor elements to create sensors integrated with controlling and processing electronics.

Magnetoresistive

The magnetoresistive effect is the property of a current-carrying ferromagnetic material to change its resistivity in the presence of an external magnetic field. Such a material is permalloy, which consists of 80 % nickel and 20 % iron and has a high magnetic permeability. Figure 2.2 shows the influence of an external magnetic field on the magnetisation of a strip of material such as permalloy. The device is arranged such that when there is no external magnetic flux, the current flows parallel to the magnetisation vector, $\underline{M}$. On the application of an external flux, $\underline{B}$, perpendicular to the current flow, $\underline{M}$ will rotate by an angle α, which changes the resistance by

$$R = R_0 + \Delta R_0 \cos^2 \alpha \tag{2.2}$$

where R_0 and ΔR_0 are material properties.

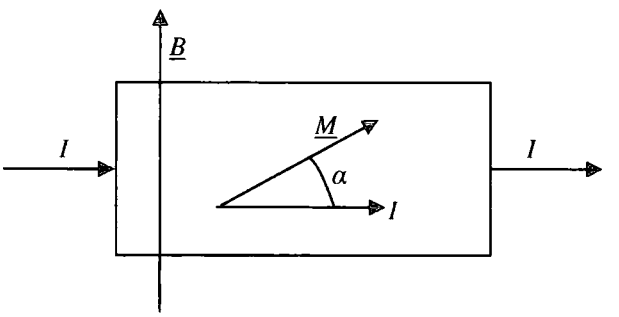

Figure 2.2. Magnetoresistive effect: a current, *I*, flows through a ferromagnetic material and an external magnetic flux, $\underline{B}$, causes the magnetisation vector, $\underline{M}$, to shift by an angle α.

2.2 Design Requirements

To gain an insight into which magnetic sensor technologies are suitable for the task in hand, values of the field magnitude and frequency were required. Initial investigations with a Hall probe gaussmeter were unsuccessful; no changes from the background readings were observed in either AC or DC modes. This was assumed to be because the gaussmeter had either too low a sensitivity or too slow a frequency response.

The simpler idea of using a single loop of wire around the end of the sensor barrel was more useful. The circuit was connected directly to a 20 MHz analogue oscilloscope to obtain a smooth trace (amplitude noise less than the thickness of the trace) with a period of 10^{-6} s, which is in agreement with the manufacturer's stated operating frequency of 1 MHz. The EMF across the loop had a sinusoidal form that varied with time, t, as

$$V = V_0 \sin(2\pi f t) \tag{2.3}$$

where V_0 is the amplitude and f is the frequency. Faraday's law gives the relation to the magnetic flux, ϕ_m, through the loop as

$$V = \frac{-d\phi_m}{dt} \tag{2.4}$$

with

$$\phi_m = BA \tag{2.5}$$

where B is magnetic flux density and A is the area of the loop. This leads to an expression for B

$$\begin{aligned} B &= -\frac{1}{A}\int V(t)dt \\ &= -\frac{V_0}{A}\int \sin(2\pi f t)dt \\ &= \frac{V_0}{A2\pi f}\cos(2\pi f t) + \text{constant} \end{aligned} \tag{2.6}$$

When the EMF is at a maximum or minimum, the field is changing at its fastest rate (corresponding to $B = 0$), so there is no offset and the integration constant is zero, thus

$$B = B_0 \cos(2\pi f t) \tag{2.7}$$

with the amplitude of the field

$$B_0 = \frac{V_0}{A2\pi f} \tag{2.8}$$

With no target present the EMF across the loop was measured as 0.134 V, so using the barrel diameter of 73.7 mm gives an estimate for the field amplitude $B_0 \sim 5 \times 10^{-6}$ T.

The coil can be modelled as a solenoid such that the flux inside the coil is constant except near the edges where its magnitude decreases as the field lines diverge. The test loop was fitted near the end of the sensor barrel and so an estimate of the magnitude of the current in the coil, I_0, can be estimated by the simple function

$$I_0 \approx \frac{2B_0}{n\mu_0} \tag{2.9}$$

where μ_0 is the permeability of free space and n is the number of turns in the coil per unit length of the coil; this assumes a one-layer thick coil. Using the estimate of B_0 gives the estimate $nI_0 \sim 10$ A.turns.m^{-1}. If the coil has, say, 1000 turns and is approximately 8 cm long, then the current in the coil, $I_0 \sim 10^{-3}$ A, which is a reasonable value that gives confidence in the suitability of the B_0 estimate.

2.3 Magneto-Resistive Sensor

The equation describing the rotation of the magnetisation with applied field (2.2) shows that the magnetoresistive (MR) effect is non-linear. The effect can be linearised by depositing aluminium stripes — so called Barber poles — on top of the permalloy at 45 ° to the strip axis. The conductivity of aluminium is larger than the permalloy and so the strips rotate the current direction through 45 °. The current follows a zigzagged pattern which effectively changes the angle of rotation of the magnetisation relative to the current from α to $\alpha - 45$ °. For the Philips KMZ series of MR sensors four permalloy strips are arranged as the arms of a Wheatstone bridge arrangement. For two diagonally opposed strips the Barber poles are at + 45 ° and – 45 ° to the strip axis. When an external magnetic field is applied, as the resistance increases in one pair of strips it is matched by a decrease in resistance in the other pair. The result is a bridge imbalance that is linearly related to the magnitude of the applied magnetic field.

Philips state that their KMZ10A thin-film permalloy MR sensor is suitable for a wide range of applications including navigation, current and field measurement, revolution counters, angular and linear position measurement and proximity detectors [33]. The navigation using Earth's magnetic field (~ 5×10^{-5} T) was of interest because the estimate of B_0 given in the previous section (§ 2.2) is just an order of magnitude less (~ 5×10^{-6} T). It was anticipated that with suitable amplification circuitry these devices could be used to measure the field. The KMZ10A devices were selected because of their availability and the fact that they are quoted as being capable of operating at 1 MHz.

2.3.1 Amplification Circuit

As a quick trial the MR device was tested by connecting it directly to a power supply and an oscilloscope. This demonstrated that the device was functioning normally and a reading was obtained when a magnetised screwdriver was placed in its vicinity. However to detect weaker fields an amplification circuit must be used; the Philips data sheet [33] gives a basic application circuit which was constructed on a PCB. The circuit allows for sensor offset and sensitivity

adjustment, as shown by the circuit diagram of figure 2.3. Temperature drift is an important consideration and the circuit diagram shows the use of a compensatory silicon device with a positive temperature coefficient (R6). However, this device could not be sourced, so by plotting the expected resistance response to temperature a suitable resistor was found to optimise the circuit for the laboratory temperature.

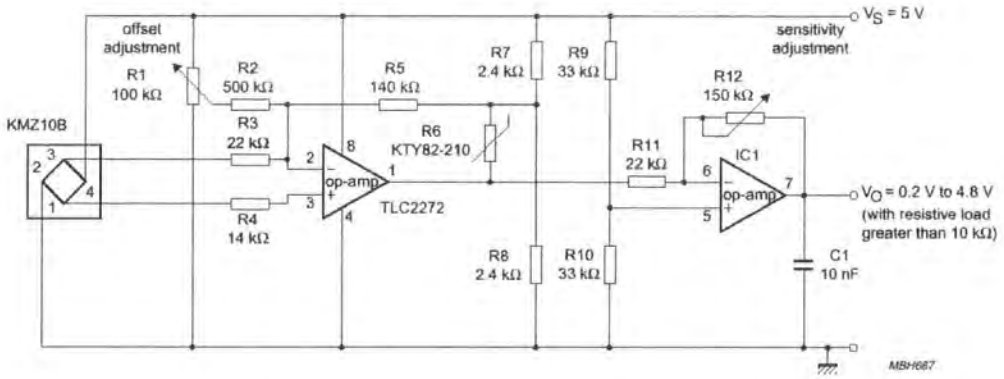

Figure 2.3. Amplification circuit used with the MR sensors. Adapted from [33].

The PCB was double sided and space between tracks was left un-etched and grounded to reduce noise levels and the resulting circuit is shown in the figure 2.4.

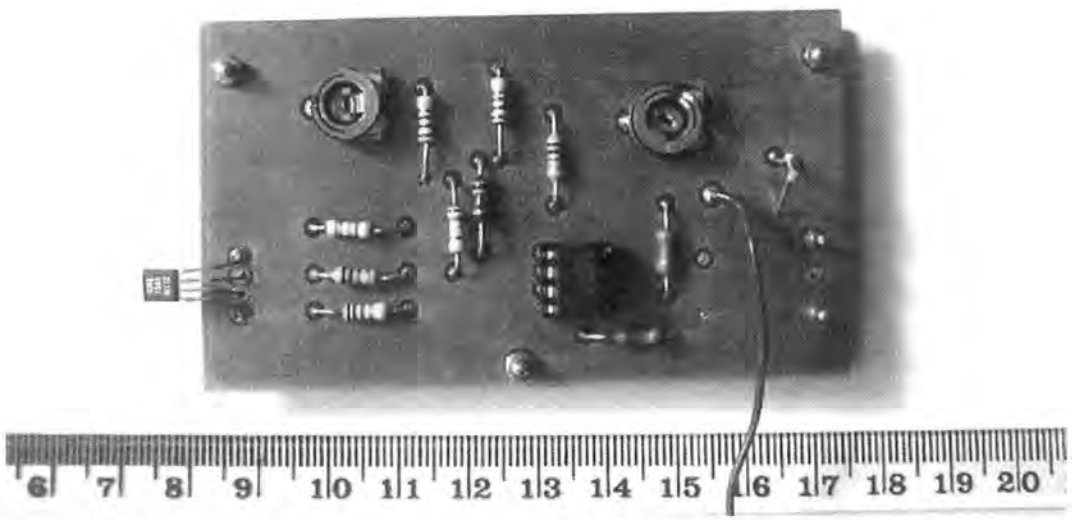

Figure 2.4. Constructed amplification circuit with the MR sensor protruding from the left-hand edge.

2.3.2 Circuit Testing

The circuit was tested by connecting the output to an oscilloscope and moving a magnetic field from a screwdriver in the vicinity of the MR sensor. The result was a response at a higher amplitude voltage level than was obtained with the circuit in the previous section (§ 2.3.1), as would be expected. However, when the MR sensor was placed near the IDS coil, no response was noticeable above the background noise levels. There were two possible reasons for this, firstly the circuit may not have been sensitive enough and secondly the frequency of the IDS coil may have been too high for the sensor to detect.

To investigate the frequency response of the MR sensor, the IDS coil was removed from the usual oscillator/demodulator circuit and connected to a frequency generator. The IDS coil was placed above the MR sensor, but no response was found at any frequency. At 1.00 MHz the coil voltage was 427 mV and the influence on the field sensor as monitored on the oscilloscope was a low-level background noise (~ 1.0 MHz, ~ 1.26 mV). At 400 kHz the coil voltage was 182 mV and there was no distinguishable effect over the background noise (~ 3.4 MHz, ~ 2.5 mV). The lower coil voltage is a result of a shift down from the resonance frequency of the coil. Similar experiments using a different coil with a much lower resonance frequency of 35 kHz also failed to yield a useful signal response. It is suspected that the low voltage and current provided by the signal generator produced a field of insufficient intensity for the MR sensor to detect. The KMZ10A data sheet shows that the response to magnetic field decreases as the frequency increases, so the lack of response from the circuit was likely to be a result of the combination of low amplitude and high frequency. Hence this device was shown not to be appropriate for this application.

2.4 Test Coil Sensor

Besides the MR sensor, the other magnetic field sensor identified in § 2.1 that fulfils the requirements of § 2.2 is the test coil. Equations (2.3) to (2.8) can be used to determine the amplitude B_0 given a measured potential difference (V_0) across the test coil. However, since the coil consists of multiple loops, the total flux is that passing through an individual loop multiplied by the number of turns in the coil, N. Therefore the magnetic flux density can be determined from the measured EMF by

$$B_o = \frac{V_0}{AN2\pi f} \tag{2.10}$$

A simple test coil was formed by wrapping 26 gauge (0.4038 mm) enamelled copper wire in 28 turns around a plastic former of diameter 11 mm and length 10 mm. A glass capillary tube

was used as a holding support for the tube and the signal wire passed though the middle and out the end to an oscilloscope. The coil is conducting, but it does not interfere with the operation of the IDS since it is stranded and therefore eddy currents cannot be generated in it. However, it is not possible to measure a physical quantity from a system without affecting the system itself. In this situation, the coil takes energy from the field and will have some influence on the system.

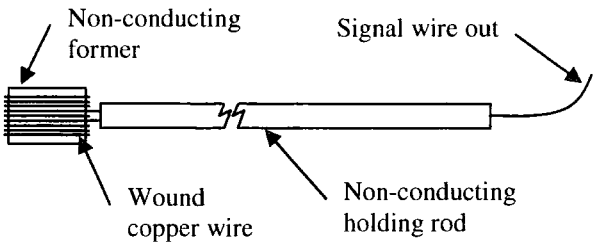

Figure 2.5. Simple test coil construction.

Placing the test coil below the IDS coil produces a clear sinusoidal signal with a 1 MHz frequency. Immediately below the sensor coil the magnitude of the potential difference across the test coil was recorded at 84 mV; corresponding to $B_0 = 5.0 \times 10^{-6}$ T. The values given by the test coil are in agreement with the estimates in § 2.2.

2.5 Selection and Refinement of Test Coil

It can clearly be seen that the results from the test coil are much more stable and well defined than from the MR sensor. Test coils are well suited to measure the AC magnetic fields generated by the IDS coil since Faraday's law relies on changing fields to generate a potential difference. This effectively eliminates the static background effect of Earth's magnetic field.

The test coil was used to measure the magnetic flux density profile of the IDS coil, as shown in figure 2.6. The test coil was positioned immediately below the IDS coil and the vertical component of the flux recorded at different displacements from the centre position. It can be seen from this profile that, as expected, the field is strongest in the centre and decreases outwards. At the edges of the IDS coil, the field drops by an order of magnitude and at a displacement of 35 mm from the centre — which corresponds to the edge of the IDS coil — the field is 36 % of the centre value. Beyond 35 mm the flux density was very small and with the trial test coil the signal was lost in the background noise. Consequently careful design of the test coil was required to give strong coupling to the IDS coil.

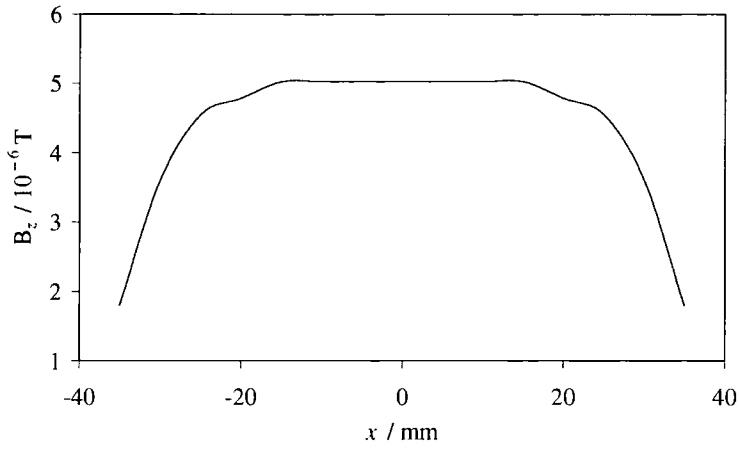

Figure 2.6. Magnetic flux density profile of the IDS coil as measured with the test coil.

2.5.1 Test Coil Construction

The test coil described in § 2.4 was refined to give a stronger signal towards the edge of the IDS coil. The use of a core with a high permeability would increase the potential difference across the test coil but this would interfere with the operation of the IDS since eddy currents can be generated in the material. Another way to increase the signal is to increase the total area of the coil by increasing the number of turns or the diameter of the core. A good coil has a large number of evenly-spaced, tightly-wound loops.

The test coil design process went through many stages before a final refined option was developed. Test coil 'a' shown in figure 2.7 was constructed using 32 gauge (0.2032 mm) enamelled copper wire with an air core and was held together with wire braces. It was found that the wire braces produced spikes on the signal and so coil 'b' was constructed in a similar way, but was held together with masking tape. For both of these designs the intention was for a flat sensor, so that only the vertical component of the field was detected. Their actual height was ~ 2 mm, which limited the number of turns to ~ 40 and so a strong signal could not be obtained. More turns were introduced in test coils 'c' and 'd' which had lengths of ~ 6 mm and were constructed on paper formers. These test coils had approximately 80 turns and produced clear signals with improved amplitude. Coil 'e' demonstrated the use of finer 40 gauge (0.0787 mm) wire enabling a higher turn density.

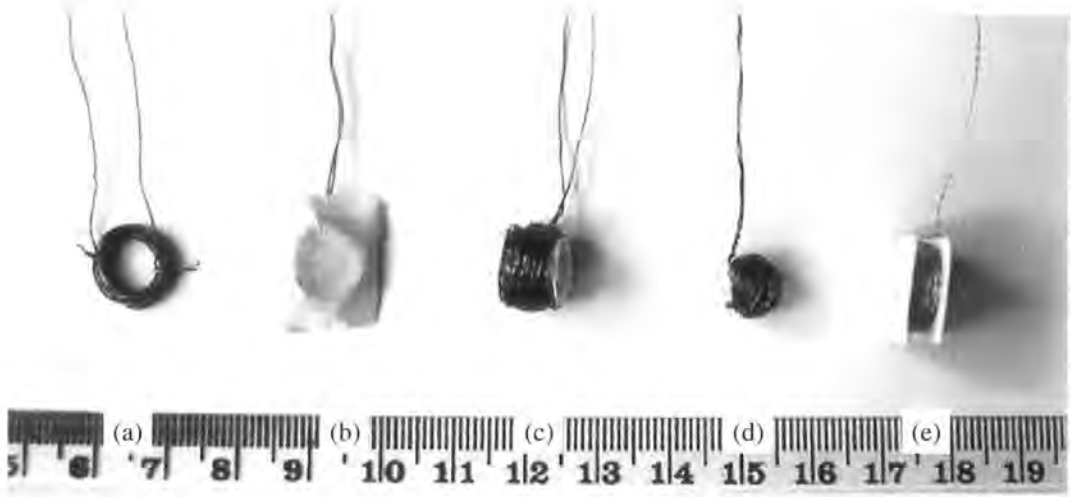

Figure 2.7. Different coil designs.

During the development of test coils 'a'–'d' marked improvements in signal to noise ratios and sensitivity were recorded, however these coils were flimsy and were not suitable for making a large number of measurements. The final test coil 'e' in figure 2.7 was a much improved design that utilised a non-conducting solid core and two end pieces to hold the wire in place; the construction is shown in figure 2.8. The test coil had 200 turns which gave a voltage of 240 mV at the centre of the IDS coil.

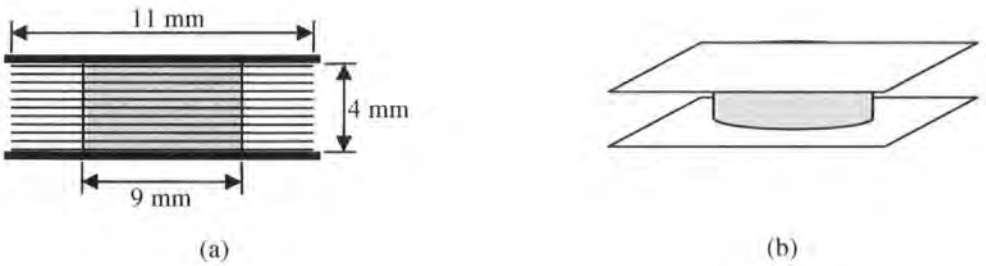

Figure 2.8. Optimised test coil design. (a) Side view. (b) Projection view.

2.5.2 Test Coil Characterisation

The impedance of the test coil was measured using an Agilent 40 Hz – 110 MHz impedance analyser. This device sweeps through a range of frequencies to determine impedance as a function of frequency, as shown in figure 2.9. The peak in impedance magnitude of 113 kΩ is at 1.38 MHz, which also corresponds to the point where the impedance phase changes from + 90 ° to – 90 °. Note that this is a peak in the complex magnitude of the impedance and does not correspond to a resistive peak.

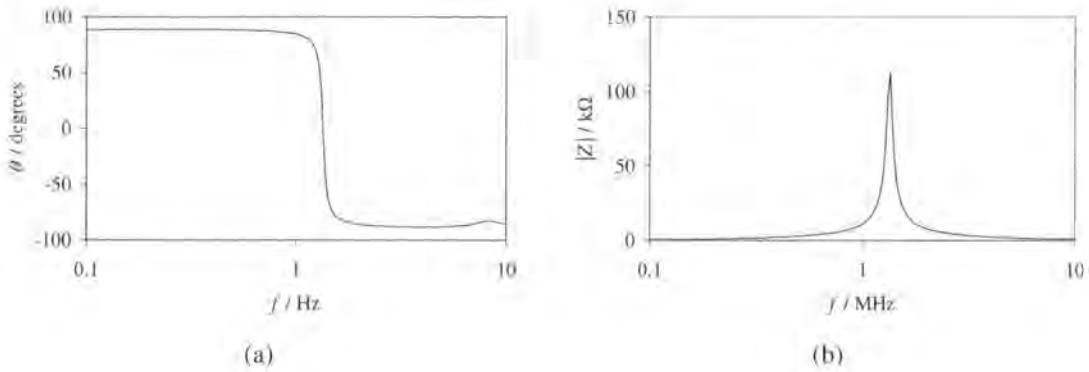

Figure 2.9. Impedance analysis of the test coil. (a) Impedance phase angle θ. (b) Impedance magnitude $|Z|$.

The form of figure 2.9 indicates that the coil is a parallel R, L and C circuit as shown in figure 2.10 and the peak corresponds to parallel R, L and C resonance. The resistance, R, results from the length of wire, the coil loops result in an impedance, L, and the capacitance, C, is the consequence of charge building between loops. The impedance of the coil, Z, can be regarded as the opposition to current flow, I, such that the potential difference across the inductor is $V = IZ$. The inductive element of the coil impedance is $X_L = i\omega L$, where $i = \sqrt{-1}$, ω is the angular frequency of I and L is the inductance. The capacitive element of the impedance is $X_C = 1/i\omega C$, where C is the capacitance. The admittance, Y, is defined as the reciprocal of impedance, i.e. $Y = 1/Z$, and for the parallel LR and C circuit is given by

$$\begin{aligned} Y &= \frac{1}{R + i\omega L} + i\omega C \\ &= \frac{R}{R^2 + \omega^2 L^2} + i\left(\omega C - \frac{\omega L}{R^2 + \omega^2 L^2}\right) \end{aligned} \tag{2.11}$$

In polar form, $Y = |Y|\varphi$, this is

$$\begin{aligned} |Y| &= \sqrt{\frac{R^2}{\left(R^2 + \omega^2 L^2\right)^2} + \left(\omega C - \frac{\omega L}{R^2 + \omega^2 L^2}\right)^2} \\ \varphi &= \arctan\left[\left(\frac{R^2 + \omega^2 L^2}{R}\right)\left(\omega C - \frac{\omega L}{R^2 + \omega^2 L^2}\right)\right] \end{aligned} \tag{2.12}$$

At resonance the phase angle, φ, is zero and equation (2.12) shows that this is when

$$\omega C = \frac{\omega L}{R^2 + \omega^2 L^2} \tag{2.13}$$

and thus the resonant frequency is

$$\omega_0 = \sqrt{\frac{1}{LC} - \frac{R^2}{L^2}} \tag{2.14}$$

At resonance when the phase angle is zero, the impedance is entirely real and thus from equation (2.11) and using equation (2.13)

$$Y = \frac{R}{R^2 + \omega_0^2 L^2} = \frac{R}{L/C}$$
$$Z = \frac{L}{RC} \tag{2.15}$$

The AC resistance is much higher than the DC resistance because of the skin and proximity effects. Passing a direct current through the test coil reveals that $R = 13.3\ \Omega$. Substituting this value and the resonance data from figure 2.9 into equation (2.15) gives a values of $L = \frac{1}{\omega_0}\sqrt{ZR - R^2} = 8.8 \times 10^{-4}$ H and $C = L/RZ = 5.9 \times 10^{-10}$ F.

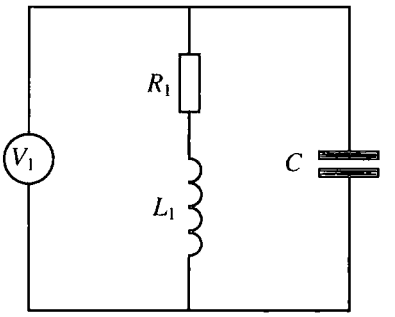

Figure 2.10. Parallel R, L and C circuit model of test coil.

2.6 Collection of Data

With the test coil designs completed, it was then appropriate to test the collection of data. Initial tests revealed low level noisy signals and efforts were made to improve them using a phase-locking technique.

2.6.1 Signal Noise

The test coils were connected to an Agilent 500 MHz 2 GSa.s^{-1} digital oscilloscope and the traces were recorded. The recorded signals were found to be subject to noise and fluctuations

that made them difficult to use. Figure 2.11(a) demonstrates the fluctuations over 200 cycles with a sample rate of 100 MSa.s^{-1} and it is clear that there is not a smooth signal as the amplitudes vary from 2.5× 10^{-3} – 7.5× 10^{-3} V. Figure 2.11(b) shows high frequency noise on the signal over 10 cycles.

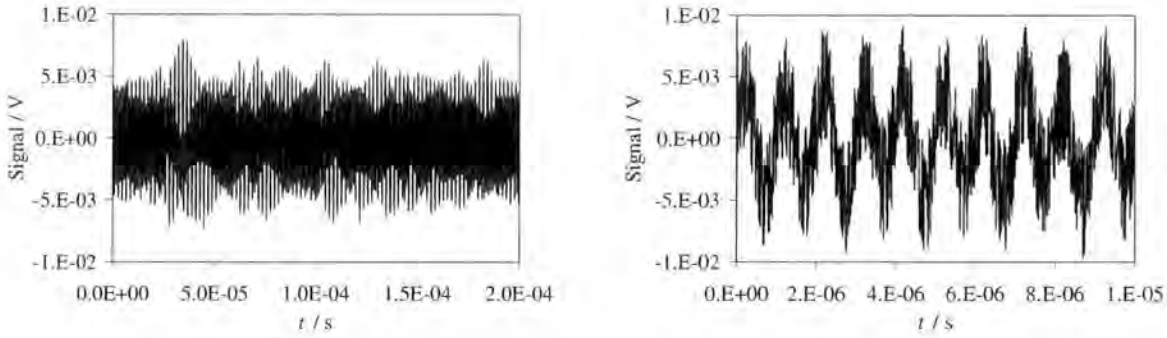

Figure 2.11. Signal recorded from a test coil. (a) Global variations. (b) Local variations.

To clean up the signal, the digital oscilloscope includes an averaging facility that takes the mean of repeating functions. However this was not used because it was expected that in practical use, the amplitude of the field would vary over time and this information would be lost in the average. So a phase-locking technique was employed, which relies on knowing the basic form of the signal that is being measured. The noisy time-dependant input signal $g(t)$ is compared to a known smooth time-dependant reference signal $f(t)$ by means of a general correlation function

$$R(\delta)=\lim_{t\to\infty}\frac{1}{T}\int_0^T f(t)g(t+\delta)dt \tag{2.16}$$

which relates f and g for a time parameter δ and where T is just the upper integration limit. R is zero when $f(t)$ and $g(t)$ are independent. Generally $g(t)$ is modulated in some way by the reference $f(t)$. In the case of the IDS the signals are known to be periodic sine functions with amplitudes a_1 and a_2 and of frequency ω, thus the correlation function becomes

$$\begin{aligned} R(nT,\phi) &= \frac{a_1 a_2}{nT}\int_0^{nT}\sin(\omega t)\sin(\omega t+\varphi)dt \\ &= \frac{a_1 a_2}{2}\cos\varphi \end{aligned} \tag{2.17}$$

which has an upper integration limit of nT where T is the period of the frequency ω and n is an integer. φ is the phase difference between $f(t)$ and $g(t)$. For complete correlation R is taken as unity and if the amplitude of $f(t)$ and the phase difference are known, the amplitude of the signal may be determined. This technique is appropriate to the test coil signal because the signals are small, periodic and noisy.

Lock-in amplifiers apply phase-locking and can be used to reduce the noise on a signal where there is a clear reference. A lock-in amplifier was tested and a smooth reference signal was taken from several loops of wire wrapped round the IDS barrel. However it was found that this instrument was not suitable for the high frequency signal from the IDS and on further investigation revealed that 1 MHz devices are uncommon.

2.6.2 Phase-Locking Program

Given the inability of the hardware lock-in amplifier to resolve the signal, an offline software solution was investigated. The digital oscilloscope was able to record actual values from the signal which enabled the development of a Java application to phase-lock the recorded signal. The signals were stored as text in comma separated value (CSV) formatted files. The program extracted data from a specified file and proceeded to multiply the signal and reference together. The product was then integrated and the resulting amplitudes plotted on the graphical user interface (GUI). The phase difference between the signal and reference was adjusted by moving a sliding bar and both an average amplitude and amplitude variance were calculated. Figure 2.12 shows a screenshot from the program. An optimisation method was developed to find the phase that gave the minimum amplitude variance i.e. the smoothest output signal. The resulting amplitudes array could then be saved to a file in CSV format to enable display in a graphing or statistical package.

Figure 2.12. Screen-shot from the phase-lock Java application.

Figure 2.13 shows the result of phase-locking a noise signal with the program. Although it may appear irregular, it is smoother than the unprocessed signal. The average amplitude is of the unprocessed signal is 4.65×10^{-4} V with a variance of 4.39×10^{-7} V^2. The phase-locked signal has a mean amplitude of 0.0324 V with a variance of 1.12×10^{-7} V^2.

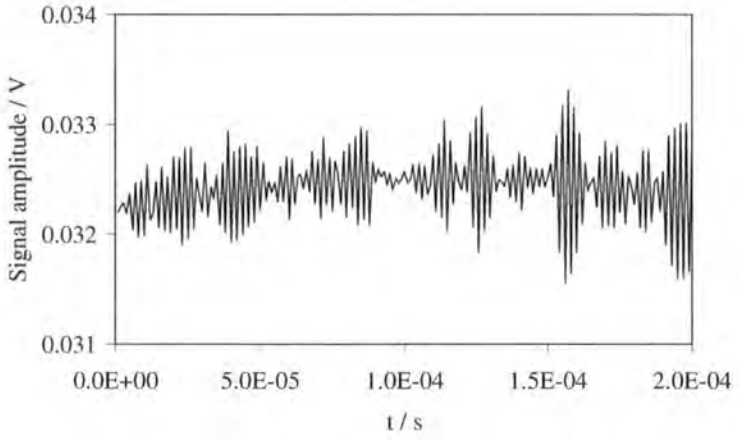

Figure 2.13. Result of phase-locking an input signal.

For practical purposes a second application was developed without the GUI to process the recorded signals in bulk. A list of input signal and reference files were given to the program that then opened the files, found the optimum phase difference and saved the resulting

amplitudes to an appropriate CSV file. With this program a set of readings from a whole experiment could be processed in one batch.

2.7 Summary

This chapter has described a number of magnetic field sensing technologies and has discussed their relative merits and suitability for measuring the field around an IDS coil. An initial investigation showed that the field oscillated in a sinusoidal manner with an amplitude of $\sim 5 \times 10^{-6}$ T and a frequency of 1 MHz. Magneto-resistive sensors and test coils were selected as being the most suitable devices to measure fields of this form. Initial investigations of a Philips KMZ10A M-R sensor were unsuccessful and this was attributed to a combination of the high frequency and low strength of the field. Trials of a test coil device were more fruitful and, after a number of refinements, a suitable coil was constructed. The signal from the test coil was found to be very clean at high field strengths, but for low field strengths ($< 2 \times 10^{-6}$ T) the low signal to noise ratio was found to be a serious issue. To address this problem, the signal was recorded with a digital oscilloscope and then a phase-locking program was built to extract the amplitudes from the noisy pattern. Before processing, an example signal was found to have a mean amplitude of 4.65×10^{-4} V with a variance of 4.36×10^{-7} V^2, but the phase-locking technique revealed an amplitude of 0.0324 V with a variance of 1.12×10^{-7} V^2. The result was a reliable system that could be used to measure the magnetic field around IDSs.

Chapter 3

Finite Element Analysis

In the first chapter it was hypothesised that small magnetic field changes that are not detected by coil impedance measurements can provide more information about the target material. The previous chapter described the development of a sensor that was suitable for measuring the small fields around IDS coils. This chapter leads on from this by describing how finite element analysis (FEA) was used to determine what field features can offer useful additional information. Firstly there is a description of the electromagnetic finite element modelling processes and how it was applied to the IDS coil and target arrangement. Both two- and three-dimensional models were constructed using a commercial software package and there is a discussion of the relative merits and applications of each. The models provided a large number of data, so a convolution program was developed to take the magnetic field solutions and extract measurements of a similar form to those taken by the test coil experiments.

3.1 Generalised FEA Modelling Process

Analytical solutions to eddy current problems are described by Dodd and Deeds [34] who give a quick and easy method for the calculation of observed effects. However, the solutions presented there are not appropriate for high frequencies. This is because as the frequency of current in a wire increases, the current density ceases to be uniformly distributed and tends to concentrate at the surface, which causes the coil resistance to increase and the inductance to decrease. This leads to an effect where the current tends to flow across the turns rather than through them and the capacitance between the coil and target increases. So given that an analytical solution is not available, numerical approximations are needed.

In general terms the finite element method is used for the solution of physical problems that are described by differential equations. The continuous domains of the problem are broken down into a finite number of elements. Chari and Silvester [35] and Silvester and Ferrari [36] describe the finite element method with particular reference to electrical and magnetic field problems.

There are a number of commercially available software suites that enable FEA of electromagnetic problems. Simulations for this thesis have used Ansoft's Maxwell software

suite, which consisted of two main programs that could be used to solve problems in two- or three-dimensions. The programs used FEA to numerically solve Maxwell's equations over a specified geometry and within user-defined boundary conditions. All simulations were completed on the same 2.2 GHz, 512 MB RAM PC with the Microsoft Windows XP (service pack one) operating system. Therefore it was possible to use the time taken to complete the FEA to compare the efficiency of various methods.

3.1.1 Setting Up the Simulation

The first stage of the modelling process is to construct the problem geometry to give the program the physical constraints within which the solution is to be found. Then the material properties such as the relative permeability, μ_r, relative permittivity, ε_r, and conductivity, σ, are entered; this may be done manually or common materials can be selected from a predefined catalogue. Following from that, sources and boundary conditions are entered, which define the problem to be solved. One or more of several so-called executive parameters may be selected, which are quantities such as force, torque, inductance, capacitance, or power loss. These parameters may arise as a result of fields generated by the sources and can be determined by the program. The program will then proceed to solve the problem through using a FEA method by generating a mesh and calculating the field solutions. Results can be extracted through the use of a post processor program that uses the field solutions to determine various properties such as magnetic field strength.

3.1.2 Impedance Simulation

The Maxwell software allows for the calculation of an impedance matrix, which summarises the relationship between AC voltages and currents in multi-conductor systems. For a two-conductor system, the equivalent circuit is shown in figure 3.1, which is a generalised form of that given in figure 1.3.

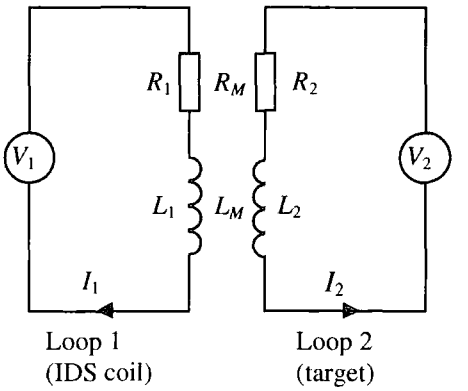

Figure 3.1. Equivalent circuit for a two-conductor system.

The potential difference across each loop are given by

$$V_1 = R_1 I_1 - R_M I_2 + i\omega L_1 I_1 - i\omega L_M I_2 \tag{3.1}$$

$$V_2 = R_2 I_2 - R_M I_1 + i\omega L_2 I_2 - i\omega L_M I_1 \tag{3.2}$$

This leads to the matrix expression

$$\begin{bmatrix} V_1 \\ V_2 \end{bmatrix} = \begin{bmatrix} Z_1 & -Z_M \\ -Z_M & Z_2 \end{bmatrix} \begin{bmatrix} I_1 \\ I_2 \end{bmatrix} \tag{3.3}$$

where $Z_1 = R_1 + i\omega L_1$ is the impedance of loop one, $Z_2 = R_2 - i\omega L_2$ is the impedance of loop two and $Z_M = R_M + i\omega L_M$ is the mutual impedance between loops one and two. For a system with n conductors, the impedance matrix contains $n \times n$ elements. Once the field solver has completed, the impedance solver can use the field values to calculate the inductance and resistance values separately before combing them into the impedance matrix.

The inductance is calculated from the average energy of the system, $\overline{U}$, which is given by the integral of the magnetic field density, $\underline{B}$, and magnetic field, $\underline{H}$, over the volume, V, of the problem, thus

$$\overline{U} = \frac{1}{4} \int_V \underline{B} \cdot \underline{H}^* \, dV \tag{3.4}$$

At any point in the current cycle, the energy of the system, U, is given by

$$U = \frac{1}{2} L I^2 \tag{3.5}$$

where L is the inductance and I is the current at a given in time. Integrating over the current cycle, gives a second expression for $\overline{U}$

$$\overline{U} = \frac{L}{2} I_{RMS}^2 = \frac{L}{4} I_{peak}^2 \tag{3.6}$$

where I_{RMS} is the root-mean-square current and I_{peak} is the peak of the current cycle. Thus the inductance can be determined from

$$L = \frac{\int_V \underline{B} \cdot \underline{H}^* \, dV}{I_{peak}^2} \tag{3.7}$$

The Maxwell program takes $I_{peak} = 1$ A.turn^{-1} and so a value for the inductance can be calculated.

The resistance is calculated from the power that it dissipates, which is given by the integral of the current density, $\underline{J}$, over the volume of the problem, thus

$$P = \frac{1}{2\sigma} \int_V \underline{J} \cdot \underline{J}^* \, dV \tag{3.8}$$

A second expression for the power is

$$P = R I_{RMS}^2 = \frac{1}{2} R I_{peak}^2 \tag{3.9}$$

Thus the resistance can be determined from

$$R = \frac{\frac{1}{\sigma} \int_V \underline{J} \cdot \underline{J}^* dV}{I_{peak}^2} \tag{3.10}$$

Coil Impedance Estimate

To compare the result of the simulations with the actual coil values, an estimate of the coil impedance was found using some of the estimates from section § 2.2. The resistance of the coil can be estimated by treating the coil as a hollow copper cylinder with a thickness of 1 mm, a height of 75 mm and a diameter of 70 mm. This gives a value of R ~ 5×10^{-5} Ω. The inductance can be estimated by treating the coil as a solenoid with an air core such that

$$L = \frac{\mu_0 N^2 A}{l} \tag{3.11}$$

where N is the number of turns in the coil, A is the coil area and l is the coil length. This yields a value of L ~ 10^{-3} H for a 100-turn coil and L ~ 10^{-7} H for a single-turn coil.

3.1.3 Eddy Current Solver

The eddy current field solver is used to simulate the influence of time-varying magnetic fields on conductors. All time-varying fields, $\underline{F}(t)$, are assumed to be sinusoidal and oscillating at the same frequency, ω, and phase, θ, with the form

$$\underline{F}(t) = F_0 \cos(\omega t + \theta) \tag{3.12}$$

where F_0 is the field amplitude. All fields must have the same frequency, but do not have to be in phase. Problems involving non-sinusoidal fields must be broken into harmonics and solved at each frequency. For the IDS coil and target system the magnetic field measurements described in section § 2.2 show that the field is of the form of equation (eq 3.12).

Maxwell's equations for the fields in the problem are

$$\nabla \cdot \underline{E} = \frac{\rho}{\varepsilon} \tag{3.13}$$

$$\nabla \times \underline{E} = -\frac{\partial \underline{B}}{\partial t} \tag{3.14}$$

$$\nabla \cdot \underline{B} = 0 \tag{3.15}$$

$$\nabla \times \underline{B} = \mu \underline{J} + \mu\varepsilon \frac{\partial \underline{E}}{\partial t} \tag{3.16}$$

where $\underline{E}$ is the electric field, $\underline{B}$ is the magnetic flux intensity, ρ is the charge density, ε is the permittivity, μ is the permeability and $\underline{J}$ is the current density. There are also a number of relations: magnetic flux intensity and magnetic field, $\underline{B} = \mu \underline{H}$; electric flux and electric field, $\underline{D} = \varepsilon \underline{E}$; and current density and electric field, $\underline{J} = \sigma \underline{E}$, where σ is the conductivity. Fields in the form of equation (3.12) can be expressed as

$$\underline{F}(t) = \mathrm{Re}[F_0 \exp(i\theta)\exp(i\omega t)] \tag{3.17}$$

and therefore

$$\frac{\partial \underline{B}}{\partial t} = i\omega \underline{B} \tag{3.18}$$

and

$$\frac{\partial \underline{E}}{\partial t} = i\omega \underline{E} \tag{3.19}$$

Thus Maxwell's equations (3.14) and (3.16) for a time harmonic field can be expressed as

$$\nabla \times \underline{E} = -i\omega \underline{B} \tag{3.20}$$

$$\nabla \times \tfrac{1}{\mu} \underline{B} = \sigma \underline{E} + i\omega\varepsilon \underline{E} \tag{3.21}$$

Let a vector potential, $\underline{A}$, be defined with the equation

$$\underline{B} = \nabla \times \underline{A} \tag{3.22}$$

Equation (3.22) may be substituted into equation (3.21) to give

$$\nabla \times \tfrac{1}{\mu} (\nabla \times \underline{A}) = \sigma \underline{E} + i\omega\varepsilon \underline{E} \tag{3.1}$$

As described by Weiss and Csendes [37] a solution for $\underline{E}$ in terms of $\underline{A}$ and φ is given by

$$\underline{E} = -i\omega \underline{A} - \nabla\varphi \tag{3.23}$$

where φ is a scalar potential function. Substituting this into (3.22) yields

$$\nabla \times \tfrac{1}{\mu} (\nabla \times \underline{A}) = (-i\omega \underline{A} - \nabla\varphi)(\sigma + i\omega\varepsilon) \tag{3.24}$$

The right-hand side of this equation is of the form of a complex current density with the three components. The electric potential results in a source current density

$$J_s = -\sigma \nabla\varphi \tag{3.25}$$

Time-varying magnetic fields result in an eddy current density

$$J_e = -i\omega\sigma \underline{A} \tag{3.26}$$

The remainder is the result of time-varying electric fields and can be described as a displacement current density

$$J_d = i\omega\varepsilon (-i\omega \underline{A} - \nabla\varphi) \tag{3.27}$$

The sum of equations (3.25), (3.26) and (3.27) is the total current density, J_T. When modelling conductors connected to an external source, the total current in the conductor, I_T, must be specified and thus J_T is specified by the integral over the cross-section of the conductor Ω

$$I_T = \int_{\Omega} \underline{J}_T \, d\Omega \tag{3.28}$$

The eddy current solver calculates eddy currents by solving for $\underline{A}$ and φ in equation (3.24) and utilising equation (3.28).

The eddy current solver cannot use these equations for non-linear materials because although the current is sinusoidal, the fields associated with non-linear materials consist of a number of

harmonics. Ansoft's Maxwell programs utilise an effective magnetic flux density and effective magnetic field intensity, which depend on the frequency of the harmonics. This is described in more detail in the Ansoft technical manual [38].

3.1.4 Solution Criteria and Meshing

The FEA solver breaks the problem space into a mesh of smaller elements over which the program can solve the differential equations. In general, the elements may be any shape, but in the Maxwell program triangles and tetrahedrons are used for two- and three-dimensional problems respectively. A number of options are available to produce a solution with the desired accuracy. The meshing process can be wholly automatic, wholly manual, or a combination of both.

The entirely automatic process generates an initial coarse mesh that is refined over a number of passes. After each pass, a value of the error in the field is calculated and the mesh is refined by a specified amount to reduce this error for the next pass. Once a user-specified target error has been reached, the solution process will stop. To put an upper limit on the maximum time that the solver will attempt to meet this target, the user may also specify the maximum number of passes that are to be completed before the process will stop regardless of the error. The result is a finer mesh around material boundaries and in the corners of objects.

The manual meshing process allows the user define smaller elements in specific areas of interest; that particular mesh is then solved on an as-is basis. The final meshing method involves a combination of both manual and automatic processes; the meshing program is given a direction with a manual initial mesh and then the automatic refinement process is applied. The solution process for finer meshes is more computationally intensive and requires more memory than coarser meshes. So the desired accuracy must take account of the available resources. For example, with the IDS and target arrangement, the area between the coil and the target is of particular interest and so the space in this region can be refined while the remainder of the problem can be left with a relatively coarse mesh. The result is that the error in the field between the coil and the target is lower than other areas that are not of particular interest.

The meshing process can be controlled by specifying mesh properties for individual objects, which can be done by either setting the maximum element size or the maximum number of elements. This can be exploited by using dummy objects that have no electrical properties, and no function in the problem, but have tighter mesh properties than the surrounding areas. For example, the region between the IDS coil and target can include a dummy object with a much finer mesh than the surrounding region and so more accurate field solutions will be found in that particular area of interest.

Within each solver pass there is also an iterative process to refine the field solution; the maximum number of iterations can be specified before the solver is started. A normalised error quantity called the solver residual is used to specify acceptable tolerances for the solution; for linear materials there is a linear residual and for non-linear materials there is a non-linear residual. A residual is calculated after each iteration: if it is higher than the specified value a correction is added and another iteration is completed, if it is lower than the specified value then no further iterations are run.

The Maxwell program can produce solutions through one of two methods. The first is a direct method that will always converge to a solution and the second is a more intelligent method that is generally faster for problems with large meshes, but does not always converge. The decision as to which method is used can be left to the program by selecting the automatic mode that makes an estimate of whether the faster method will work. If the estimate is incorrect and the faster method does not appear to be converging, then the process is stopped and the direct method is used.

3.2 Two-Dimensional FEA

Ansoft's Maxwell 2D Field Simulator uses FEA to numerically solve two-dimensional electromagnetic problems. A problem is entered into the program and field solutions are calculated as described above. Two-dimensional simulations are appropriate to schemes such as the IDS coil with a target centrally positioned below it.

3.2.1 Test Problem

A basic model of the IDS sensor coil and target arrangement was used to investigate the effectiveness of the two-dimensional FEA.

Geometry

One of two coordinate systems may be utilised for drawing the geometry of a two-dimensional problem. The first is an xy-plane Cartesian coordinate system, which is appropriate for any cross-sectional geometry. In this system, the current flows in the z-direction and therefore the magnetic field lies entirely in the xy-plane with no z-component. The second is an rz-plane cylindrical coordinate system, which is suitable for axial-symmetric problems. In this system, current flows in the θ-direction around the device's axis of rotational symmetry and therefore the flux only has components in the rz-plane. The problem geometry of the IDS sensor coil with a centred target can utilise the latter scheme, as shown in figure 3.2. It should be noted that using this coordinate scheme means that the target is modelled as disc rather than a rectangle.

The assumptions about the geometry of the coil were taken from a discussion with the UK supplier of the IDS and from the Kaman user manual [10]. The coil is taken as being a 1 mm thick cylinder with an external diameter 1 mm less than the outer carbon fibre protective casing. The target was taken as being a 5 mm thick rectangular plate positioned at $d_t = 10$ mm, with a width 3 times the coil diameter to avoid problems associated with small targets (§ 1.4.2).

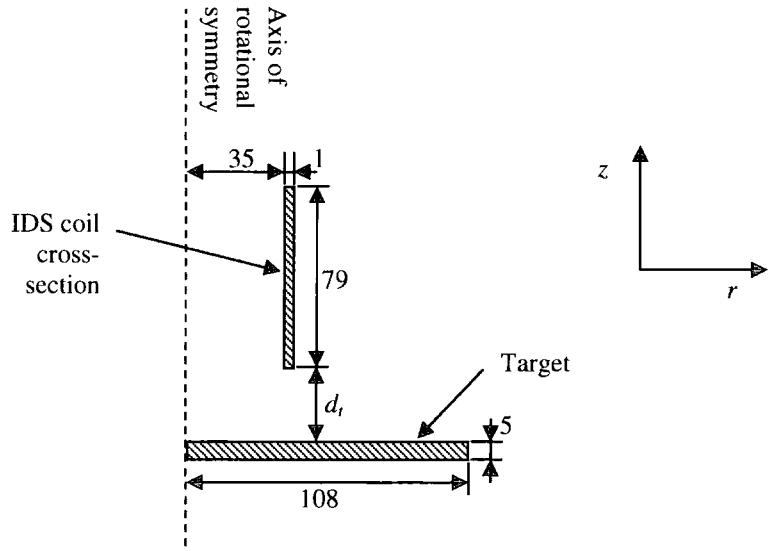

Figure 3.2. The axial-symmetric geometry of the IDS sensor coil and centred target. Dimensions given in mm.

Materials

The IDS coil was assumed to be a copper construction and therefore appropriate material parameters were selected: $\varepsilon_r = 1.0000000$, $\mu_r = 0.9999910$, $\sigma = 5.8000000 \times 10^{-7}$ S.m^{-1}. For the purposes of the simulation the target was taken to be aluminium with $\varepsilon_r = 1.000000$, $\mu_r = 1.0000210$, $\sigma = 3.800000 \times 10^{-7}$ S.m^{-1}. The remainder of the problem space was set to be a vacuum ($\varepsilon_r = 1.0000000$, $\mu_r = 1.0000000$, $\sigma = 0.0000000$ S.m^{-1}), which is a good approximation to air ($\varepsilon_r = 1.0006000$, $\mu_r = 1.0000004$, $\sigma = 0.0000000$ S.m^{-1}) and was expected to result in a faster solution.

Boundaries

The IDS coil consisted of wound copper wire and so eddy currents could not develop in it, therefore in the simulation it was set to be "stranded". The aluminium target, however, did experience eddy currents on the surface as a result of the excitation from the coil, therefore the default Neumann eddy current boundary was applied. Using the estimate of the coil current in section § 2.2, the current density in the coil was estimated to have a magnitude, $J_0 = 10^4$ A.m^{-2}

over the whole cross-section. The outer balloon boundary that contains the whole problem was set to pad all the problem geometry by 200 %.

Solution

The impedance matrix was set to involve the coil and the target material. The solution criteria were set so that the solver used the automatic mesh process with 15 % refinement per pass to solve for both the field and the impedance matrix with a residual of 10^{-5}. The solver was then set to find a solution with a maximum error of 1 %, which took approximately 30 seconds on the computer specified in section § 3.1.

Results

The impedance matrix yielded a coil resistance of $1.617 \times 10^{-4}\,\Omega$ and an inductance of 4.051×10^{-8} H. The inductance value is the result for a single-turn coil and so there is agreement to within an order of magnitude with the estimate of coil impedance found in section § 3.1.2.

A plot of the magnetic field calculated by the simulation is shown in figure 3.3. This shows that the FEA has produced field results that instinctively make sense in terms of a simple representation of the problem i.e. the field is strongest around the coil and decays with increasing distance from it and the field is compressed by the target and the eddy currents generated in it. The edge of the target affects the field such that it appears to bulge at this point, which is discussed in section § 3.4.2.

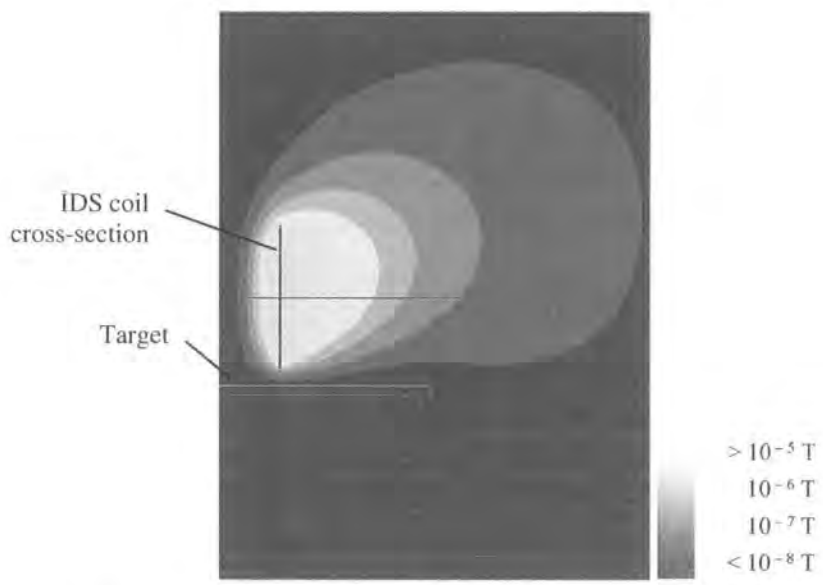

Figure 3.3. The magnetic flux plotted for the two-dimensional test problem. The central lighter portions represent a stronger field than the surrounding darker regions.

A plot of the magnitude of the z-component of the field taken along a line parallel to the target, but 1 mm below the base of the IDS coil, is given in figure 3.4. On this plot radius $R = 0$ mm is the left-hand edge of the problem space, which is the centre of symmetry and lies below the centre of the IDS coil. It is the magnitude of the z-component that is of interest, since this is the quantity that is measured by the test coil system described in section § 2.5.2. The plot reveals local discontinuities which result from areas of the mesh that were not well refined. Recall that the external radius of the simulated IDS coil was 36 mm and this corresponds to the point on the figure where the plot drops to zero. This zero figure means that the field no longer has a z-component and — recalling that the field cannot have a θ-component — must therefore only have an R-component. Investigation of the phase revealed that the field flips direction at this point, which instinctively makes sense in terms of a simple representation of what is happening to the field from the coil: at a given point in the coil's current cycle the field lines extend downwards from the centre of the coil (strong vertical component); below the edge of the coil the field lines are horizontal (weak vertical component); and outside the edge of the coil the field lines loop upwards to the top of the coil (strong vertical component).

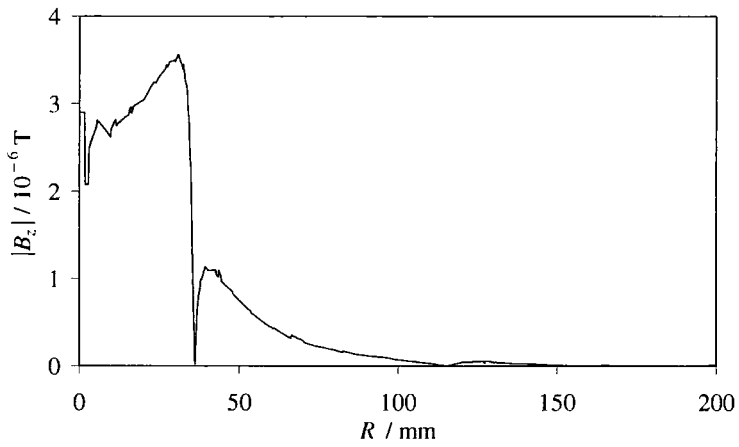

Figure 3.4. Variation in the magnitude of the z-component of the field, $|B_z|$ / tesla, with radius, R / mm, along a line 1 mm below the IDS coil.

The form of figure 3.4 is in agreement with the field measurements shown in figure 2.6 and the magnitude of the field below the central portion of the IDS coil also agrees approximately with the measured value of ~ 5×10^{-6} T.

3.2.2 Simulation Refinement

The test problem simulation produced good results that appeared to reliably represent the form of the experimentally measured field. The error for the test problem was set at 1 % but the

discontinuities found in figure 3.4 demonstrated that this value did not correspond to the actual error in the field solution. The meshing process required more refinement to produce a more accurate field solution and smoother plots that could reveal more detailed information. Therefore a dummy object (§ 3.1.4) was introduced to decrease the mesh size in the region of interest i.e. the space between the coil and the target.

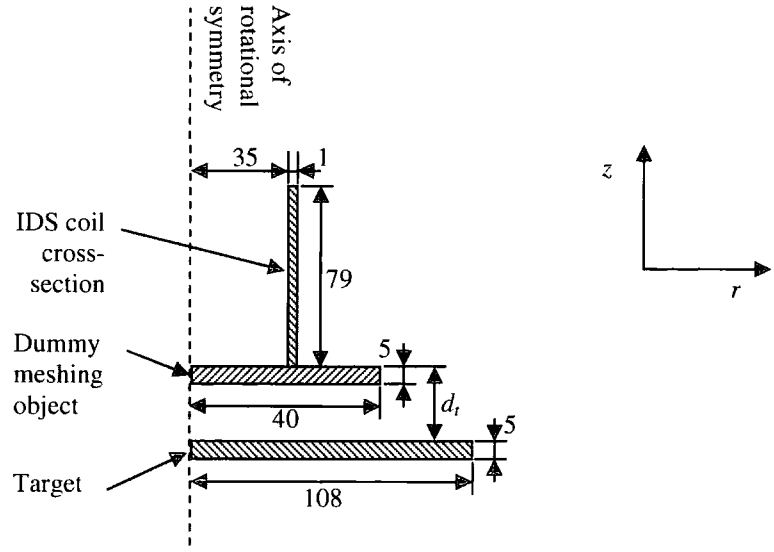

Figure 3.5. Axial-symmetric geometry of the IDS sensor coil and centred target with the inclusion of a dummy object to improve meshing. Dimensions given in mm.

Figure 3.5 shows the addition of the dummy object to the test problem geometry. The object is simply a vacuum region within which the mesh is set to have a low initial element size. The maximum element area in the dummy object was set to 0.5 mm^2. Figure 3.6 compares the mesh without (3.6(a)) and with (3.6(b)) the dummy object. It can clearly be seen that there are more elements in the area of interest in the mesh with the dummy object.

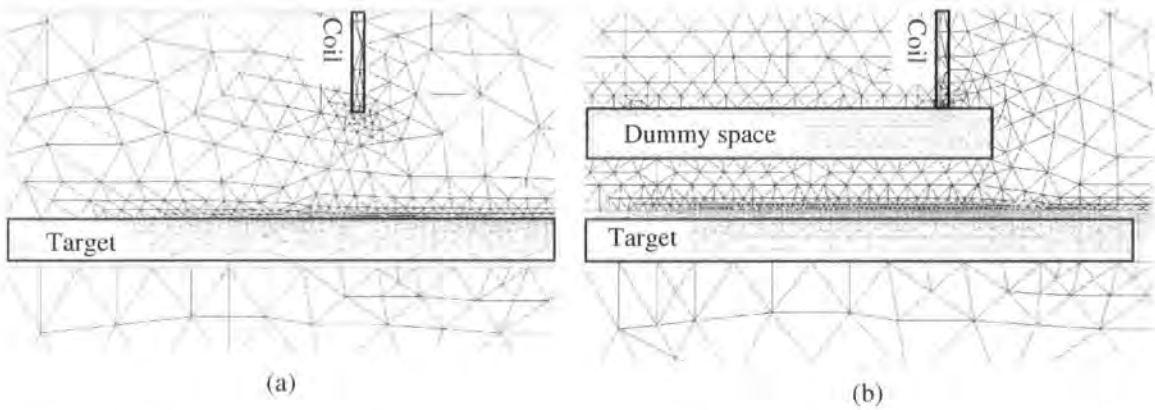

Figure 3.6. Mesh in the space between the coil and target. (a) The original problem without a dummy object. (b) The problem with a refined mesh inside the dummy object.

The field solution took about the same time as the original problem (~ 30 s) and the results are demonstrated by the plot in figure 3.7. Comparing this graph with figure 3.4 shows that the addition of the dummy object has successfully improved the continuity of the solution in the region between the IDS coil and the target, without a noticeable increase in the solver time.

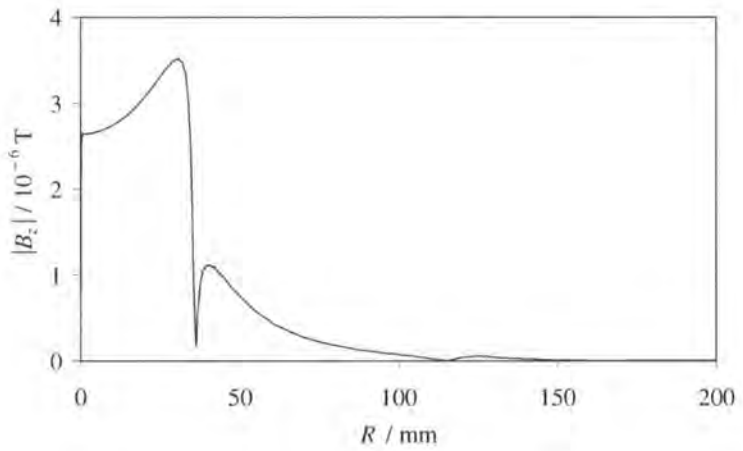

Figure 3.7. Magnitude of the z-component of the field, $|B_z|$ / tesla, with radius, R / mm, along a line 1 mm below the IDS coil, for a geometry with a meshing dummy object.

3.2.3 Parametric Test Problem

Using the basic model of the test coil and target, a parametric problem was constructed to demonstrate the influence of different target displacements on the field. This was achieved by setting a constraint, d_t, from the base of the coil to the top of the target that was swept in five

steps over the range $d_t = 0, 5, \ldots, 25$ mm. The whole solution took approximately 2.5 min, which is what would be expected given that one solution took 30 s.

The impedance matrix was calculated for each step and the variation of inductance with d_t is given in figure 3.8. As d_t increases, the mutual inductance, M, between the coil and target decreases as the coupling between the two systems decreases. Equation (1.8) shows that a decrease in M corresponds to a decrease in the coil's equivalent resistance. Conversely, equation (1.9) shows that the decrease in M leads to an increase in coil's equivalent inductance. This theoretical analysis is mirrored by the simulation results. A further simulation, with d_t = 50 mm, showed that the curve tended to 4.36× 10^{-8} H as the target's influence decreased.

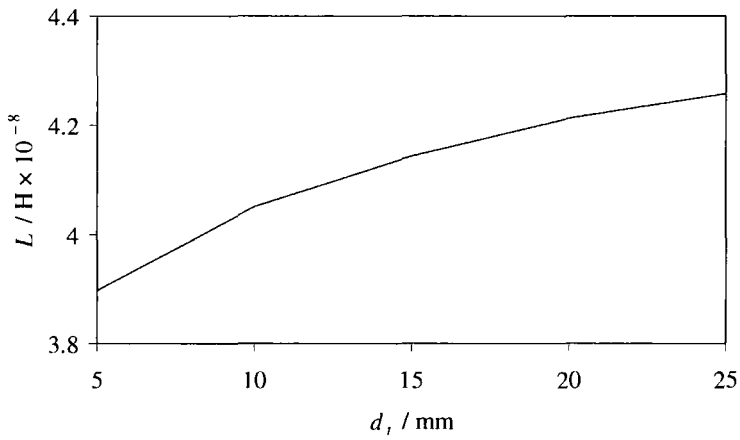

Figure 3.8. The variation of coil inductance, L, with target displacement, d_t.

3.3 Three-Dimensional FEA

Ansoft's Maxwell 3D Field Simulator uses FEA to numerically solve three-dimensional electromagnetic problems. Like its two-dimensional cousin, a problem is entered into the program and field solutions are calculated as described in section § 3.1. Three-dimensional simulations are appropriate to schemes such as the IDS coil with a target not aligned centrally so that there is no axial symmetry.

3.3.1 Test Problem

A simple model of an IDS coil with an offset target was constructed to test the effectiveness of the three-dimensional FEA. The two-dimensional xy-plane model of the cross-section of the problem geometry is not appropriate since it would assume that the target extended infinitely in the z-direction and could not simulate the cylindrical coil.

Geometry

As in section § 3.2.1, assumptions about the coil dimensions were taken from a discussion with the IDS supplier and from the Kaman user manual [10]. The problem geometry is shown in figure 3.9. The 5 mm thick aluminium target was positioned at d_t = 10 mm, had a width 3 times the IDS coil diameter and was offset from the central position by 0.5 times the coil diameter. An additional plane was included in the cross-section of the coil to act as a current source. The outer boundary of the problem space was set to pad all objects by 200 %.

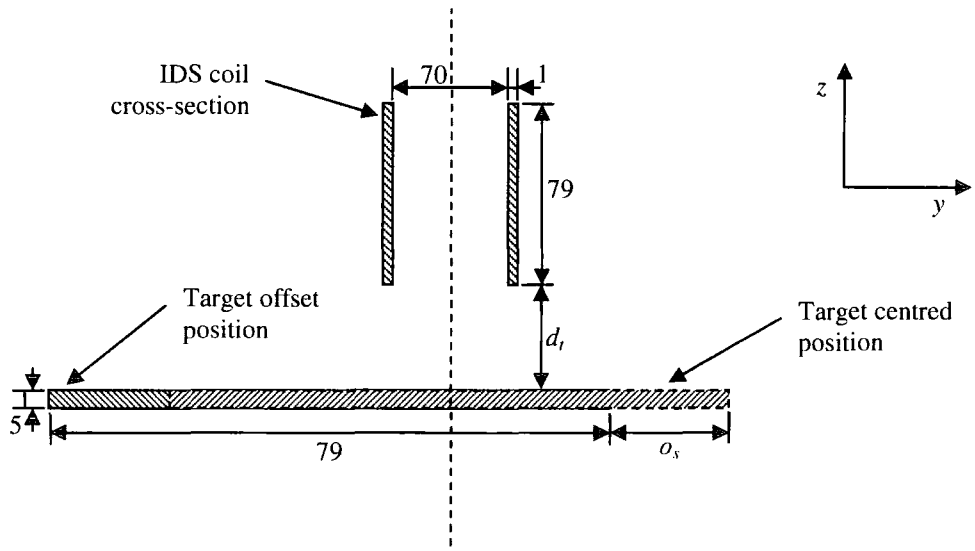

Figure 3.9. Three-dimensional geometry of the IDS coil and non-centred target *yz*-plane cross-section. Dimensions given in mm.

Materials

The appropriate materials were selected from the materials catalogue: copper coil (ε_r = 1.0000000, μ_r = 0.9999910, $\sigma = 5.8000000 \times 10^{-7}$ S.m^{-1}); aluminium target (ε_r = 1.000000, μ_r = 1.0000210, $\sigma = 3.800000 \times 10^{-7}$ S.m^{-1}); and vacuum for the remainder of the problem space (ε_r = 1.0000000, μ_r = 1.0000000, σ = 0.0000000 S.m^{-1}).

Boundaries

The IDS coil was set to be stranded to prevent eddy currents from forming in it and the current density estimate from section 2.2 was used to set the total coil current to 0.8 A. This was the only source in the problem and so the phase was set to zero. The eddy current effect was turned on in the target and off in the coil.

Solution

The impedance matrix for the three-dimensional solver works in a different way to its two-dimensional cousin and only objects with external sources can be included in the impedance

matrix; therefore the target was not included, but the coil was. The solution criteria were set so that the solver used the automatic meshing process with the program's default values of 30 % refinement per pass with a residual of 10^{-8}. The solver was then set to find a solution with a maximum error of 1 %, which took approximately 3 min on the computer specified in section § 3.1.

Results

The impedance of the coil as given by the simulation was found to consist of a resistance of $5.361\times 10^{-5}\ \Omega$ and an inductance of 4.254×10^{-8} H. The inductance value is for a single turn coil and so these values are in agreement with the estimates found in section § 3.1.2.

Figure 3.10 shows a plot of the direction of the magnetic field calculated by the simulation. The vectors show a snap-shot of the field at the start of the current cycle in the coil, which corresponds to a peak in the field magnitude. On the left-hand side of the coil, the field behaves in a similar manner to that in figure 3.3 where the field lines appear to be 'compressed' by the target. To the right-hand side of the target the field behaves differently and there is interaction with the target where the field appears to curl up at the edge of the target.

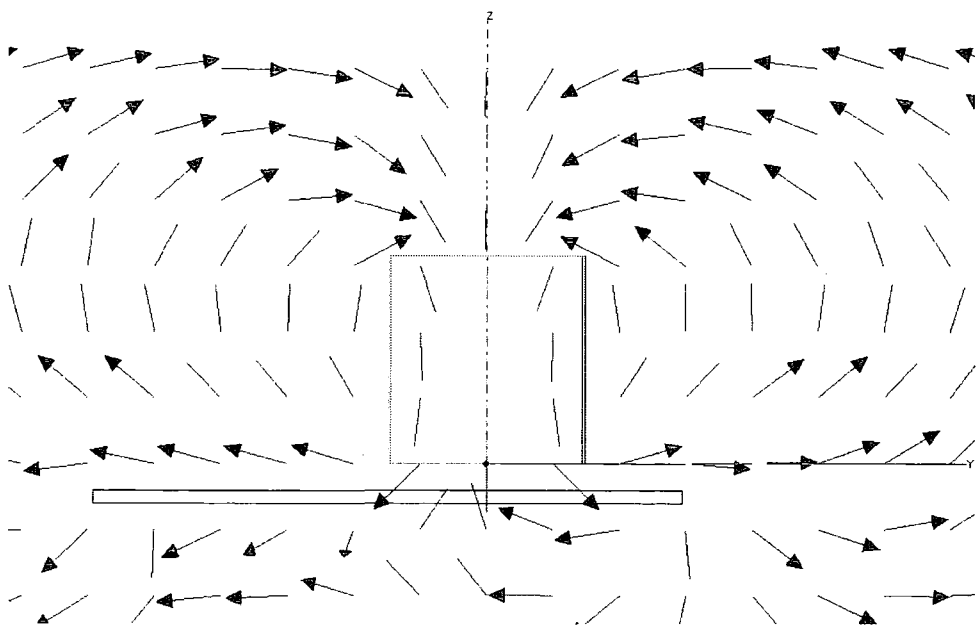

Figure 3.10. Magnetic flux direction plotted in the *yz*-plane of the three-dimensional test problem.

A plot of the magnitude of the *z*-component of the field taken along a line parallel to the target, but 1 mm below the base of the IDS coil, is given in figure 3.11. On this plot, the y = 0 mm position corresponds to the point below the centre of the IDS coil. This graph has

some of the same characteristics displayed in the two-dimensional simulation results (figure 3.4): below the edge of the coil $|B_z|$ drops towards zero and outer 'wings' tail off with increasing distance from the centre. The discontinuities in the plot reveal areas of the mesh that are coarse and have not produced a smooth field.

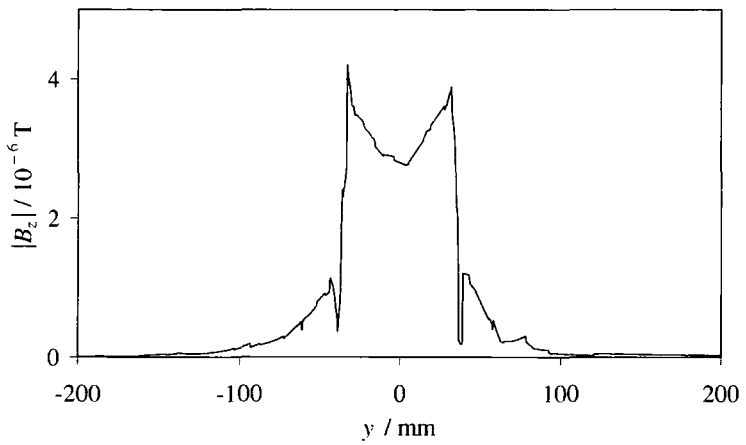

Figure 3.11. Variation in the magnitude of the z-component of the field, $|B_z|$ / tesla, with position y / mm, along a line 1 mm below the IDS coil.

The form of figure 3.11 is generally in agreement with the field measurements shown in figure 2.6, although the central portion below the IDS coil is quite different. This region consists of two spikes below the edges of the coil and a central dip, which was not observed experimentally. However, the magnitude of the field roughly agrees with the measured value of ~ 5×10^{-6} T; although the simulation value is slightly lower than the experimental reading.

3.3.2 Simulation refinement

The three-dimensional FEA produced a reliable simulation of the offset IDS coil and target system. However, the rough nature of figure 3.11 showed that the mesh needed to be refined in the region between the coil and the target. This is the same effect that was observed with the two-dimensional simulation where the error for the test problem was also set at 1 %, so it was thought unlikely that setting this to a tighter tolerance would yield more accurate results. Therefore a dummy object (§ 3.1.4) was introduced to decrease the mesh size in the region of interest i.e. the space between the coil and the target. The object was set to be a vacuum to match the surrounding area, but with a tighter mesh to improve the field solutions. The line from which the field profile measurements were taken lies 1 mm below the base of the IDS coil and the dummy meshing space was constructed to include the line with a padding of 2 mm. The maximum element size in this region was set to 0.5 mm.

The field solution took approximately 90 min to produce a solution to the desired accuracy i.e. 30 times longer than the problem without the additional meshing space. The field profile is shown in figure 3.12 and comparing it to figure 3.11 demonstrates that the addition of the dummy meshing object improved the field simulation continuity albeit with a substantial increase in solution time.

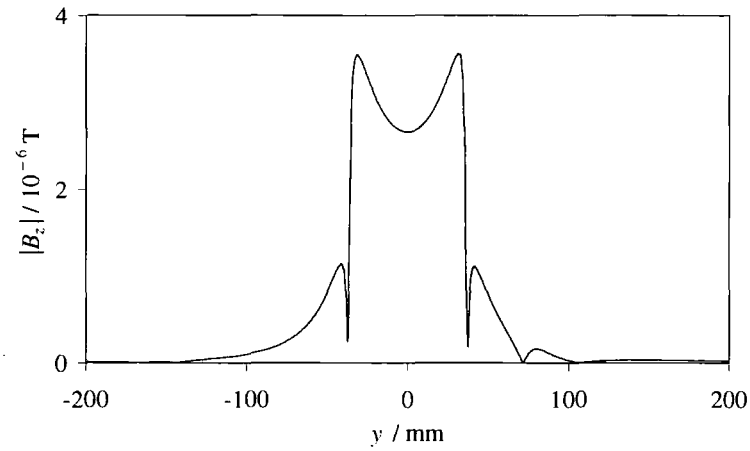

Figure 3.12. Variation in the magnitude of the z-component of the field, $|B_z|$ / tesla, with position y / mm, along a line 1 mm below the IDS coil, for a geometry with a meshing dummy object.

3.3.3 Parametric Problems

The three-dimensional field simulator did not include the parametric unit that the two-dimensional version did. However, it was possible to use a combination of operating system batch files and program macros. For example a batch file could include instructions to start the Maxwell program and execute a macro to construct the problem geometry, set up the materials and boundaries and solve the problem. Once the program had finished, the next line in the batch file was executed and a macro containing a different problem geometry could be executed.

General Macro

A general macro was developed for use in the later experiments. The macro took the target distance, d_t, target width, w_t, and target offset, o_s, in millimetres from the project file name, as shown in table 3.1. The format of the geometric parameters was strict, although the final date tag could be any length to include information about the project date, author, etc. Other dimensions for the problem geometry were assumed to be constant and were set within the macro. Using this method the batch file could run a set of problem geometries with differing problem geometries.

Table 3.1. Parameters taken by macro from project file name, where d_t = target distance, w_t = target width, o_s = target offset.

	d_t		w_t		o_s		Date or Other Notes
General format	AAAA	_	BBBB	_	CCCC	_	DD-MM-YY
Example	0010	_	0222	_	0037	_	01-01-00

For problems that required dummy meshing objects, a macro was constructed to set the maximum element size in the problem objects. However, a bug in the Maxwell program meant that it was not able to utilise macros automatically for the meshing process and a work-around method had to be used. A batch file called the general macro to construct and set up each problem. Each problem was then opened individually and the meshing macro manually started. A second batch file was then used to solve the problems automatically in succession.

Test Problem

A parametric test problem was constructed to test the macros and investigate the influence of target displacement on the impedance of the coil. The general macro and the meshing work-around described above were used. The test problem geometry from section § 3.3.1 was used with $w_t = 222$ mm and $o_s = 37$ mm, but the target distance was swept in the range $d_t = 0, 5, \ldots, 25$ mm. The mesh was refined such that maximum length of elements in the target and the measuring gap was 7.5 mm. The whole solution took 450 min, which was approximately 5 times the length of an individual problem, as expected.

The results of the simulation are plotted in figure 3.13 and show the effect described in equation (1.7) whereby the coil inductance decreases with increasing d_t. A further simulation, with $d_t = 50$ mm, revealed that the inductance tended to 4.58×10^{-8} H as the influence of the target decreased. This value differed slightly from the two-dimensional result ($L \rightarrow 4.36\times 10^{-8}$ H), although because the target had very little influence at large displacements, one would expect them to be identical. This implies that the differences are due to simulation errors, which cannot be quantified directly since they depend on the particular mesh used for the solution. None-the-less the difference is less than 5 % and the form of the two- and three-dimensional result plots are as predicted by the equivalent circuit model.

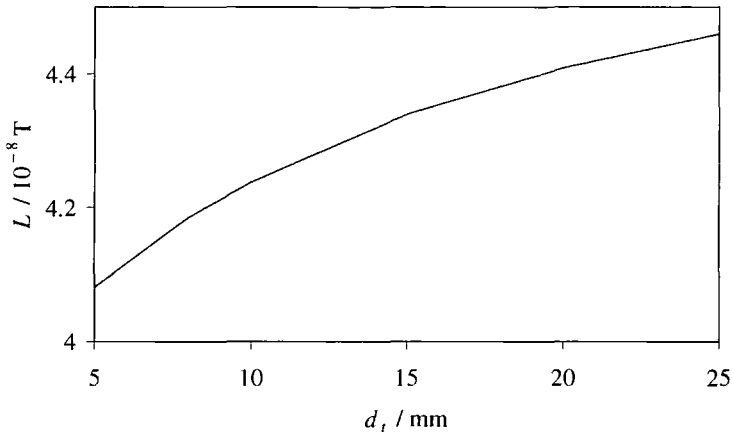

Figure 3.13. The variation of coil inductance, L, with target displacement, d_t for an offset target geometry.

3.4 General Considerations

The FEA simulations of the coil and target system have produced results that compare well with the experimental observations.

3.4.1 FEA of Experimental Equipment

The simulations discussed above involve idealised models of the coil and target arrangement; they do not include experimental considerations such as test coils used to measure the field or spacers used to separate the target and IDS coil.

Test coils

Measurements taken from a system will always affect that system to some extent. In the case of using test coils to measure the magnetic field, the effect was expected to be negligible since the coils were stranded and so eddy currents could not form in them. This assumption was confirmed by completing a two-dimensional simulation of a similar geometry to that of section § 3.2.1, but with the incorporation of a test coil. The test coil was modelled as a 5 mm high, 10 mm diameter, empty copper cylinder with an inside diameter of 8 mm, positioned below the centre of the IDS coil. A plot of the magnetic flux given in figure 3.14(a) revealed no noticeable change to the field pattern compared to figure 3.3. The magnitude of the z-component of the magnetic field taken along a line located 1 mm below the IDS coil is given in figure 3.14(b) and comparison with figure 3.4 also revealed no significant effect from the addition of the test coil. These results were taken as justification for neglecting test coils in the later simulations.

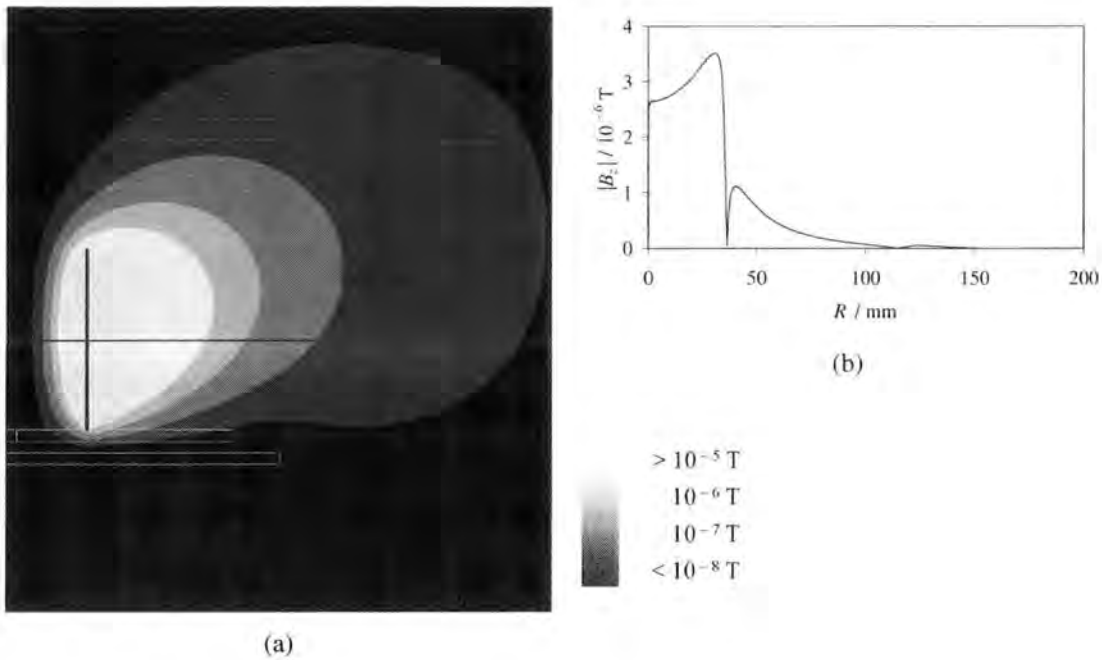

Figure 3.14. Two-dimensional simulation of the IDS coil and target arrangement with a field-measuring test coil. (a) Magnetic flux plot with stronger field represented by lighter colour. (b) Magnitude of the *z*-component of the field, $|B_z|$ / tesla, with position *R* / mm, along a line 1 mm below the IDS coil.

Plastic Spacers

In the simulations above, the space between the test coil and the target has been taken as a vacuum. For the field strengths involved in this system, the electrical properties of air were negligible and so the problem background was modelled as a vacuum. However, for practical purposes the IDS coil was held above the target using a set of plastic spacers of various heights to provide an accurate separation. It was thought that the non-conducting spacers would not affect the field since the eddy currents would not form in them. This assumption was confirmed by completing a two-dimensional simulation based on that described in section § 3.2.1, but with the incorporation of a plastic spacer. The spacers were machined from clear acrylic block and the materials catalogue gives the electrical properties of such a material as $\varepsilon_r = 3.5000000$, $\mu_r = 1.0000000$, $\sigma = 0.0000000$ S.m^{-1}. The width of the block was taken as being that of the sensor coil and the axial-symmetric coordinate system meant that it was modelled as a filled cylinder positioned directly below the IDS coil.

A plot of the magnetic flux given in figure 3.15(a) revealed no noticeable change to the field pattern compared to figure 3.3. The magnitude of the *z*-component of the magnetic field taken along a line positioned 1 mm below the IDS coil is given in figure 3.15 (b) and comparison with

figure 3.4 also revealed no significant effect from the addition of the plastic spacers. These results were taken justification for neglecting plastic spacers in the later simulations.

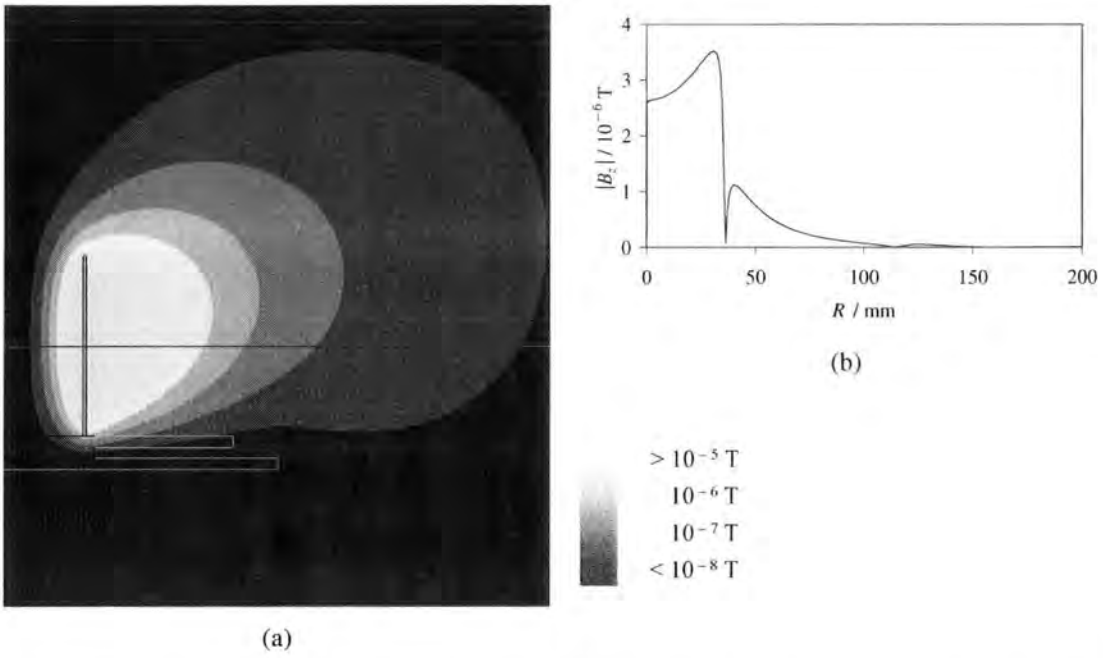

Figure 3.15. Two-dimensional simulation of the IDS coil and target arrangement with a plastic target spacer. (a) Magnetic flux plot with stronger field represented by lighter colour. (b) Magnitude of the z-component of the field, $|B_z|$ / tesla, with position R / mm, along a line 1 mm below the IDS coil.

3.4.2 Edge Effects

The edge effect was noticeable through the initial FEA models, for example in figure 3.3 where there is a fold in the flux above the edge of the target. This is caused by the eddy currents, which channel the field around the target object. This process is further demonstrated by the plot of the z-component of the magnetic field shown in figure 3.16.

Figure 3.16. Demonstration of the edge effect on the *z*-component of the magnetic field around the target.

3.4.3 Extraction of Data

The output from the magnetic field sensing test coils and the phase-locking program described in section § 2.6.2 was a single voltage for the entire area of the coil. This signal was the result of an averaging effect of the flux passing through the coil. The necessity to compare experimental and simulation results lead to the requirement for a similar averaging effect to be applied to the simulated field measurements.

The relationship between the incident field and the output from the test coil is a convolution of the field pattern as a function of position and the response of the test coil as a function of position. The convolution operation describes the overlap of two functions, which in this case is between the magnetic field, $f(x, y, z)$, and the test coil's response $g(x, y, z)$. The convolution of these two functions at a point, $p(X, Y, Z)$, is given by the integral

$$f \otimes g = \int_{-\infty}^{+\infty} f(x, y, z) g(x - X, y - Y, z - Z) \, \mathrm{dx\ dy\ dz} \tag{3.29}$$

This describes the three-dimensional case; in two-dimensions the arrangement is the same but over the coordinates R and θ (or y and z). In the Maxwell programs, field values were extracted in a convenient format by taking them from a line by the technique used above (e.g. figure 3.4). To assist in the process, macros were used to draw the lines at the desired positions and then

save the field values to disk. A Java application was constructed to read the data and convolve them with the coil response function.

For the case of a two-dimensional field solution, lines were constructed to run parallel to the y-axis (horizontal) over a 5 mm range of 1 mm spaced z-values (vertical). Field values were taken from the six lines and saved to a series of files with names that described the line positions. To test the convolution program the coil response was taken as being constant over the length and width of the coil and coil-field coupling was assumed to be 100 %. The result is that the coil response function was taken as a step function with fields inside the coil coupling to the coil and fields outside not coupling to the coil.

In the three-dimensional case, lines were drawn parallel to the y-axis, over a 5 mm range of 1 mm spaced z-values and a 10 mm range of 1 mm spaced x-values. Problem geometries created by the macro described in section § 3.3.3 produced fields that were symmetrical about the y-axis. This consideration meant that for test coils positioned on the y-axis, lines only needed to be drawn on one side of the axis, thereby halving the number of lines to be drawn. Field values were taken from the 36 lines and again saved to a series of files with suitable names. As for the two-dimensional convolution, a test was done using a step function to describe the coupling between the coil and the field.

An example of the three-dimensional convolution is given in figure 3.17, which is the result of applying the program to the field profile from a small-target simulation. The fluctuations in the lobes are caused by the edge effect of the target. It can be seen that although the general pattern in of the filed is unchanged it is smoothed over the area of the test coil. The raw profile is from a line directly below the centre of the IDS coil, whereas the processed profile takes contributions from the whole test coil volume. This is responsible for the lower field value in the central portion of the processed data.

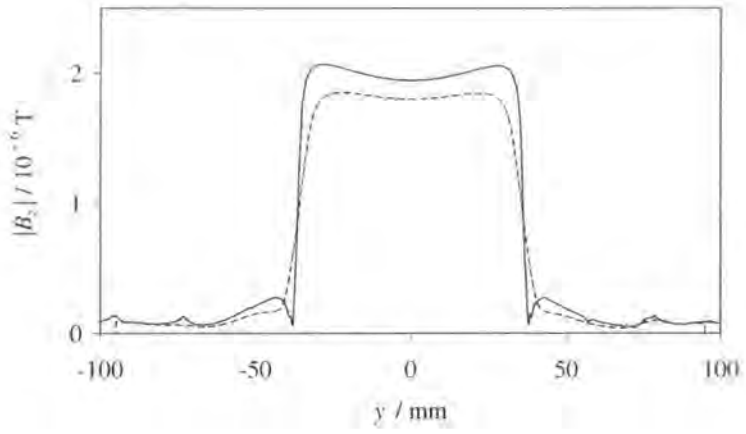

Figure 3.17. Application of the three-dimensional convolution program to the field profile of small-target arrangement. (Solid ——) raw field. (Dash - - -) Processed field.

3.5 Summary

In this chapter some of the theory and workings of eddy current FEA have been investigated and both two- and three-dimensional FEA simulations of an IDS coil and target arrangement have been developed and refined. The two-dimensional simulations were appropriate for problems with a large centred target. The three-dimensional simulations were found to take longer to solve (up to 180 times longer for a solution with a well refined mesh), although they could be applied to any target and coil arrangement. The models neglected the test coils and the plastic spacers from the simulations; test simulations were used to justify these assumptions. It was not possible to quantify the errors on the values produced by the simulations because the accuracy of the solution depended on the solver and the nuances of the individual meshes.

Test simulations with $d_t = 10$ mm and w_t of three times the IDS coil diameter were completed. A 2D model was solved with a centred target and a 3D model was solved with $o_s = 0.5$ times the IDS coil diameter. The simulations with a refined mesh gave central field values of 2.6×10^{-6} T and 2.7×10^{-6} T for the 2D and 3D simulations respectively, which were similar in value to the experimentally estimated field strength of $\sim 5 \times 10^{-6}$ T. The coil impedances were also solved and inductances were found to be 4.051×10^{-8} H and 4.254×10^{-8} H for the 2D and 3D cases respectively, which were in agreement with the experimentally estimated values of $\sim 10^{-7}$ H. The difference was again due the target offset of the 3D model, which decreased the coupling and therefore increased the inductance in agreement with the equivalent circuit models.

Techniques for solving two- and three-dimensional parametric problems have been developed and were used to demonstrate the influence of target distance on the impedance of the IDS coil.

The results matched the equivalent circuit models and as d_t increased (the influence of the target decreased) $L \rightarrow 4.36\times 10^{-8}$ H and $L \rightarrow 4.58\times 10^{-8}$ H for the 2D and 3D models respectively. Since at large d_t the target had little influence on the coil, the differences between the 2D and 3D models must have resulted from differences in the meshes and solvers. A convolution program has also been developed to match the output from the field simulations and the signal measured by the test coils. The results have been compared to experimental results and good correlation was found.

Chapter 4

Inductive Displacement Sensor Limitations

The first chapter's introduction to IDSs and their limitations provides the groundwork for this present discussion, which concerns results from a complete investigation of these limitations. This was achieved using the experimental techniques discussed in chapter two and the FEA electromagnetic field simulations from chapter three. Firstly, the influence of target material on the IDS is discussed in section § 4.1 where experiments using aluminium, brass, copper, nickel and steel are described. The following section (§ 4.2) discusses how displacing the target laterally relative to the IDS coil affects the reliability of the system. This is closely related to the final section's investigation of the effect of using targets that are smaller than the recommended 2.5 – 3 times the IDS coil diameter.

4.1 Target Material

IDSs are usually calibrated in the factory for use with a particular target material and attempting to measure displacements to different target materials will result in errors. The influence of target material on the impedance of an IDS coil is described in section § 1.4.1 and equation (1.13) shows that coil impedance is not only dependent on target displacement and current frequency, but also on the conductivity and permeability of the target. To investigate this, the effect of using different materials on the reliability of IDSs was characterised (§ 4.1.1) and the results were used to show that the effect was real. Earlier equivalent circuit models of the system were confirmed by modelling the system with FEA electromagnetic simulations (§ 4.1.2).

4.1.1 Characterising the Effect of Target Material

An experiment was conducted to characterise the effect of using the IDS to measure the distance to different target materials. The IDS used for the experiment was calibrated for use with an aluminium target and it was expected that using it on other target materials would result in errors in the displacement measured.

Table 4.1. Physical properties of some targets investigated.

Sample Material	Width × Height / mm ± 0.5 mm	Thickness / mm ± 0.05 mm	μ_r	$\sigma^{\ddagger}$ (at 273 K) / 10^7 S.m^{-1}	Standard Depth of Penetration (at 1 MHz) / 10^{-5} m
Aluminium	250 × 253	1.50	1.000021	4.00	7.96
Brass	309 × 226	1.30	1	1.59	12.6
Copper	224 × 222	3.30	0.999991	6.45	6.27
Mild Steel	214 × 187	1.00	1000[†]	0.588	0.656

[†] Permeability is a function of field $\mu = B / H$, take 1000 for this estimate.
[‡] From Kaye and Laby [39]

Table 4.1 gives the dimensions of the different target samples used in the experiment. The targets must be of sufficient width to allow eddy currents to flow in the surface as described in section § 1.4.2. The IDS user manual [10] (p. 15) gives the sensor diameter as 73.7 mm and since it is unshielded, the target material must be 2.5 – 3 times larger than the sensor. The skin depth, or standard depth of penetration, was defined in section § 1.2.2 as the point where the current density has decreased to $1/e$ times its value at the target surface. Table 4.1 gives the permeability and conductivity, which are used to calculate the skin depth at 1 MHz using the relation

$$\delta = (\pi f \mu \sigma)^{-1/2} \tag{4.1}$$

The distance between the target and the sensor, d_t, was varied in 5 mm steps within the range 0 – 65 mm. By cycling up and down three readings were recorded and the mean was plotted. The output voltage was found to vary linearly up to the limit of the sensor range (~ 60 mm). When the target was at a displacement greater than 60 mm the output voltage remained constant.

Figure 4.1(a) shows the displacement to the different target materials as recorded by the IDS. The axis of abscissas shows the actual target displacement i.e. the physical distance between the target and IDS barrel. The axis of ordinates shows the target displacement given by the output voltage of the IDS system. Aluminium was used as the baseline — since the IDS was factory-calibrated with plate aluminium — hence this plot is linear and the actual target displacement correspond exactly to the IDS predicted target displacement. From the figure it is apparent that the mild steel sample gave the most error. The brass and copper sample measurements were in good agreement with the aluminium.

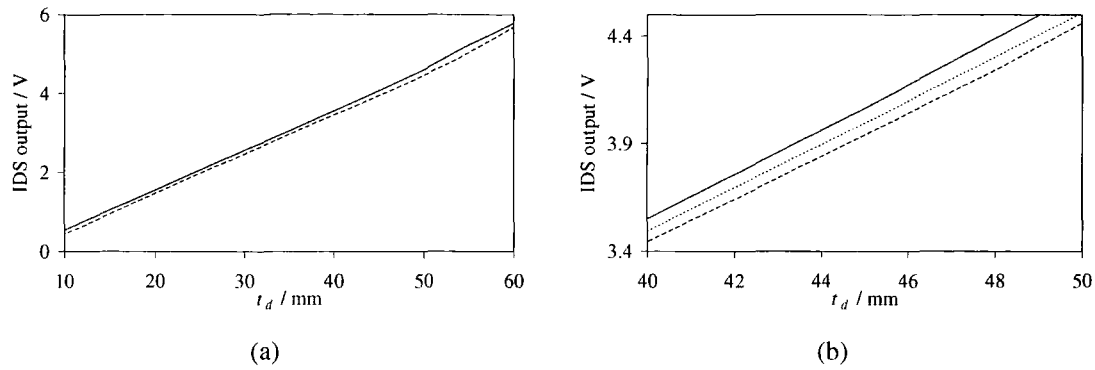

Figure 4.1. Influence of target material on IDS displacement measurements. (Solid ——) Steel. (Dash - - -) Brass. (Dot ·····) Aluminium. (a) Over the whole measurement range. (b) Close-up to highlight differences.

To highlight the differences between target materials a close-up view for mild steel and aluminium is given in figure 4.1(b). Here d_t was varied in 2 mm steps within the range 40 – 50 mm and again, the mean of three readings was found. The two lines have similar gradients but the steel line is slightly set upwards from the aluminium target. Using linear regression, expressions describing these straight lines are found to be

$$\text{Steel: } V = 0.087 d_t - 0.049 \tag{4.2}$$

$$\text{Aluminium: } V = 0.091 d_t - 0.184 \tag{4.3}$$

each with an R^2 value of 0.997. Consider a distance of 10 mm to an aluminium target; this would produce an output voltage of 0.726 V. Swapping the target to steel, the same voltage would correspond to $d_t = 9.91$ mm, which highlights the problems associated with the influence of target material.

4.1.2 FEA Simulations of the Influence of Target Material

Using the Ansoft Maxwell 2D program the influence of target material on the magnetic field was investigated. The two-dimensional module was appropriate because the large centred target meant that there was axial symmetry. Simulations were completed for each target material at a range of target distances. The distance between the base of the IDS coil and the top of the target material was set as a variable that was controlled by the parametric module. The target materials selected were aluminium, brass, copper and steel as used in the laboratory experiments. The steel used in the simulations was steel-1008 (plain steel with 0.008 % carbon) which was chosen because it has similar properties to the sample used in the experiments. A fifth material, nickel, was also simulated since it does not have a B-H curve (the relative permeability is

constant at 600) and it has a conductivity of 1.45×10^7 S.m^{-1}, thus it was quite different to the other samples and a worthwhile simulation. A suitable nickel target could not be found for the experimental testing, but it was listed in the Maxwell 2D material catalogue, which demonstrated the usefulness of the FEA simulations.

In this model there are two primary position coordinates, which were defined thus: z extended downwards along the vertical axis and was set to be zero at the base of the IDS coil; and r extended in a horizontal direction from a zero point at the centre of the IDS coil. The distance between the base of the IDS coil and the top of the target was denoted by d_t and was positioned at $z = d_t$.

Simulation Results

The complete parametric solutions to the aluminium, brass and copper problems each took approximately 15 min, whereas the nickel and steel problems each had a much higher solver time ~ 200 min. The FEA software required a finer mesh for materials with a high permeability than for those with a low permeability. This lead to an increase in the processor time that was required to solve the large number of elements and the large memory usage increased the processor time required for swapping page files between the virtual and physical memory.

An example of the simulation results is given by figure 4.2, which shows the influence of target material on $|B_z|$, the magnitude of the z-component of the magnetic field taken along a line 3 mm below the base of the IDS coil ($z = 3$ mm), for $d_t = 15$ mm. All the profiles have similar forms with a high central portion below the IDS coil and an outer lobe. The aluminium, copper and brass curves lie over each other and appear identical on the given scale, whereas the steel and nickel profiles are quite different.

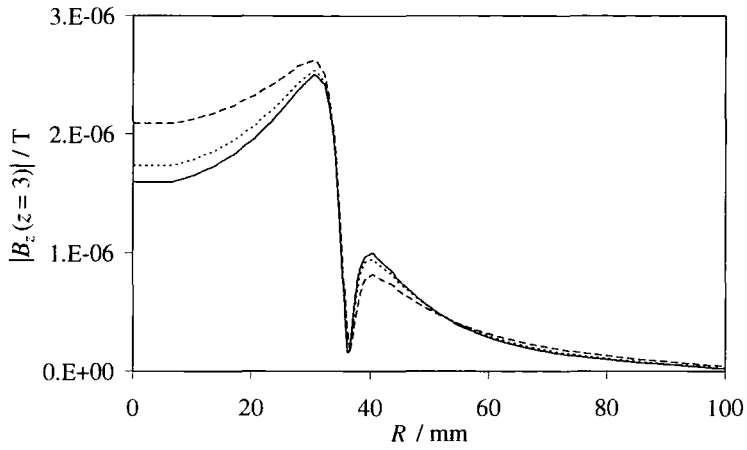

Figure 4.2. Influence of target material on the magnetic field, $|B_z(z = 3 \text{ mm})|$, from different target material simulations with d_t = 15 mm. R = 0 mm position is directly below the centre of the IDS coil. (Dash - - -) Steel-1008. (Dot ·····) Nickel. (Solid ——) Aluminium, copper, brass.

Steel has the highest central field value, which can be explained in terms of the skin effect. Equation (4.1) shows that the high permeability of steel means that it has a low standard depth of penetration. This decreases eddy currents in the target material and therefore decreases the field that opposes the incident IDS coil field. Hence the field below the IDS coil is not counteracted to the same extent that it is with lower-permeability materials. This is further illustrated by the plot of central field values given in figure 4.3. With increasing d_t the aluminium and steel curves meet as the influence of the target decreases. But more importantly, it is noted that the steel target gives a lower spread of central field values, which results from the skin effect.

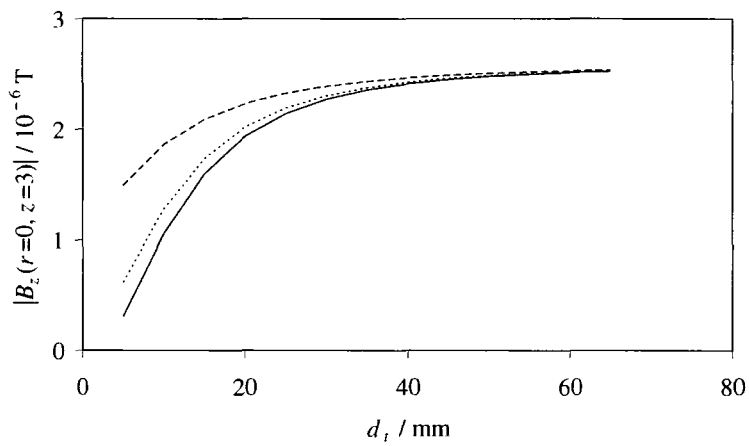

Figure 4.3. Variation in central field value, $|B_z(r=0, z=3)|$, with target displacement, d_t. (Dash - - -) Steel-1008. (Dot ·····) Nickel. (Solid ——) Aluminium, copper, brass.

The influence of target displacement on the IDS coil impedance is shown in figure 4.4. With increasing target displacement, the resistance decreases and the inductance increases, which is in agreement with the equivalent circuit equations (1.8) and (1.9). It can be seen that with nickel and steel targets the effect is substantially different to aluminium, brass and copper.

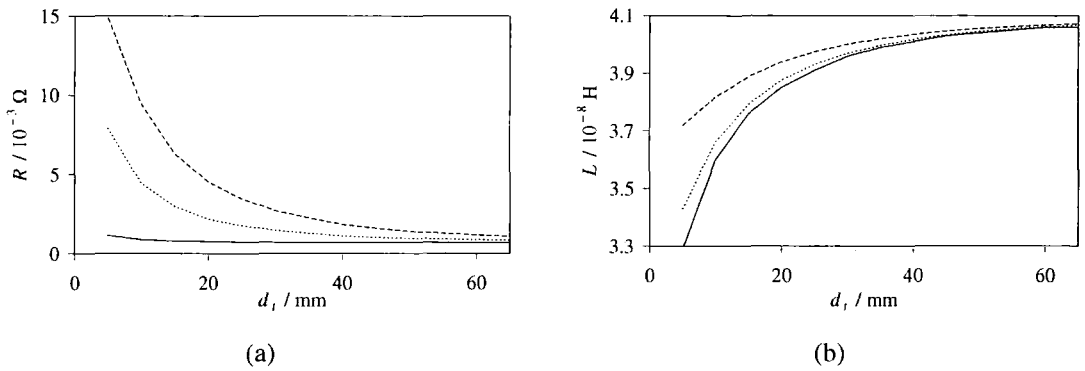

Figure 4.4. Impedance components as a function of target displacement, d_t. (Dash - - -) Steel-1008. (Dot ·····) Nickel. (Solid ——) Aluminium, copper, brass. (a) Resistance, R. (b) Inductance, L.

Edge Effects

The edge effect was introduced in section § 3.4.2 as the channelling of the magnetic flux around the edge of the target. Interestingly, the strength of the effect depends on the target material and it is weaker for steel (figure 4.5(a)) than it is for aluminium (figure 4.5(b)). Note that in these figures, the axis of abscissas starts at R = 35 mm, which corresponds to the edge of the IDS coil, so these plots only show the external lobes. It might be expected that the higher permeability of steel would increase the field channelling and thus increase the edge effect, however the higher permeability also leads to a smaller skin effect and the edge effect is reduced. This effect has important implications for electromagnetic shielding and is discussed by Marsh and Johnstone [40]. The edge effect decreases with target displacement and it was found that in general when the target was at $d_t >$ 30 mm, the edge effect could not be distinguished from the background field.

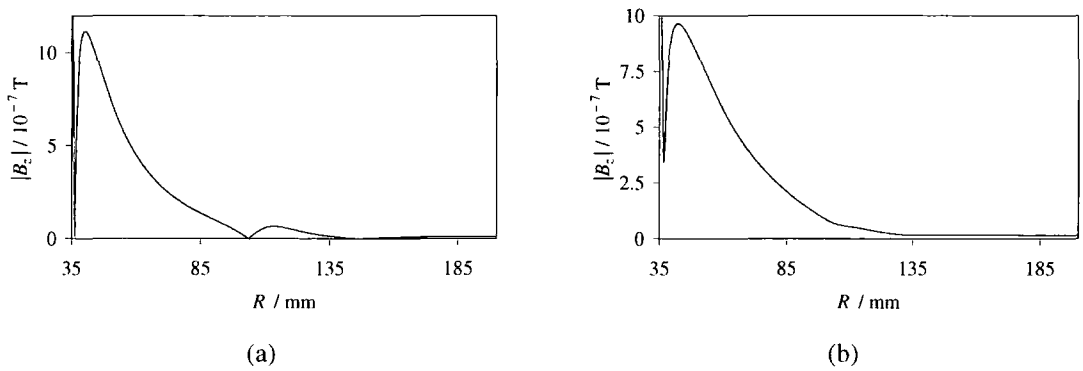

Figure 4.5. Dependence of edge effect on target material demonstrated by the field plotted along a line 1 mm below the IDS coil. (a) Aluminium. (b) Steel.

Further Investigations

Note from figure 4.2 that the form of the field profiles is the same regardless of the target material, however the central and outer lobe field values do change. Some further simulations were completed to investigate this fully and explore whether or not it provides more information about the target. Since the results for non-ferromagnetic materials were very similar, aluminium was arbitrarily selected for the further simulations with the assumption that it was also representative of copper and brass. Models were constructed to find a target displacement where $|B_z(r = 0, z = 3)|$ matched for both steel and aluminium targets. Since the aluminium problems were faster to solve, the displacement of aluminium was varied to match the field to that of existing steel results. Three different values of $|B_z(r = 0, z = 3)|$ were selected from previous steel simulations and for each a series of new aluminium results were found to home in on a target displacement with the same central field value. During each of the simulations impedance values were also calculated and the results are shown in table 4.2.

Table 4.2. Influence of target material on IDS coil impedance.

$\|B_z(r = 0, z = 3)\|$ / T	Sample Material	d_t / mm	$R / 10^{-4}\ \Omega$	$L / 10^{-8}$ H
2.316×10^{-6}	Steel-1008	20.0	0.448	3.976
	Aluminium	28.2	7.279	3.944
2.405×10^{-6}	Steel-1008	25.0	3.685	3.975
	Aluminium	32.9	7.211	3.968
2.467×10^{-6}	Steel-1008	30.0	2.826	4.000
	Aluminium	37.8	7.145	4.002

It was found from plots of the results that matching the central field values also matched the lobe values and so the profiles were identical. This meant that it was only the magnitude of the field that changed with target displacement and not the shape of the field. This implies that

looking at the field profiles in this way cannot provide any more information about the target material than is already available from the coil impedance.

4.1.3 Target Material Summary

The influence of target material on the output from the IDS has been investigated and it has been shown that this is a real problem. FEA simulations have been completed for a range of target displacements to several different target materials. Investigation of the coil impedance matrix confirmed that the simulations were in agreement with the theoretical equivalent circuit treatment of the system. Further simulations to match the magnetic field profiles of different target materials revealed that it is just the magnitude of the field that changes with target displacement and not the shape of the field. The coil impedance and field are not independent variables and so this method can not reveal any more information about the target. In summary, a target-independent IDS cannot be realised by measuring the magnetic field in this way.

4.2 Target Offset

In section § 1.4.3 the influence of target offset on the reliability of inductive eddy current displacement sensors was introduced. From an empirical point of view, as the target offset increases one expects the reliability of the IDS to decrease, that is, the target displacement and output voltage will no longer be linearly related. This section shows how this effect was investigated; the limitation was characterised experimentally and theoretically (§ 4.2.1), the set up was modelled with EM FEA simulations (§ 4.2.2) and experiments were used to confirm the results (§ 4.2.3).

4.2.1 Characterising the Effect of Target Offset

The influence of target offset on the output of an IDS was investigated with an experimental characterisation. The target material was set at a fixed displacement and the IDS output voltage was recorded for different lateral displacements. The target displacement was then changed and a new set of readings was taken.

The target width was fixed at 2.6 times the IDS coil diameter since this is of sufficient size to avoid the edge effects from too small a target width. The Kaman IDS under test was calibrated with aluminium and so this was the logical choice for the target material in these experiments. The results of the previous chapter reveal that the results are similar for materials with a low permeability and so aluminium is a good representation of copper and brass targets too. The target was cut from 5 mm thick plate, which is much larger than the skin depth (see table 4.1).

The thickness also increased the consistency of the results, since it meant that the target was flat as it did not distort as readily as thinner samples.

The IDS and target were separated by non-conducting spacers and three experiments were conducted with target displacements of 10, 20 and 30 mm. Figure 4.6 shows the results and gives the output of the IDS in terms of the percentage error in predicted target displacement. This is simply defined by

$$\%\ \text{distance error} = \frac{d_{t(IDS)} - d_t}{d_t} \times 100 \tag{4.4}$$

where $d_{t(IDS)}$ is the target displacement that corresponds to the recorded IDS output voltage, whereas d_t is the actual target displacement. The results confirm that the output from the IDS becomes less reliable as the target offset increases. Note that small errors for d_t = 10 mm at low offsets are a result of experimental errors where very small changes in voltage lead to a percentage distance error of ~ 1 %. As increasing offset leads to the coil and target edges aligning at ~ 0.8 times the IDS coil diameter the error becomes large and beyond this point the readings are highly unreliable. The lower the target displacement, the larger the offset could be without affecting the IDS output. However, higher target displacements were found to have a lower error at higher offsets. For offsets larger than those shown in this figure, the curves reached plateaux when the target no longer has an influence on the IDS.

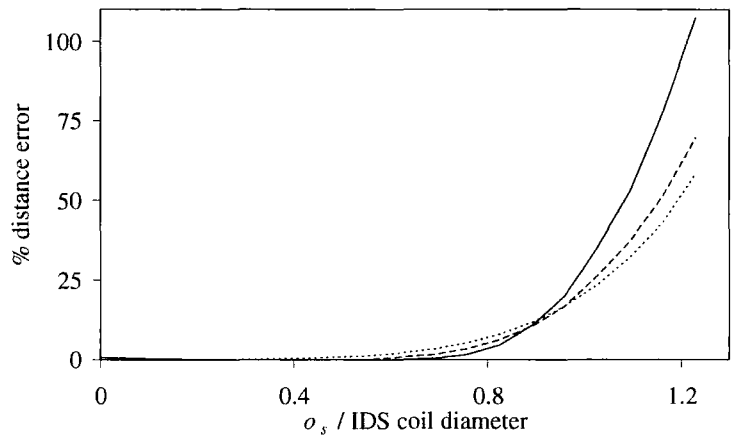

Figure 4.6. Influence of target offset on IDS output. Normalised IDS output with target offset, o_s, at different target displacements, d_t. (Solid ——) d_t = 10 mm. (Dash - - -) d_t = 20 mm. (Dot ·····) d_t = 30 mm

4.2.2 FEA Simulations of an Offset Target

The results of the previous section reveal that the IDS coil is affected by target offset, but further investigations were required to determine the reasons for the effect. FEA simulations were completed to determine the patterns of the field around the IDS coil. A three-dimensional geometry was used since the influence of the target on both sides of the IDS coil was of interest i.e. the influence of the advancing target edge and the receding target edge. Using the parametric methods described in section § 3.3.3, geometries were constructed with target offsets $o_s = 0, 5, \ldots, 150$ mm for target displacements $d_t = 10, 15, \ldots, 30$ mm.

Figure 4.7 shows the influence of large offsets on the field profiles. As the edge of the target moves below the IDS coil, the magnitude of the field below the coil increases. This is because the influence of the eddy currents decreases and therefore the IDS coil field is not counteracted to the same extent as when the target lies directly below the coil.

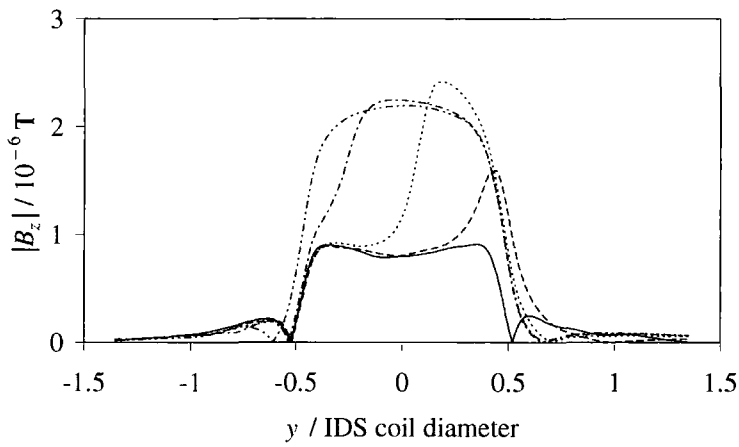

Figure 4.7. Field profiles for large offset targets for $d_t = 10$ mm. (Solid ——) $o_s = 0$ mm. (Dash - - -) $o_s = 100$ mm. (Dot ·····) $o_s = 100$ mm. (Dash dot - · - ·) $o_s = 125$ mm. (Dash dot dot —··) $o_s = 125$ mm.

More practical use can be made of the results of smaller offset models as shown by the example field profiles with offsets $o_s = 0, 20, 40, 60$ mm that are given in figure 4.8. Figures 4.8(a) – 4.8(d) show the field profiles for $d_t = 10$ mm and figures 4.8(e) – 4.8(h) show the field profiles for $d_t = 30$ mm. Note that the axis of abscissas focuses on the lobe regions and is scaled in terms of the IDS coil diameter (72 mm) e.g. the edge of the coil corresponds to $y = 0.5$. Particular attention should be paid to the variations in the field for the same offset, but different target displacements. For large target displacements, the $d_t = 30$ mm plot contains just one lobe that decreases in magnitude with increasing target offset. The peak of the lobe remains at the

same position, independent of the offset. However, the $d_t = 10$ mm field includes three lobes and the middle lobe is drawn to the left as the target edge advances. The difference between the $d_t = 10$ mm and $d_t = 30$ mm field profiles is a result of the target edge effect, which was discussed in section 3.4.2.

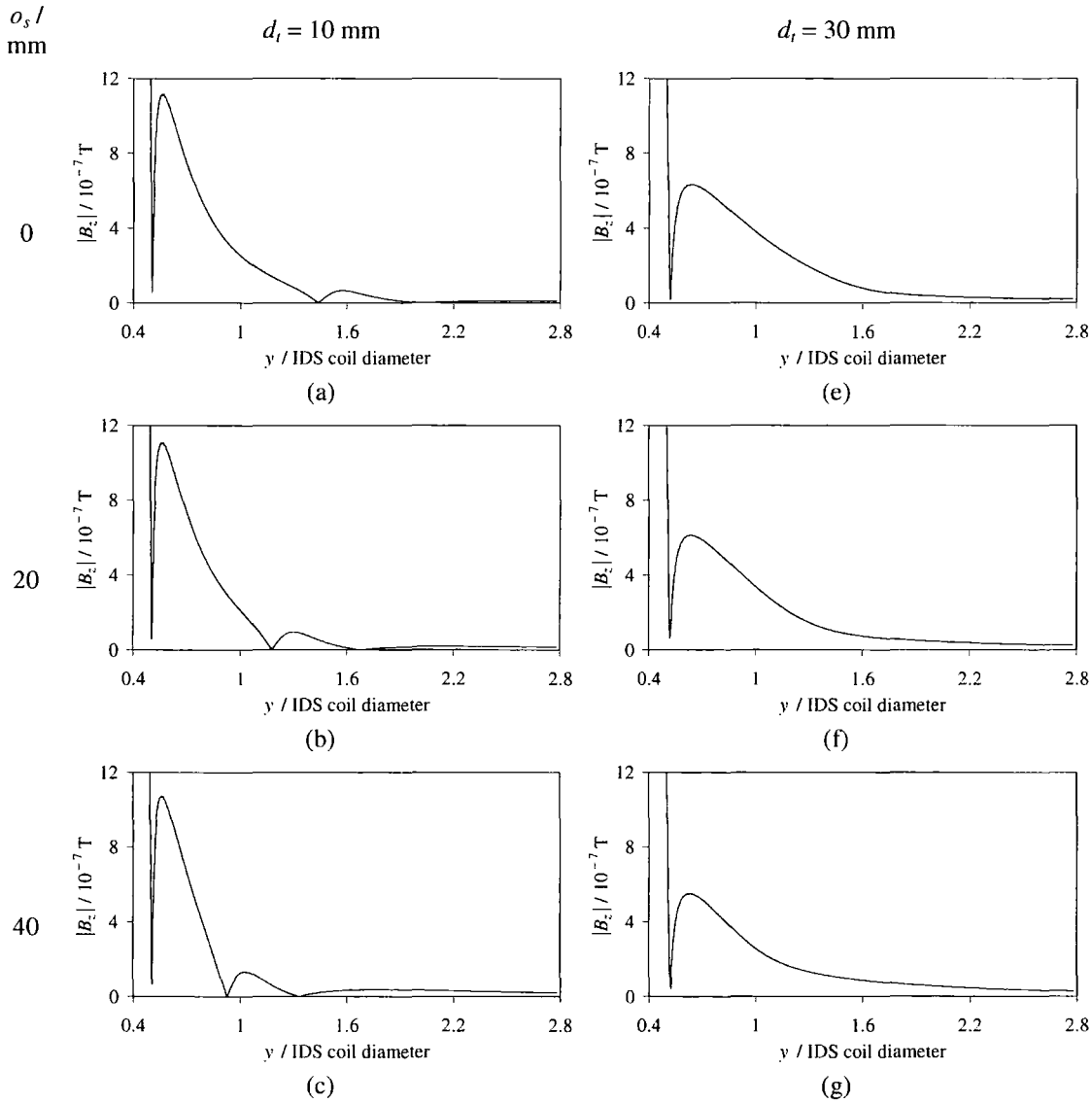

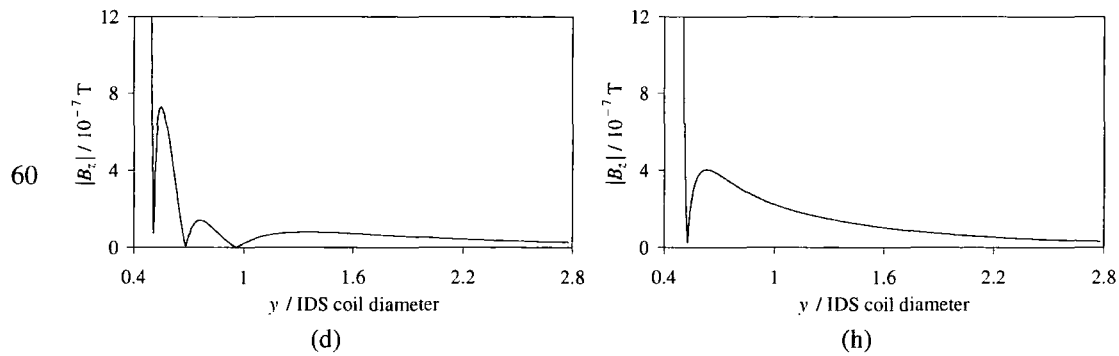

60

Figure 4.8. FEA simulations of offset targets at different target displacements. (a) – (d) d_t = 10 mm. (e) – (h) d_t = 30 mm.

Figure 4.9 shows the influence of target offset on the IDS coil inductance for different target displacements. With increasing offset, the curves converge to a point as the influence of the target diminishes. These results are in agreement with the equivalent circuit model described by equation (1.9), which shows that closer targets result in a lower IDS coil inductance because of the stronger coupling to the target.

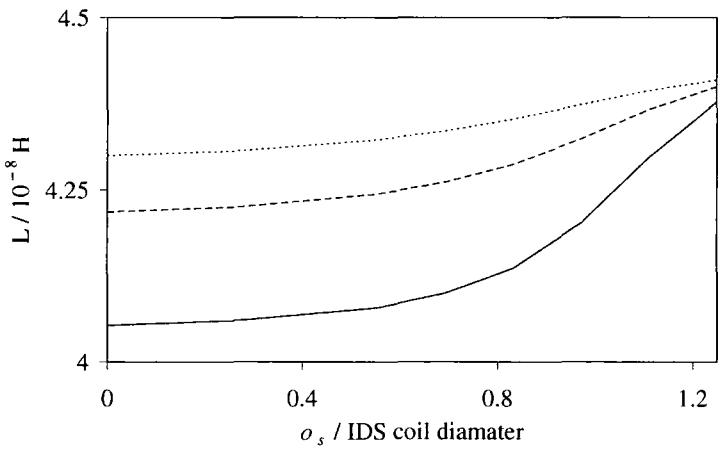

Figure 4.9. Influence of target offset on coil inductance. (Solid ——) d_t = 10 mm. (Dash - - -) d_t = 20 mm. (Dot ·····) d_t = 30 mm

Figure 4.10 shows the change in coil impedance and lobe amplitude with target offset. Recall that the IDS measures target displacement only using the coil impedance.

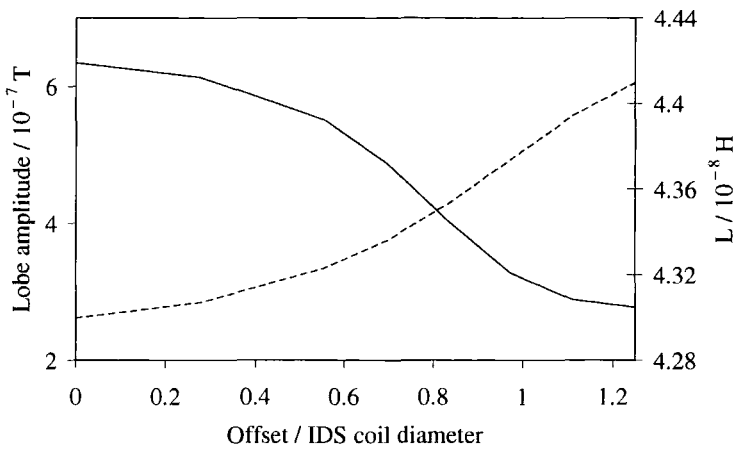

Figure 4.10. IDS coil impedance and magnetic field lobe amplitude for d_t = 30 mm. (Left, solid ——) Lobe amplitude. (Right, broken - - -) IDS coil inductance.

4.2.3 Experimental Measurements of an Offset Target

The results of the previous section were confirmed by experimentally measuring the output from the IDS taking test coil readings at the same time. For d_t = 25 mm and with a target width of 3.3 times the IDS coil diameter, the target was offset and readings taken. The results are given in figure 4.11, with the test coil output scaled such that a value of 1 corresponds to the reading with no offset and the IDS output scaled to give the percentage distance error.

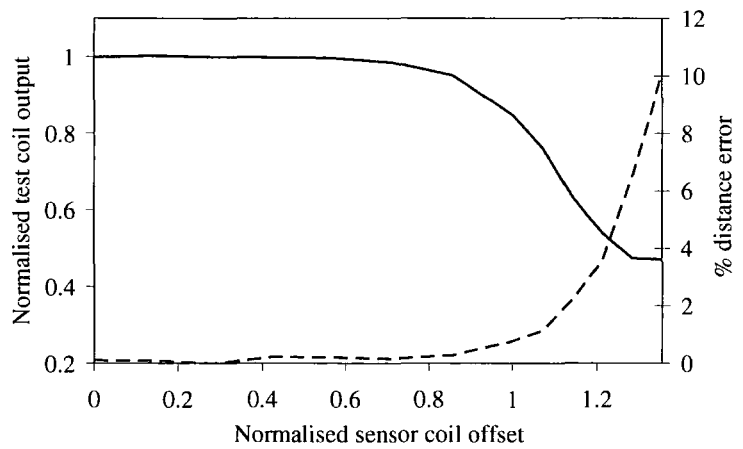

Figure 4.11. Experimental confirmation of FEA simulation results. (Left, solid ——) Normalised test coil signal. (Right, broken - - -) IDS distance error.

4.2.4 Target Offset Summary

The influence of target offset on the output of the IDS has been characterised and was shown to be a real problem that leads to a decrease in reliability of the measurements from the system.

The lower the target displacement, the larger the offset could be without affecting the IDS output. However, higher target displacements were found to have a lower error at higher offsets. FEA simulations were conducted and the results were found to agree with experimental measurements. It is proposed that by using an array of small test coils around the IDS it would be possible to compensate for the influence of target offset on the IDS output. The relationship between the lobe shape and amplitude is not trivial and either a look-up table or a trained artificial neural network could be utilised to convert test coil measurements into an IDS correction factor. In this way, the influence of target offset on the output from an IDS could be corrected, which would result in more reliable displacement measurements.

4.3 Target Width

The influence of target width on the output from an IDS was introduced in section § 1.4.2 and is closely related to target offset. In this section the effect of using targets smaller than the recommended width is investigated, which begins with a characterisation of the effect in section § 4.3.1, where it is shown that the problem is real and the resulting measurement errors are calculated. The results of FEA simulations are presented in § 4.3.2 and conclusions are drawn in section § 4.3.3.

4.3.1 Characterising the Effect of Target Width

The influence of target width on the output from the IDS was characterised experimentally. As in the previous section, aluminium plate targets with a thickness of 5 mm were used since the IDS was factory-calibrated for this material; the thickness targets ensured a flat surface for the experiment. Two experiments were completed: the first measured influence of target size on the IDS output voltage for a fixed target displacement; the second concerned using the IDS to measure the displacements to different target widths. For both experiments, target displacements were controlled with non-conducting plastic spacers.

The target was maintained at a constant displacement, $d_t = 20$ mm and the output from the IDS was measured with different target widths. The targets used in the experiment were as follows: 2.6, 2.4, ..., 1.2, 1.0 times the IDS coil width. As the effects were observed to increase sharply as the target size approached the diameter of the IDS coil, an additional target was constructed with a width of 1.1 times the IDS coil width. Figure 4.12 shows the results from the experiment, from which it can be seen that as the target width increases, the accuracy of the IDS increases. The curve levels out, which shows that using a target wider than about 2.5 times the IDS coil diameter does not improve the IDS accuracy.

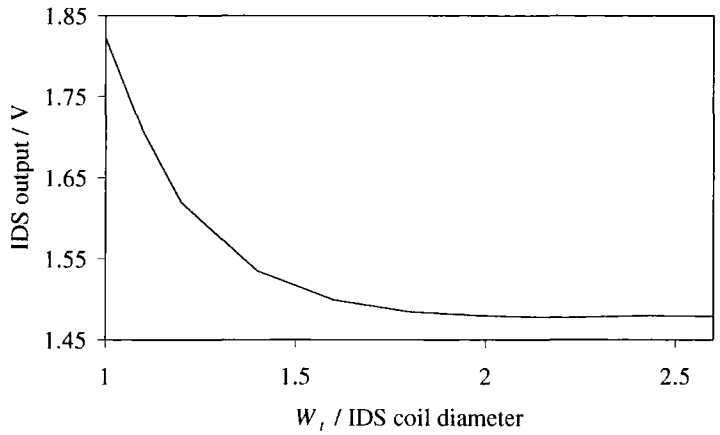

Figure 4.12. Influence of target width on the IDS output.

In the next experiment, three target sizes were investigated: 2.6, 1.4 and 1.2 times the IDS coil width. For each target, the output from the IDS was measured at different target displacements. The results are shown in figure 4.13, from which it can again be seen that the IDS reliability deteriorates with decreasing target width. Figure 4.13(a) shows that the linearity of the system is dependent on the target width and displacement. Smaller targets give reliable results at lower target displacements and it is only when the target is moved further away that the output deviates from a linear response. By comparing the measured voltage with the output that would be expected at a given target displacement, a measure of distance error can be obtained, which is defined by equation (4.4). This error is plotted for target displacements larger than 25 mm in figure 4.13(b).

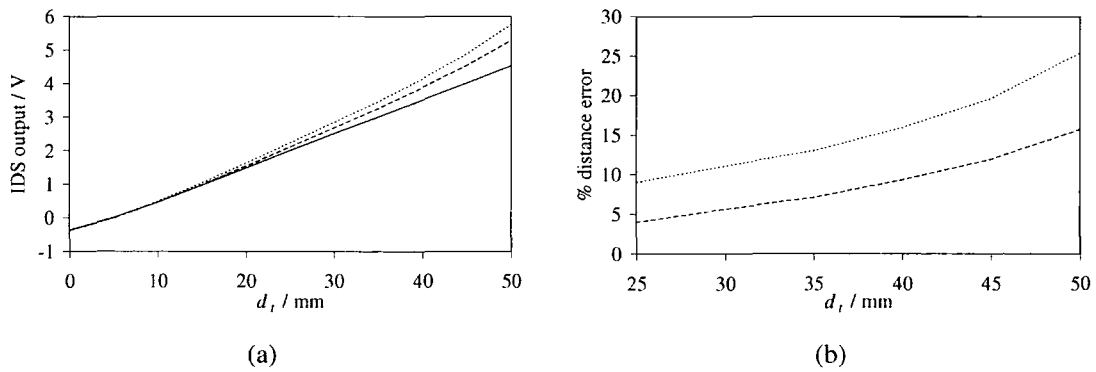

Figure 4.13. Influence of target width on the IDS output. (Solid ——) w_t = 2.6. (Dash - - -) w_t = 1.4. (Dot ·····) w_t = 1.2. (a) Non-linearity introduced with different target widths. (b) Distance measurement error resulting from small target widths.

4.3.2 FEA Simulations of the Effect of Target Width

Using Ansoft's Maxwell 3D program, the influence of an offset target on the field around the IDS was investigated. The three-dimensional module was selected because as the width of the target decreased, the influence of the corners increased and so the approximation that the target was axially symmetric — as had to be assumed in two-dimensional simulations — increased the modelling error to an unacceptable level. Two groups of simulations were run: one with $d_t = 10$ mm and another with $d_t = 20$ mm. For each group, nine simulations were run with each having a different target width.

Some results from the FEA simulations are presented in figure 4.14, which shows the influence of target width on the field profiles. Figures 4.14(a) – 4.14(c) are for a target displacement of $d_t = 10$ mm and figures 4.14(d) – 4.14(e) are for a target displacement of $d_t = 20$ mm. Comparing these figures with figure 4.7, highlights the difference between the influences of target offset and target width. As has been explained in previous sections, the central portion of the field, below the IDS coil, is reduced in magnitude for a lower target displacement. The influence of an offset target is to skew this central portion, whereas a small target width gives a skewed effect for both sides and the result is a central dip. This is less prominent at higher target displacements, which indicates that it results from the edge effect that was described in section § 3.4.2.

The influence of a small target width on the outer lobes is similar to that observed for an offset target. At small target displacements, the edge effect causes the outer lobes to be broken into separate lobes. However at large target displacements, this effect is not present and there is a single lobe that decreases in magnitude with decreasing target width.

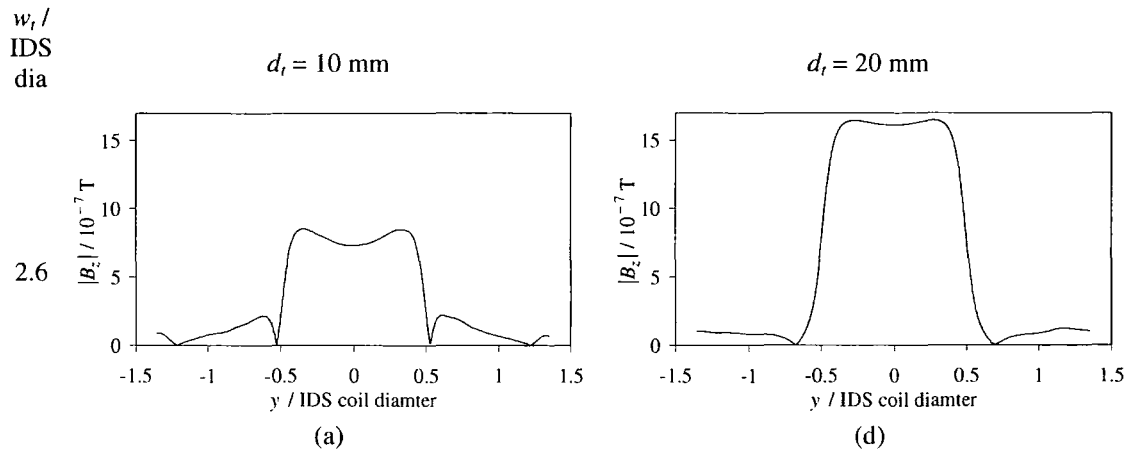

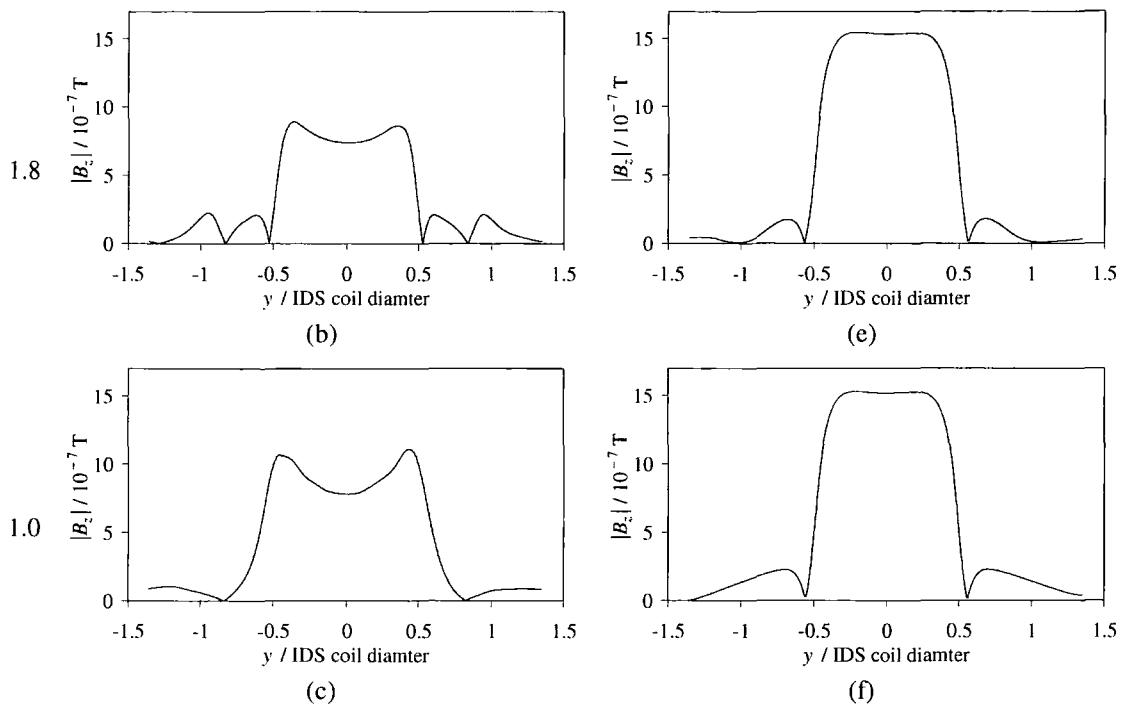

Figure 4.14. FEA simulations of the influence of target width on the magnetic field. (a) – (d) d_t = 10 mm. (e) – (h) d_t = 20 mm.

4.3.3 Target Width Summary

The use of small targets on the output from IDSs has been characterised and it was shown that there is a real effect on the reliability of the distance measurements. The effect is similar to that of an offset target and at low displacements the target affects the lobe shape. A similar array of test coils that was proposed to measure an offset target could also be used to counter the influence of target width.

4.4 Summary

In this chapter the techniques developed previously were applied to investigate the limitations of IDSs. The test coil design that was described in chapter two was applied to measure the field around the test coils experimentally and the FEA methods discussed in chapter three have been utilised to simulate these fields. A combination of two- and three-dimensional FEA simulations have been used to investigate the influence on the IDS output of target material, target offset and target width.

The effect of target material on the IDS was demonstrated by obtaining two equations for the measured voltages and the corresponding target displacement: for steel $V = 0.087d_t - 0.049$ and for aluminium $V = 0.091d_t - 0.184$, each with an R^2 value of 0.997. Solutions for steel and

nickel problems took approximately 13 times longer than aluminium, brass and copper targets. The field profiles for aluminium, brass and copper overlapped and with $d_t = 5$ mm, the $|B_z(r = 0, z = 3)|$ values were 3.07×10^{-7} T. The values were 6.15×10^{-7} T and 1.49×10^{-6} T for nickel and steel respectively. The difference resulted from reduced coupling to the higher permeability materials, which is a consequence of the skin effect. As $d_t \rightarrow \infty$ and the influence of the target material decreased, the central field values all tended to the same value of 2.53×10^{-6} T. Further simulations showed the edge effect was stronger for an aluminium target than a steel target. The impedance results were observed to follow the equivalent circuit models. Further steel and aluminium simulations were ran to match the central field values. This was also found to match the lobe amplitudes and so it was determined that monitoring the lobes did not reveal more information about the target material.

The influence of an offset target on the reliability of an IDS was investigated experimentally and with FEA simulations. An experimental characterisation of the influence of offset revealed that the lower the target displacement, the larger the offset could be without affecting the IDS output, but conversely that higher target displacements yield a lower error at higher offsets. For example with $o_s = 1.23$ times the IDS coil diameter the distance errors were 107, 70, 58 % for $d_t = 10$, 20, 30 mm respectively. FEA investigations showed that the impedance of the IDS coil followed the behaviour described by the equivalent circuit equations. The value of the simulated impedance with the target at a large offset was approximately 20 % larger than for the same experiment conducted in 2D for the material investigation.

The target edge effect was found to play an important part in shaping the lobes at low target displacements. At low target displacements the field external to the IDS was found to comprise a number of distinct sub-lobes, whereas at higher target displacements only a single lobe was found. By monitoring the lobe amplitudes with a test coil array it was found that the effect of an offset target could be corrected. For example, with $d_t = 25$ mm and $w_t = 3.3$ times the IDS coil diameter, when $o_s = 1.2$ times the IDS coil diameter the distance error was 3.6 %, which corresponded to a normalised test coil output of 0.54.

The influence of target width on the IDS was demonstrated to be similar to that of target offset and edge effects were again important at low target displacements. It was proposed that the lobes could be monitored using an array of test coils and either a look-up table or an artificial neural network could used to compensate for the affects of target offset.

Chapter 5

Conclusions

The primary aim of the work described in this thesis was to investigate the limitations of inductive proximity sensors and it was initially proposed that measuring the field external to an IDS could provide more information than was available from the IDS coil impedance alone.

The first chapter included a general discussion about displacement sensing and applications where different technologies are appropriate. Particular emphasis was placed on comparing behaviour in harsh environments where dust, dirt, oil, humidity, etc. can interfere with the measuring process. This discussion lead to the confirmation that IDSs were suitable for making displacement measurements in harsh industrial environments and that they had advantages over other technologies that could not perform as well in these conditions. The discussion of IDS operating principles lead to an understanding of their limitations and it was shown that target material, offset and width affected the sensors. IDSs have been widely used in industry for a number of years and many systems are available commercially, consequently it was determined that an investigation of their limitations was an important physical problem.

The field around the IDS coil was found to be sinusoidal with a magnitude ~ 10^{-6} T and a frequency of 1 MHz. A comparison of magnetic sensing technologies in the second chapter determined that a number of devices are available that can measure a field with these characteristics although many — such as SQUIDs — would be impractical for the application environment. A simple test coil was shown to be the most appropriate device for this application, although a phase locking signal processing technique was required to produce a high signal to noise ratio at low field strengths ($< 2 \times 10^{-6}$ T). Before processing, an example signal was found to have a mean amplitude of 4.65×10^{-4} V with a variance of 4.36×10^{-7} V^2, but the phase-locking technique revealed an amplitude of 0.0324 V with a variance of 1.12×10^{-7} V^2. Hence a system was developed that could reliably measure the magnetic field around the IDS coil.

The third chapter described work to simulate the magnetic fields around IDSs with commercial FEA software. Both two- and three-dimensional models were constructed, tested and refined to produce smooth field values. Central field values produced by the 2D and 3D models were 2.6×10^{-6} T and 2.7×10^{-6} T respectively, which matched the experimentally

measured value of ~ 5×10^{-6} T. Also, investigation of the influence of target displacement on the impedance of the IDS coil found the behaviour to match with the equivalent circuit models. Hence the simulations were shown to be an accurate model of the experimental equipment. A program, that was developed to convolve the simulated field and test coil response, was found to improve the match between experimental and simulation results and the result was a system suitable for the investigation of limitations of IDS systems.

The effect of target material was shown to be real experimentally by calibrating the IDS, which was demonstrated by the two relations: $V = 0.087d_t - 0.049$ (for steel) and $V = 0.091d_t - 0.184$ (for aluminium), each with an R^2 value of 0.997. Simulations were setup that produced impedance values that agreed with theoretical models. These simulations showed that the field profiles of aluminium, brass and copper were very similar and when $d_t = 5$ mm, the $|B_z(r = 0, z = 3)|$ values were 3.07×10^{-7} T. For nickel and steel, the values were 6.15×10^{-7} T and 1.49×10^{-6} T respectively. This demonstrated how the permeability of the target material affected the IDS field. Further simulations were completed to investigate this further and it was found that varying d_t to match the central field values also matched the lobe amplitudes. This meant that it was not possible to reduce the target dependence by monitoring the field in this way.

The target offset effect was demonstrated experimentally by measuring the distance error with offset. For example when $o_s = 1.2$ times the IDS coil diameter, the distance errors were 107, 70, 58 % for $d_t = 10$, 20, 30 mm respectively. This showed that the target offset effect was a real problem that could potentially have made measurements highly unreliable. FEA simulations revealed the effect of the offset targets on the magnetic field around the IDS. Agreement was found between the simulated and theoretical coil impedance variations, which confirmed the appropriateness of the model. The external field lobe on the side nearest the leading offset edge was affected while the trailing edge was unaffected. Two key features in the leading edge lobes were observed: the amplitudes decreased with increasing offset and at low target displacements the edge effect caused the lobes to split. An experiment with the test coil array confirmed that it was possible to use the change in lobe amplitude to measure the offset of the target, for example when $d_t = 25$ mm and $w_t = 3.3$times the IDS coil diameter, with $o_s = 1.2$ times the IDS coil diameter the distance error was 3.6 %, which corresponded to a normalised test coil output of 0.54. Hence it was possible to correct the output signal from the IDS coil to counteract the effect of an offset target.

Target width was found to have a similar effect to target offset. Again, experiments were completed which showed that the effect was a real problem, for example with $d_t = 20$ mm when

w_t = 1.2 times the IDS coil diameter, the output was 8 % larger than it was when w_t = 2.5. FEA simulations showed that both sides of the IDS external field lobes were affected by the smaller target compared to just one side with an offset target. The same features were observed in the field lobes: the amplitudes decreased with increasing offset and at low target displacements the edge effect caused the lobes to split. Hence it was possible to measure the lobe amplitudes and correct the IDS output to compensate for the target width effect.

Future work could develop the test coils further and produce an array suitable for use in harsh environment applications. Also, the target offset and width corrections could be developed with the use of either look-up tables or artificial neural networks to utilise the lobe splitting that was caused by the edge effects.

The macros and the convolution program were very versatile and future work could utilise them as they could easily be adapted to use new geometries and materials. The experiments for the effect of target offset and width only looked at aluminium targets, which were taken to be representative of targets with a low permeability. Steel targets were not simulated because of the time taken to produce solutions, which was a consequence of the large mesh sizes. Future work could complete these experiments on a more powerful computer. A further parameter that could be investigated is target thickness; simulations could be run to see the effect of using targets approaching the skin depth. This could also be achieved by modifying the macros.

The frequency of the IDS coil that was simulated was fixed, however the skin effect was dependent on the frequency of the exciting radiation and so simulations involving different frequencies or a burst of frequencies would be worthwhile.

When measuring the magnetic fields, only the magnitude of the test coil signal was measured. In practical experiments phase information was lost in the signal processing program and in the FEA simulations the phase information was not collected by the macros and convolution program. Further work could investigate the effect of the parameters on the phase of the test coil signal.

Appendix 1

Published Research

The paper "*Improving the Reliability of Eddy Current Distance Measurements with Finite Element Modelling*" by M. R. Wilkinson and S. Johnstone was taken to The Institute of Physics Sensors and their Applications XII conference in Limerick, Republic of Ireland in September 2003. It is published in the book *Sensors and their Applications XII* (0750309748) by Institute of Physics Publishing in 2003. It is reprinted here with permission.

Improving the Reliability of Eddy Current Distance Measurements with Finite Element Modelling

M. R. Wilkinson, S. Johnstone

School of Engineering, University of Durham, South Road, Durham, DH1 3LE, United Kingdom

Abstract: Eddy current distance measuring devices are used widely in a number of harsh environment applications. However they have limitations and this paper looks at the effect of non-centred targets on the reliability of such devices. It was found that when a target was offset by 1.3 times the sensor coil diameter there was an error of 6.5% in the distance measured.

Finite element electromagnetic field simulations have been employed to model the system and have shown how the field outside the sensor coil changes with target offset. By monitoring this field with small test coils it is possible to correct the distance measurement error. This work has potential to lead to an improvement to the range of applications in which eddy current distance measuring devices may be employed.

1. Introduction

Eddy current sensors (ECSs) [1] are widely employed to measure the distance to conducting targets in harsh environments [2]. Such true position measuring devices comprise a sensor coil and associated electronics. An alternating current is passed through the coil to generate an electromagnetic field. When a conducting target material is placed in this field, eddy currents are generated which produce an opposing field thus reducing the original intensity. This causes an impedance variation in the sensor coil which is detected by the monitoring electronics. The distance to the target is given as a voltage that is directly proportional to the target displacement. Non conducting materials between the ECS and target will not affect the field and so they can operate in environments where dust, oil or humidity, etc. are present. This is a major advantage over other distance measuring devices.

The distance range over which an ECS will provide linear results is directly proportional to the diameter of the ECS coil. The magnetic field around ECSs with a shield is less extended than for unshielded designs. This has the effect of reducing the measuring range, but means that smaller targets may be used. For shielded ECSs the target size should be at least 1.5 to 2 times the ECS coil diameter and for unshielded ECSs the target should be at least 2.5 to 3 times the ECS coil diameter [3]. Using a target size smaller than these limits reduces the linearity and long term stability. A similar effect is observed when the target is offset from centre; that is the target extends a greater distance on one size of the ECS coil than on the other. Previous authors have looked at various aspects of ECS reliability [4, 5], but this paper summarises research into a solution to the offset problem and is a subset of wider work on the limitations of ECSs.

Experimental work was carried out using a commercially available eddy current distance measuring device from Kaman Instrumentation. This enabled the researchers to avoid the complication of constructing and fine-tuning such a device [6] and meant that the limitations of a well calibrated system were investigated. The system was modelled using Ansoft's *Maxwell3D*™ finite element electromagnetic field solver using an eddy current module; this is detailed in section two. The results of these simulations have been confirmed experimentally (section three) and section four shows how they were interpreted and exploited.

2. Simulation of Target Offset

There are a number of modelling methods through which more can be learnt about electromagnetic sensor designs. Early analytical work on shielding and eddy current problems [7, 8] is relevant but limited to simple geometries. Probable flux methods [9] are suitable for complex geometries, but often require large assumptions. However with increasing computing power rigorous numerical finite element methods [10, 11] have proven to be useful in three dimensional and high frequency cases [12].

The ECS coil was modelled as a 1 mm wide rectangle swept 360° around a central axis with an alternating current source running at 1 MHz. The magnetic field strength was measured below the ECS coil using a test coil. By treating it as a solenoid, the amplitude of the current in the coil was estimated. This value was then adjusted so that the simulated field strength matched the measured field strength. The ECS coil was located above a square aluminium target that was positioned with various offsets relative to the ECS coil as illustrated in figures 1(a) and 1(b). The target material had a width of 3 times the ECS coil diameter and a thickness of 5 mm. The distance between the ECS coil and the target was fixed at 20 mm.

Finite element field solutions were computed on a fine mesh and the magnitude of the magnetic field in the direction along the ECS coil axis (z-axis in figure 1), $|B_z|$, was measured on a line perpendicular to the ECS coil axis (y-axis in figure 1) in the region between the ECS coil and target.

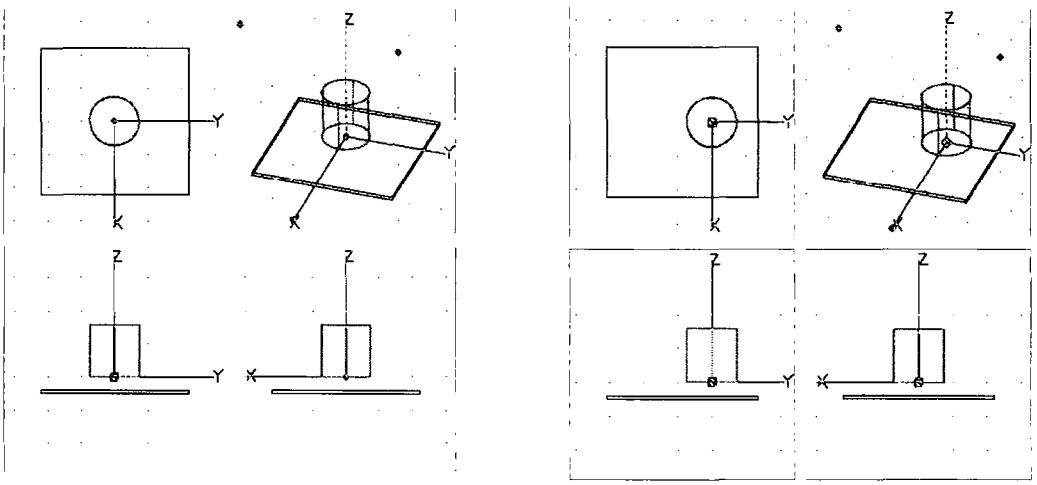

(a) (b)

Figure 1. Wire frame perspectives of the problem geometry for (a) a target offset of zero and (b) a target offset of 0.6 times the sensor coil diameter.

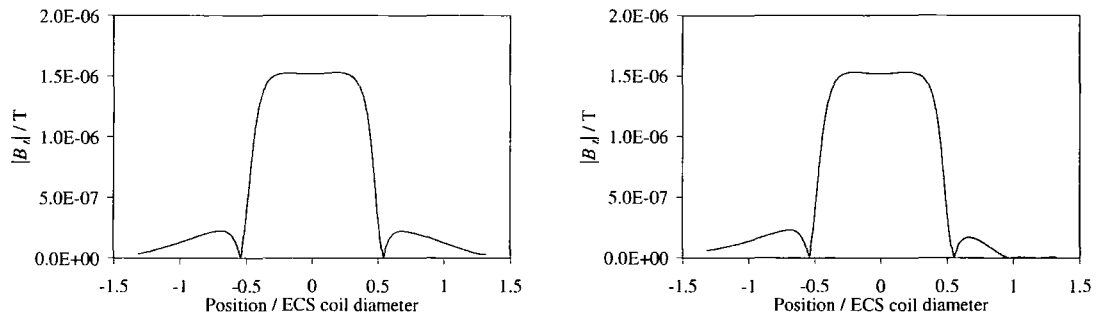

Figure 2. The field profiles for (a) a target offset of zero and (b) a target offset of 0.6 times the sensor coil diameter.

The field was found to consist of a higher central portion immediately below the ECS coil and two 'lobes' to either side. As the offset was increased (i.e. the ECS coil was displaced laterally relative to the target centre) the lobe on the side closest to the advancing target edge decreased in magnitude and was curtailed in its lateral extension. This is illustrated in figure 2 which shows the field patterns for an offset of zero and an offset of 0.6 times the ECS coil diameter.

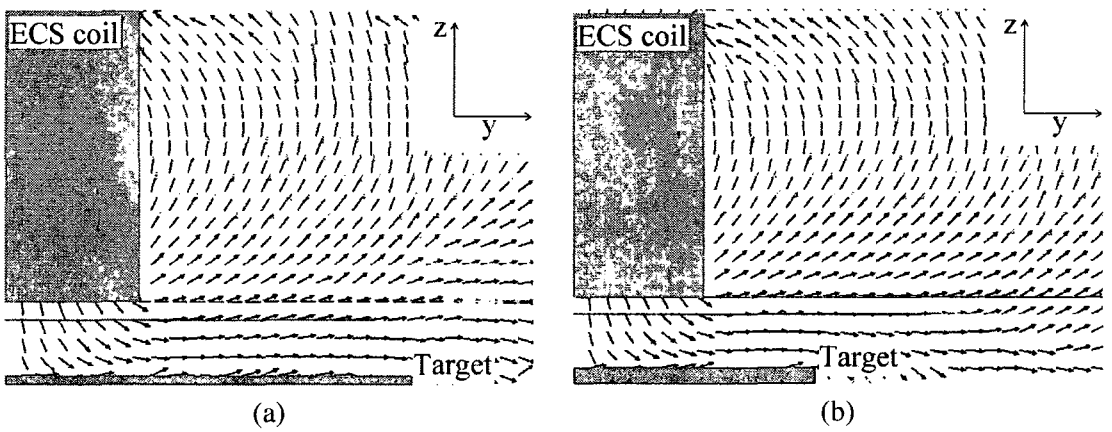

Figure 3. Direction of the magnetic field for a given phase angle on the y-z plane cross section through the ECS coil, target and profile line for (a) a target offset of zero and (b) a target offset of 0.6 times the sensor coil diameter. Note that the magnitude of the field is not shown by this diagram.

The form of the field profiles may be understood in terms of the direction of the magnetic field vectors as illustrated by figures 3(a) and 3(b). Below the centre of the ECS coil the vectors are vertical (large z-component) as they are within the coil. Moving along the profile line away from the ECS coil centre the flux lines start to curve around and the vector takes on an increasing horizontal component. Immediately below the ECS coil edge the vector is horizontal (large y-component) and the there is a dip on the curves of figures 2(a) and 2(b). For the zero-offset geometry the z-component of the field increases as the flux lines sweep back up to join the upper end of the ECS coil. $|B_z|$ then drops off as the field decays with increasing displacement from the source. For the

geometry with an offset of 0.6 times the ECS coil diameter there is also an initial increase as the flux sweeps back up, however in this case the target edge comes into play. Some of the flux lines are swept down and around the target so the field lines are spilt. This has the effect of creating more horizontal than vertical components of the field and thus $|B_z|$ decreases.

3. Experimental Confirmation

The modelling results were confirmed by measuring the magnetic field outside of the ECS coil with small tightly-wound test coils. These test coils were constructed from fine copper wire and an air core was used so as to minimise the disruption to the field. The stranded nature of the devices meant that eddy current interactions were small. An Agilent Technologies impedance analyser was used to match the natural frequency of the test coils closely to the 1 MHz of the ECS coil; this enabled maximum response and sensitivity. The test coils were connected to a digital oscilloscope and the amplitude of the signal recorded.

Two test coils were employed and were positioned either side of the ECS coil on the y-axis in figure 1 so as so track changes in the lobes of figure 2. The offset of the target material was increased and the output from the test coils was recorded. This has been expressed in normalised terms to highlight the variation from the zero-offset case. The ECS output was also recorded and was observed to change as the offset increased, even thought the actual target distance (d_t) remained constant. This is expressed in terms of a percentage distance error, which is simply:

$$\%\ \text{distance error} = \frac{d_{t(ecs)} - d_t}{d_t} \times 100$$

where $d_{t(ecs)}$ is the distance given by the eddy current ECS.

Figure 4 shows the normalised output of the test coil on the side of the approaching target edge (i.e. positive y-axis position on figure 1) and the % distance error. For low values of the normalised ECS coil offset ($\leq$0.6), the small distance errors were caused by experimental limitations and were not actual device errors.

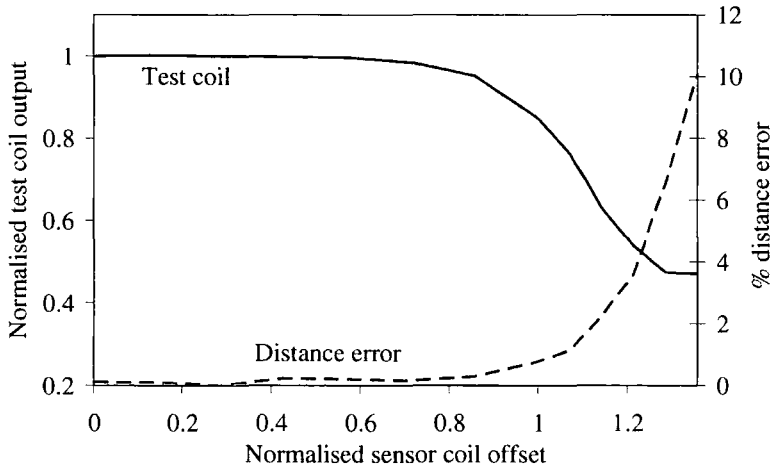

Figure 4. Graph showing percentage distance error resulting from target lateral displacement and the output from the test coil.

When the ECS coil and target edges were aligned (an offset of 1 times the ECS diameter) there was a 6.5% error in the target distance as given by the ECS. The output of a test coil positioned at 1.3 times the ECS coil radius was found to be 0.47 of the value when the target was centred. Thus by monitoring the test coils in this way, it was possible to correct for the errors caused by target offset.

The direction of the target offset was also determined by comparing the output from the two test coils. As can be seen in figure 2 only the lobe closest to the approaching target edge was affected; the opposite lobe remained static.

4. Conclusions

This paper has demonstrated by using finite element field simulations that there is more information available from the ECS system than is extracted by only measuring the impedance of the ECS coil. Outside the ECS coil lobes were observed in the z-component of the magnitude of the magnetic field. As the offset of the target material was increased the lobe on the side of the advancing target edge was observed to decrease in magnitude and its lateral extension was curtailed. By monitoring small test coils positioned to observe these lobes it was possible to counteract the effect on the ECS coil.

With further work the system of test coils and the ECS coil could be combined into a package that was resistant the harsh environment in which ECSs are often employed. The signal from the test coil could be monitored by an electronic system that could directly modify the output from the ECS device. This would make an eddy current distance measuring device that could be used in situations where the target materials were not always centred. Such applications include environments targets move through the path of the ECS (e.g. production lines) and where the target may be knocked out of alignment (e.g. rolling mills).

Acknowledgements

This work is supported by funding from the UK EPSRC reference number GR/R58475/01.

References

1. Welsby, S.D. and Hitz, T., *True Position Measurement with Eddy Current Technology.* Sensors Magazine, 1997. 14(11): p. 30-40.
2. Aknin, P., Placko, D., and Ayasse, J.B., *Eddy current sensor for the measurement of lateral displacement. Applications in the railway domain.* Sensors and Actuators A, 1992. 31: p. 17-23.
3. Kaman Instrumentation, *KD-2300 Instruction Manual Rev. E. (part no. 860021).* 2000, Kaman Corporation, P.O. Box 1, Bloomfield, CT 06002-0001, USA. p. 21-22.
4. Tian, G.Y., Zhao, Z.X., and Baines, R.W., *The research of Inhomogeneity in Eddy Current.* Sensors and Actuators A, 1998(69): p. 148-151.
5. Vasseur, P. and Billat, A., *Contribution to the development of a smart sensor using eddy currents for measurements of displacement.* Meas. Sci. Technol., 1994. 5(8): p. 889-895.

6. Roach, S.D., *Designing and building an eddy current position sensor.* Sensors Magazine, 1998. 15(9).
7. Levey, S., *Electromagnetic shielding effect of an infinite plane conducting sheet placed between circular coaxial coils.* P. IRE., 1936. 24(6): p. 923-941.
8. Dodd, C.V. and Deeds, W.E., *Analytical solutions to eddy-current probe-coil problems.* J. App. Phys., 1968. 39(6): p. 2829-2838.
9. Hugill, A.L., *Probable flux path modelling of an inductive displacement sensor.* J. Phys. E: Sci. Instrum, 1981. 14: p. 860-864.
10. Chari, M.V.K. and Silvester, P.P., eds. *Finite Elements in Electrical and Magnetic Field Problems.* Wiley Series in Numerical Methods in Engineering, ed. R.H. Gallagher and O.C. Zienkiewicz. 1980, Wiley-Interscience. 219.
11. Silvester, P.P. and Ferrari, R.L., *Finite Elements For Electrical Engineers.* 2 ed. 1990: Cambridge University Press. 344.
12. Johnstone, S. and Peyton, A.J., *The application of parametric 3D finite element modelling techniques to evaluate the performance of a magnetic sensor system.* Sensors and Actuators A, 2001. 93: p. 109-116.

References

1. Grattan, K.T.V. and S.H. Khan, eds. *Sensors and Their Applications XI.* Series in Sensors, ed. B.E. Jones. 2001, Institute of Physics.
2. Decker, W. and P. Kostka, *Inductive and Eddy Current Sensors*, in *Sensors: A Comprehensive Survey*, J.N. Zemel, Editor. 1989, Weinheim. p. 300-304.
3. Regtien, P.P.L., *Sensors for Applications in Robotics.* Sensors and Actuators, 1986. **10**: p. 195-218.
4. Wang, H., *A Simple Optical Displacement Sensor Utilizing Dual-Channel Angle-Limited Integrated Scattering Measurements.* Journal of Modern Optics, 1996. **43**(11): p. 2279-2288.
5. Bartoletti, C., et al., *The design of a proximity inductive sensor.* Measurement Science and Technology, 1998. **9**(8): p. 1180-1190.
6. Welsby, S.D., *Capacitive and Inductive Noncontact Measurement*, in *Sensors Magazine.* 2003.
7. Libby, H.L., *Introduction to electromagnetic nondestructive test methods.* 1971, New York: Wiley-Interscience. xiv, 365.
8. Aknin, P., D. Placko, and J.B. Ayasse, *Eddy current sensor for the measurement of lateral displacement. Applications in the railway domain.* Sensors and Actuators A, 1992. **31**: p. 17-23.
9. Sharp, R. and L. Pater, *Radiation-tolerant Inductive Proximity Detectors.* Nuclear Energy Jnl British Nuclear Society, 2000. **39**(2): p. 125-129.
10. Kaman Instrumentation, *KD-2300 Instruction Manual Rev. E. (part no. 860021).* 2000, Kaman Corporation, P.O. Box 1, Bloomfield, CT 06002-0001, USA. p. 21-22.
11. Welsby, S.D. and T. Hitz, *True Position Measurement with Eddy Current Technology*, in *Sensors Magazine.* 1997. p. 30-40.
12. Roach, S.D., *Designing and building an eddy current position sensor*, in *Sensors Magazine.* 1998.
13. Tian, G.Y., Z.X. Zhao, and R.W. Baines, *The research of Inhomogeneity in Eddy Current.* Sensors and Actuators A, 1998(69): p. 148-151.
14. Wang, Y. and W.-J. Becker, *Materialunabhangiges Messen des Abstands vonMetallen mit induktiven Naherungssensoren.* Technisches Messen, 1995. **62**(12): p. 470-476.
15. Passeraub, P.A., et al., *Inductive proximity sensor with a flat coil and a new differential relaxation oscillator.* Sensors and Actuators A, 1997. **60**: p. 122-126.
16. Macovschi, M. and C. Poupot, *Study of variable inductance transducers as proximity sensors: I. Computer-assisted study.* Measurement Science and Technology, 1990. **1**(10): p. 1031-1040.
17. Macovschi, M. and C. Poupot, *Study of variable inductance transducers as proximity sensors: II. Experimental study using 'C'-type magnetic circuits.* Measurement Science and Technology, 1990. **1**(12): p. 1291-1296.
18. Passeraub, P.A., et al., *High-resolution miniaturized inductive proximity sensor: characterization and application for step-motor control.* Sensors and Actuators A, 1998. **68**(1-3): p. 257-262.
19. Peyton, A.J., et al., *An overview of electromagnetic inductance tomography: description of three different systems.* Measurement Science and Technology, 1996. **7**(3): p. 261-271.
20. Hardy, L., A. Billat, and G. Villermain-Lecolier, *Flat eddy-current matrix sensor for detecting metallic objects.* Sensors and Actuators A, 1991. **29**: p. 13-19.

21. Fenniri, H., A. Moineau, and G. Delaunay, *Profile imagery using a flat eddy-current proximity sensor.* Sensors and Actuators A, 1994. **45**(3): p. 183.
22. Passeraub, P.A., et al., *Metallic profile and coin imaging using an inductive proximity sensor microsystem.* Sensors and Actuators A, 1998. **66**(1-3): p. 225-230.
23. Belloir, F., R. Huez, and A. Billat, *A smart flat-coil eddy-current sensor for metal-tag recognition.* Measurement Science and Technology, 2000. **11**(4): p. 367-374.
24. Huez, R., F. Belloir, and A. Billat, *Original improvements of a smart eddy current sensor by BSS techniques.* Measurement Science and Technology, 2002. **13**(4): p. 547-555.
25. Marcic, M., *A new inductive displacement transducer.* Sensors and Actuators A, 1998. **70**(3): p. 233-237.
26. Scarr, J.M. and J.K. Zelisse. *A new topography for thickness monitoring eddy current sensors.* in *Society of Vacuum Coasters, 36th Annual Technical Conference.* 1993. Dallas.
27. Johnstone, S. and A.J. Peyton, *The application of parametric 3D finite element modelling techniques to evaluate the performance of a magnetic sensor system.* Sensors and Actuators A, 2001. **93**: p. 109-116.
28. Huang, L.D., et al., *Electromagnetic finite element analysis for designing high frequency inductive position sensors.* Ieee Transactions on Magnetics, 2001. **37**(5): p. 3702-3705.
29. Lenz, J.E., *A Review of Magnetic Sensors.* Proceedings of the IEEE, 1990. **78**(6): p. 973-989.
30. Caruso, M.J., et al., *A New Perspective on Magnetic Field Sensing*, in *Sensors Magazine*. 1998.
31. Gallop, J.C., *SQUIDs, the Josephson effects and superconducting electronics.* 1991, Bristol: Hilger. 232.
32. Ripka, P., *Review of Fluxgate Sensors.* Sensors and Actuators A, 1992. **33**: p. 129-141.
33. Philips Semiconductors, *Data Sheet: Magnetic Field Sensors.* 1998, Philips Semiconductors, Marketing & Sales Communications, Building HVG, P.O. Box 218, 5600 MD EINDHOVEN, The Netherlands.
34. Dodd, C.V. and W.E. Deeds, *Analytical solutions to eddy-current probe-coil problems.* Journal of Applied Physics, 1968. **39**(6): p. 2829-2838.
35. Chari, M.V.K. and P.P. Silvester, eds. *Finite Elements in Electrical and Magnetic Field Problems.* Wiley Series in Numerical Methods in Engineering, ed. O.C. Zienkiewicz. 1980, Wiley-Interscience. 219.
36. Silvester, P.P. and R.L. Ferrari, *Finite Elements For Electrical Engineers.* 2 ed. 1990: Cambridge University Press. 344.
37. Weiss, J. and Z.J. Csendes, *A One-Step Finite Element Method For Multiconductor Skin Effect Problems.* IEEE Transactions on Power Apparatus and Systems, 1982. **PAS-101**(10): p. 3796-3800.
38. Ansoft, *Maxwell 2D Online Help System.* 2002, Ansoft, Four Station Square, Suite 200, Pittsburgh, PA 15219-1119, USA. p. 285-289.
39. Kaye, G.W.C. and T.H. Laby, *Tables of physical and chemical constants : and some mathematical functions.* 15th / now prepared under the direction of an Editorial Committee ed. 1986, London: Longman 1986.
40. Marsh, J. and S. Johnstone. *Investigation into the Use of Inductive Coil Arrays for Metal Object Identification.* in *Proc. Second IEEE International Conference on Sensors.* Accepted for publication. 2003. Toronto, Canada.